

Acknowledgments
References

AR
AR

1. INTRODUCTION

Graphene, a recent addition to carbon allotropes, is set to surpass all other allotropes in utility for life and material sciences due to its many intrinsic properties.^{1–3} Its abundance in the multi-layered form known as graphite can be traced back to antiquity. However, graphite in the form of individual sheets was not technically considered until more recently. It was known in metal workings as Kish and later identified as graphite with impurities existing between the layers.⁴ The structure of graphite was deciphered with the advent of single-crystal X-ray crystallography, which revealed the honeycomb nature of individual layers as shown in Figure 1. The single layer called “graphene” is considered as the first two-dimensional (2D) crystal.⁵

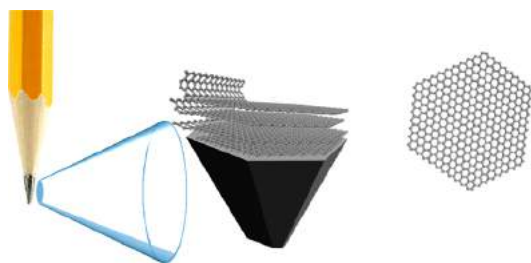


Figure 1. A layer of graphene peeled away from the graphite found in a common pencil.

With an early elucidation by Wallace,⁶ who took to assuming conduction in the layer and not between van der Waals spaced interlayers, it was then envisioned as a 2D material. Later, individual layers were experimentally observed by Boehm et al. from the reduction of graphite oxide, and they showed that the as-formed porous materials have applications such as in the sorption of gases and small organic molecules.^{7,8} Interestingly, Hoffman and Frenzel⁹ described the reduction of graphite oxide using hydrogen sulfide before the demonstration by Boehm et al.^{7,8} that graphite oxide can be exfoliated. These methods of production for single or few layer graphene materials, albeit defective, are still applicable for large-scale production. The ability to make high-quality single layer graphene is credited to Novoselov and Geim who used Scotch tape to pull apart individual layers.¹ This breakthrough made it possible to observe properties that previously were known only in theory. Prior to this mechanical exfoliation, Van Bommel et al.¹⁰ came to the conclusion that a monocrystalline graphite layer is formed over the Si surface, by studying the transformation on the faces of SiC after heating. A model depicting their observations is shown in Figure 2. Upon heating, the silicon is evaporated, allowing the upper carbon atoms to reposition in the next lower layer, and upon longer thermal annealing these atomic carbon layers turn into graphite.¹⁰ A similar phenomenon was noted earlier by Foster et al.¹¹ during the thermal treatment of Al_4C_3 to grow graphite crystals.¹¹ Scanning tunneling microscopy images of single layer graphene were presented in 1992 by Land et al.¹² who decomposed either ethylene or naphthalene on a Pt(111) surface. Forbeaux et al.¹³ in their 1998 article also used the word graphene to describe the top layer of carbon formed during the growth of graphitic layers on SiC.

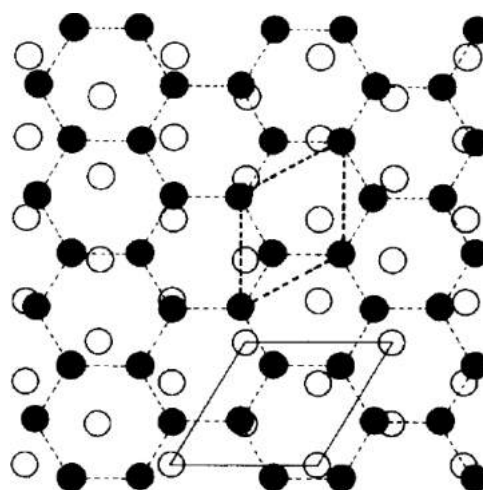


Figure 2. Model of the SiC structure in which three carbon layers of SiC are collapsed under evaporation of Si to form one graphite layer: (---) unit mesh of SiC (0001); (- - -) unit mesh of the graphite layer; (○) C atoms from the collapse of three carbon layers of SiC; and (●) C atoms of the monocrystalline graphite top layer. Reprinted with permission from ref 10. Copyright 1975 Elsevier B.V.

When the atoms of carbon participate in robust covalent bonds between sp^2 hybridized states forming an extended honeycomb topology, it gives the structure formed a strength to weight ratio that remarkably outperforms metals and metal composites.³ Even with such strength, it is relatively flexible and thus can form the different allotropes such as carbon nanotubes, nanohorns, and fullerenes.^{14–19} Furthermore, the zero band gap of graphene gives it excellent electron mobility; the investigation and modification of this mobility is important as a means to replace current semiconductors in electronic devices.^{20,21} Such changes can come about by altering graphenes structural dimensions.^{22–25} Ideally, a few C atoms thick electronic devices could make such devices nearly invisible, as a single sheet of graphene is $\sim 97.7\%$ transparent to white light, and represents a new means of delivering information.²⁶

Prior to the focus on graphene (G), there was extensive research on the preparations and properties of graphite oxide and later graphene oxide (GO).^{27–31} The obvious difference between G and GO is the addition of oxygen atoms bound with the carbon scaffold as shown in Figure 3. As a result, G is hydrophobic in



Figure 3. Oxidation of graphene sheet to form graphene oxide.

nature whereas GO is hydrophilic, that is, easily dispersible in water. In addition, GO contains both aromatic (sp^2) and aliphatic (sp^3) domains, which further expands the types of interactions that can occur with the surface. GO is easily reduced to reduced GO at high yields; however, the quality of the produced graphenes is not suitable for electronic applications or mechanical reinforcement of polymers due to structural defects created during the synthesis of GO. Still this is a preferable route for large-scale handling of graphenic materials with tailored surface properties by functionalization.

Both G and GO described above play a central role in materials science thanks to their unique structural and morphological features, relatively easy chemical modification toward task-specific materials, as well as excellent electrical, mechanical, and thermal properties. Some niche applications include low-cost, large-area, flexible and/or lightweight electronics, displays or e-papers, polymer composites, catalysts, energy-related materials, sensors, and bioderivatives. Particularly the moderate reactivity of G at the interface provides a powerful tool in controlling its structure and properties to meet the applications listed above. Last, G/GO provides an excellent platform for the size-controlled deposition of highly dispersed nanoparticles with catalytic activity.

In most cases, functionalization is the best way to achieve the best performance out of G or GO. In this respect, the literature is massive for the growing applications of G and GO modified through both noncovalent interactions and covalent bonds. Generally, covalent functionalization compromises the sp^2 structure of G lattices, thus resulting in defects and loss of the electronic properties. In contrast, noncovalent functionalization is largely preferred as it does not alter the structure and electronic properties of G while it simultaneously introduces new chemical groups on the surface. Common examples of noncovalent functionalization include polymer wrapping, π - π interactions, electron donor-acceptor complexes, hydrogen bonding, and van der Waals forces (see examples in Figure 4). In all instances, noncovalent functionalization leads to enhanced dispersibility, biocompatibility, reactivity, binding capacity, or sensing properties.

This Review focuses on noncovalent interactions of G and GO. First, a brief description regarding the nature of noncovalent interactions with G/GO is given in section 2. A detailed survey of various types of interactions and functionalization modes is provided in subsequent sections covering also the interactions of

G/GO with polymers, aromatic molecules, biomolecules, drugs, and solvents (section 3). Later, the combination of G/GO with other carbon nanoallotropes and different 2D graphene analogues through noncovalent interactions and 3D superstructures follows (section 4). A significant part of this Review is devoted to the attachment of metal nanoparticles, metal oxide nanoparticles, and semiconducting nanoparticles (quantum dots) onto the surface of G/GO through simple, noninvasive deposition techniques with emphasis on applications in catalysis and lithium-ion batteries. Additionally, specific exploitations of various noncovalently modified G/GO in environmental, biomedical, sensoric, and catalytic applications, as well as in energy materials and nanodevices, are discussed (section 5). This Review ends with a look at current and future prospects of noncovalently modified G/GO (section 6).

2. NONCOVALENT INTERACTIONS OF GRAPHENE AND GRAPHENE OXIDE

Noncovalent or supramolecular interactions are found in all types of materials that experience attractive and/or repulsive forces between them. These interactions are found in many natural and synthetic systems for recognition or detection.^{32,33} For the sake of simplicity, this Review will consider pristine G and avoid defects to the carbon honeycomb scaffold. The allowance of defects or distortions caused by the transformation of sp^2 carbon to sp^3 carbon, in the case of GO, for its involvement with noncovalent interactions is potentially beneficial for combining multiple interactions and will be discussed later.

To compare the relative strength of noncovalent interactions, we consider (i) the energy range of covalent bonds and (ii) the bond distances of single to multiple carbon bonds. The dissociation energies are ~ 350 kJ mol⁻¹ for single, ~ 611 kJ mol⁻¹ for double, and ~ 835 kJ mol⁻¹ for triple bonds, while the bonding distances range from 1.54, 1.34, and 1.20 Å for ethane, ethene, and ethyne, respectively.^{34,35} The energies of individual noncovalent/supramolecular interactions are normally lower than those mentioned for covalent bonds, but when combined over large surfaces they can rival some covalent bonds. The energy ranges for different interactions have been summarized by Atkins and de Pula,³⁶ Steed and Atwood,³⁷ and Skinner and Connor.³⁸ Dissociation energies for ionic bonds range from 100 to 350 kJ mol⁻¹ and are similar to those of organometallic metal-carbon bonds, which range from 150 to 400 kJ mol⁻¹. The dissociation energy begins to decrease for noncovalent interactions; that is, ion-dipole or coordinate covalent bonds range from 50 to 200 kJ mol⁻¹ for coordination complexes or metals bound in crown ethers. These dissociation energies allow noncovalent/supramolecular systems to be reversible, or kinetically labile, and thus self-correcting. With graphenic materials, the π - π or CH- π interactions are prominent with dissociation energies less than 50 kJ mol⁻¹. The weakest forces, that is, London-dispersion forces or van der Waals interactions, affect all atoms in close proximity. The solvation and hydrophobic effects (caused by different interactions types) are a large component to consider in G and GO systems as they influence not only its dispersibility but recognition interactions that can be used for sensing.^{39,40} The focus on π - π and hydrogen bonds is to target an accessible region at room-temperature conditions, thus making it easier to investigate without specialized laboratory equipment.

Interested readers can find additional detailed information about aromatic interactions in relation to the π - π interactions (i.e., π - π stacking interaction) from the review article by

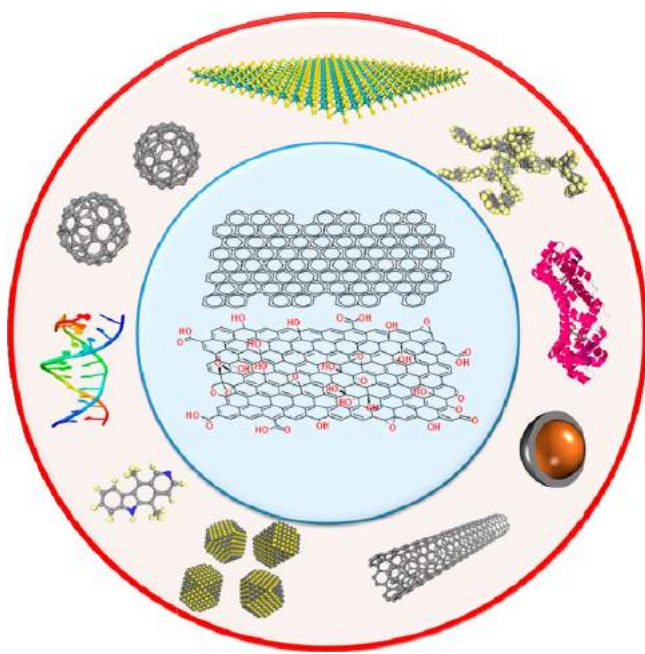


Figure 4. Schematic representation of noncovalent interactions of G/GO with selected application-important species involving MoS₂, aromatic polymers, proteins, core-shell nanoparticle, nanotube, quantum dot, ellipticine (drug/photoluminescence probe), DNA segment, and fullerenes (clockwise from top).

Hunters et al.⁴¹ In G, two types of π - π interactions occur between the electron-rich and electron-poor regions, which influence its interaction with other molecules or nanomaterials. This is commonly seen in the face-to-face and edge-to-face arrangement as shown in Figure 5 for C_6R_6 , where R is hydrogen

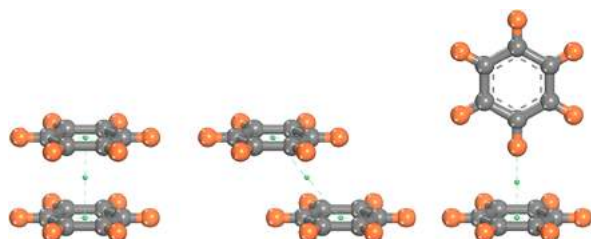


Figure 5. π - π stacking face-to-face (left), slipped (middle), and C-H $\cdots\pi$ (right) type from benzyl molecules where the gray atoms represent carbon and orange represents hydrogen for benzene or other atoms for different derivatives.

for benzene and other substituents that alter the ring's polarity. These interactions are not limited to benzene but are also observed in biologically relevant molecules such as DNA and porphyrins. Similarly, these interactions found in small molecules are carried over to GO and G systems where they can be employed to functionalize them for processing and property modification.

The general representation of π - π interaction types observed in G can be seen in Figure 6. Along with this, there is also a small

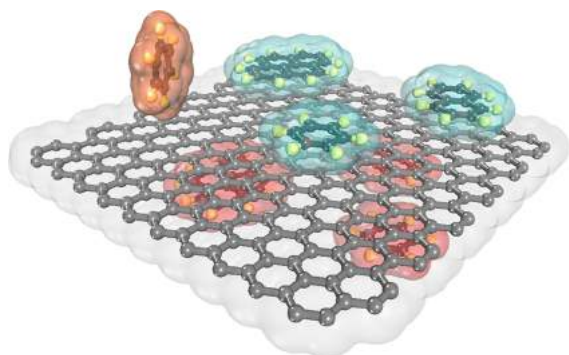


Figure 6. Idealized π - π or C-H $\cdots\pi$ interactions from benzene, naphthalene, or pyrene molecules above and below the basal plane of graphene.

possibility that CH $\cdots\pi$ -like interactions occur around the edge of G that may be terminated with a hydrogen atom or from phenyl rings oriented perpendicular to the surface of G. Because G is several magnitudes larger than the participating section of the modifying molecule or polymer, there should be multiple interactions on both sides of the G sheet.

For GO, or more so for reduced graphene oxide (rGO), the basal plane is relatively similar to G except for defects by epoxides or hydroxides bound to the carbon atoms. For this reason, similar π -interactions will likely occur as shown with G, but there are additions of both hydrogen-bond donors and acceptor moieties from the epoxides, alcohols, ethers, carboxylic, and carboxylate oxygen bearing moieties that can contribute an additional mode for interactions. As shown in Figure 7, the oxygen moieties on GO may predominantly situate near or on the edges and aide in binding. Although it is still unclear the qualitative and quantitative distribution of various oxygen bearing functional

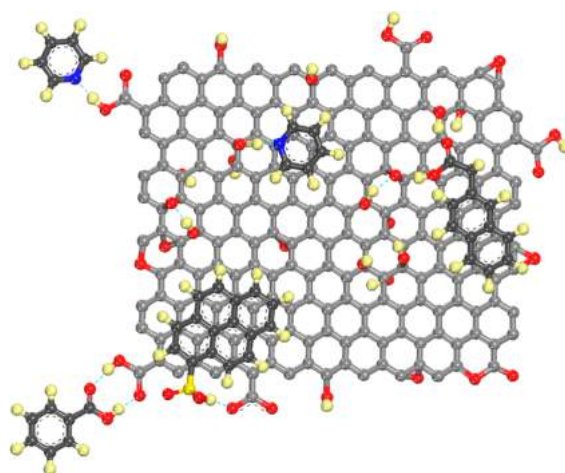


Figure 7. Schematic representation of both hydrogen bonds and/or π - π stacking with GO.

groups within the basal plane, the reduction of GO can remove many of these groups, leaving an edge dominant oxygen moiety starting material.

Supramolecular interactions with G and the undisturbed regions of GO impart minimum structural impairment, and as such many of the original properties of the starting materials are retained.

The real time visualization of G, or graphite, with molecules adsorbed on the surface via noncovalent interactions, is evident from several scanning tunneling microscopy (STM) studies. Theoretical studies show that molecules on the G surface at either the solid-liquid, solid-atmosphere, or solid-vacuum interface are possible and can manifest as a property modifier for G.⁴²⁻⁴⁴ Foster and Frommer's first observation of single to several monolayers of 4-*n*-octyl-4'-cyanobiphenyl onto the surface of highly oriented pyrolytic graphite (HOPG) showed that the ordering lasted for several days during constant scanning (see Figure 8).⁴⁵

Aromatic bodies with aliphatic chains are utilized well for designing 2D crystals on different flat surfaces including G. The favorable π - π interaction allows the molecules to lie flat on the surface while either hydrogen bonding or hydrophobic interaction guides the molecules to form the 2D supramolecular

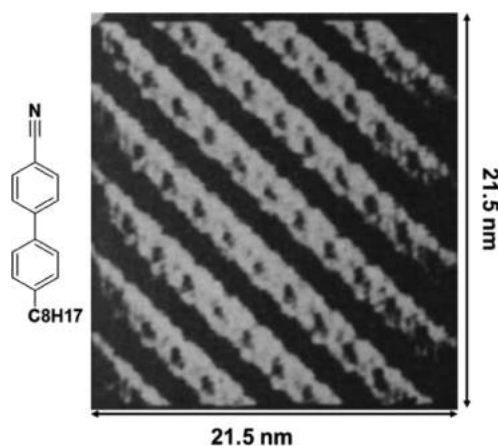


Figure 8. Molecules of 4-*n*-octyl-4'-cyanobiphenyl aligned on the surface of HOPG. Reprinted with permission from ref 45. Copyright 1988 Nature Publishing Group.

systems. The classic example of hydrogen bonding, leading to 2D supramolecular systems on graphite, is the organization of trimesic acid, which shows the different honeycomb (see Figure 9a) or flower (see Figure 9b) motifs. Griessel et al.⁴⁶ showed that

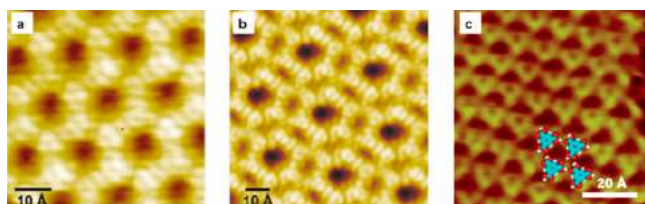


Figure 9. Scanning tunneling microscopy (STM) images of trimesic acid on the surface of HOPG in (a) honeycomb, (b) flower, and (c) close packing motifs. Panels (a) and (b) reprinted with permission from ref 46. Copyright 2002 Wiley-VCH. Panel (c) reprinted with permission from ref 49. Copyright 2014 Royal Society of Chemistry.

the formation of these motifs is due to the formation of carboxylic acid dimer or trimer hydrogen bonds, respectively. This same group also demonstrated the adsorption of coronene, considered the smallest piece of G, on the cleaved surface of HOPG.⁴⁷ These two motifs, formed during trimesic acid organization, have been modeled on G and found to influence its electronic properties; this influence is based on the polymorphism.⁴⁸ The honeycomb motifs have also been observed in multilayer G by Zhou et al.,⁴⁹ who also identified a close packing motif (see Figure 9c) on bilayer G supported on SiC. Shortly afterward, the honeycomb arrangement on single layer G was observed by MacLeod et al.,⁵⁰ and they pointed out that the different supports under the G affect the 2D network. These authors also reported a lack of bandgap opening, using ultraviolet photoelectron spectroscopy, resulting from monolayer adsorption of a trimesic acid network, suggesting a lack of charge transfer.⁵⁰

Adding tetrafluoro-tetracyanoquinodimethane (F4-TCNQ) to 1–3 layered epitaxial graphene (EG) grown on the 6H-SiC(0001) crystal face was observed using low energy electron diffraction (LEED) along with angle-resolved photoemission spectroscopy (PES). Chen and colleagues demonstrated a p-type doping effect due to electron transfer from EG to the F4-TCNQ adsorbed layer.⁵¹ Interestingly, this layer was not observed on the EG/SiC substrate from STM, but from the STM height data it was considered to stand upright on the surface as shown in Figure 10a.⁵² On the other hand, Stradi et al.⁵³ showed that monolayer coverage of F4-TCNQ or TCNQEG on a Ru(0001) face (see Figure 10b) tailored the magnetic ordering of EG.

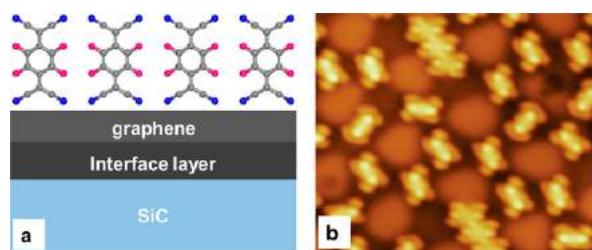


Figure 10. (a) Upright arrangement of F4-TCNQ on EG/SiC and (b) parallel with the EG/Ru surface. Panel (a) reprinted with permission from ref 52. Copyright 2010 American Physical Society. Panel (b) reprinted with permission from ref 53. Copyright 2014 Royal Society of Chemistry.

Monolayer adsorption of 3,4,9,10-perylene tetracarboxylic dianhydride (PTCDA) arranging in an herringbone motif on bilayer EG/SiC(0001) has been observed (see Figure 11).^{54–57}

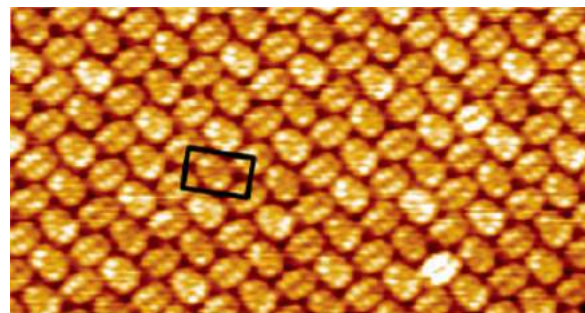


Figure 11. Monolayer of PTCDA adsorbed on EG/SiC(0001). Reprinted with permission from ref 54. Copyright 2009 American Chemical Society.

With scanning tunneling spectroscopy (STS), Lauffer et al.⁵⁵ observed n-type doping due to charge transfer from PTCDA to EG. In the same way, Huang et al.⁵⁴ observed a weak charge transfer from PTCDA to the EG layer using high-resolution PES.

Similar to PTCDA, perylenetetracarboxylicdiimide (PTCDI) forms monolayers on EG/Rh(111) and EG/SiC(0001).^{58,59} PTCDI monolayers, which adopt a herringbone arrangement, were thermally more stable by around 40 °C than PTCDA on the EG/SiC surface.⁵⁹ It was calculated by Kozlov et al.⁶⁰ that the bandgap will increase from the physisorption of PTCDI on G. Differences in the 2D arrangement of alkylated and nonalkylated PTCDI on EG/Rh(111) were observed by Pollard and coauthors. The hydrogen-bonding ability between the C=O and N–H in nonalkylated PTCDI allows for linear-like arrangement (see Figure 12a), while the alkylated PTCDI

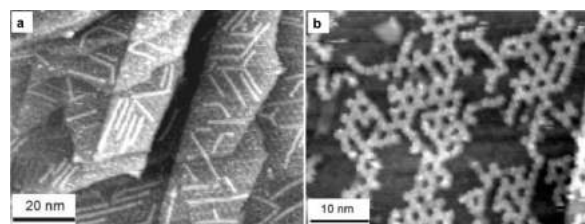


Figure 12. (a) Supramolecular chains of PTCDI and (b) an alkyl PTCDI derivative adsorbed on EG/SiC. Reprinted with permission from ref 58. Copyright 2010 Wiley-VCH.

molecules were observed to form hexagonal motifs (see Figure 12b).⁵⁸ This type of hydrogen bonding is believed to be one of the reasons behind the stability of the adlayers on EG.

The issue of the interface layer having a profound influence on the G layer was not considered here, but is another challenge for future devices, which needs to be considered. We have briefly shown that many of the aromatic bodied molecules lie parallel with the G basal plane and that there are still challenges to explore in this research area. One of the challenges is to have free floating G, G bridge, or one or both surfaces covered with electron-donating or -withdrawing molecules. Also challenging will be to prepare Janus like G,⁶¹ with two different π – π stacked molecules on either side of G for physical property tailoring. These small molecules that self-assemble onto G and other 2D materials are emerging tools for tailoring the band structure of G.

Before noncovalent interactions can be applied to G, the ability to prepare G dispersed in solution must be considered. A lot of work to make G a viable option for applications has been focused on improving its dispersibility in solvent without altering the honeycomb structure and leaving the material intact. It was revealed by Coleman and others that the surface tension of the solvent should be similar to the surface energy of the material to be exfoliated, that is, a crucial factor for preparing useable quantities of 2D materials.^{30,62–69} It has been found that the surface energy of G of approximately 68 mJ m^{-2} is similar to results from contact angle measurements by Wang et al.⁷⁰ who reported surface free energies of 54.8 and 46.7 mJ m^{-2} for graphite and G, respectively. This value is not necessarily best at explaining the exfoliation for G from graphite, but the Hansen and Hildebrand solubility parameters can shed insight for the dispersion of nanomaterials.^{71–73} The Hansen parameters describe the solvent's mixing ability of dispersive (δ_D), polar (δ_P), and hydrogen-bonding (δ_H) interactions. With G, it was approximated at $\delta_{D,G} \approx 18 \text{ MPa}^{1/2}$, $\delta_{P,G} \approx 10 \text{ MPa}^{1/2}$, and $\delta_{H,G} \approx 7 \text{ MPa}^{1/2}$.⁶⁷ These parameters are found for common organic solvents with a low vapor pressure such as NMP and DMF, and also for solvents like isopropanol.⁶⁶ This enhancement in our understanding to prepare good dispersions of G or other 2D nanomaterials has a small drawback with the commonly applied sonication procedure. That is, with longer times in the sonication bath, the size is generally reduced, but the quality remains intact.

Alternatively, π – π interactions can be experimentally studied by single molecule force spectroscopy (see Figure 13a).^{74,75} Single molecule force spectroscopy is considered as a powerful experimental tool providing a direct measurement of intermolecular force precisely at a single molecular level; it has been successfully employed to monitor many intramolecular and intermolecular interactions such as covalent bonding, ligand–receptor pairing, host–guest complexation, hydrogen bonding, coordination bonding, hydrophobic interactions, and charge-transfer interactions. For instance, the π – π interactions were directly observed between pyrene and graphite surface in aqueous solutions, manifested by single molecular ruptures (see Figure 13b).⁷⁴ The force curve fitting provided determination of the strength of the π – π interactions amounting to $\sim 55 \text{ pN}$. Another experimental example involves measurement of the force needed to peel the single-stranded DNA from the surface of single crystal graphite; with single molecule force microscopy, it was feasible to identify two types of force–displacement curves, that is, steady-state peeling or polymer chain stretching, depending on the type of the substrate.⁷⁵ Effective binding energy for interaction between polythymine and graphite was then estimated to be $11.5 k_B T$ per nucleotide, in accordance with the theoretically predicted results.

3. DRIVING FORCES FOR NONCOVALENT FUNCTIONALIZATION OF GRAPHENE AND GRAPHENE OXIDE

The noncovalent functionalization of G and GO is mostly based on van der Waals forces or π – π interactions with organic molecules or polymers that meet some basic criteria. Usually, van der Waals forces are developed between G or GO and organic molecules or polymers with high hydrophobic character, while π – π interactions are common between G or GO and molecules with short to highly extended π system. Because of the regular presence of oxygen groups on the surface and edges of GO, ionic interactions and hydrogen bonds are often involved. This is in

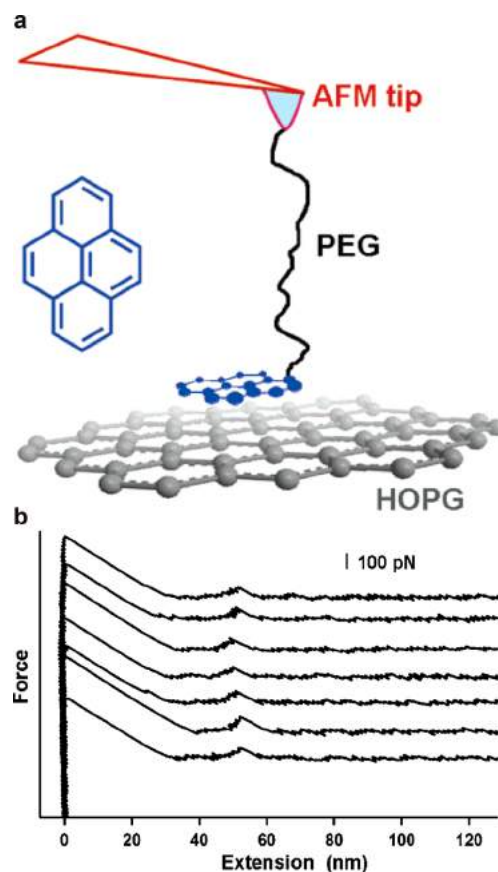


Figure 13. (a) Schematic setup used for measuring the π – π interactions between pyrene and graphite in aqueous medium by single molecule force microscopy. (b) Force curves of pyrene-modified tips desorbed from graphite substrate in aqueous medium under a retraction velocity of 500 nm/s and at room temperature. Reprinted with permission from ref 74. Copyright 2007 American Chemical Society.

contrast to pristine G, which has no oxygens that could contribute to these kinds of interactions.

The noncovalent interactions are very important for most applications because the extended π system of graphenic nanostructures is not interrupted, which means that important properties such as electric conductivity or mechanical strength are not affected. In addition, the mild and nonpermanent character of noncovalent interactions offers high flexibility with regards to the treatment of the afforded products. Taking into account that a comprehensive presentation of the noncovalent interactions of graphenic nanostructures has been presented in 2012, that is, our review on G functionalization,⁷⁶ this section is focused on the most recent representative research that deals with the noncovalent interactions of graphenic nanostructures with aromatic species, organic molecules, other carbon nanostructures, and inorganic species.

3.1. π – π Interactions

Depending on the basic properties of the aromatic molecules that are concerned, π – π interactions can be involved with the exfoliation of graphite and the stabilization of graphenic nanostructures in dispersion, the use of G as a platform for drug delivery, and the formation of a great variety of hybrids or composite functional materials with advanced properties. On the other hand, basic properties of the organic-aromatic components such as photoluminescence, light absorption, chemical stability, hydrophilicity or hydrophobicity, and morphological and

structural characteristics are often influenced by their interactions with G/GO nanostructures.

The π - π interactions have two prevalent requirements. The first is the existence of π systems, and the second has to do with the geometry of the interacting species. It is necessary that an overlap exists between the two components to have a noticeable interaction, and usually this is strongly favored by the planarity of the two components. A pristine G monolayer has a rich extended aromatic system with almost planar geometry, which prefers to interact strongly with small aromatic molecules. On the other hand, rGO has decreased aromatic character, while GO can be described as a nonaromatic surface with sp^3 carbon atoms with isolated small aromatic areas, sp^2 domains. Furthermore, the existence of the sp^3 carbon atoms (bonded with oxygen groups) introduces extended deviations from the planarity for GO. These two important factors are intended to differentiate the behavior of GO and rGO from that of G as regards the interaction with aromatic species. On the other hand, the behavior of a G nanostructure is not always similar to all aromatic molecules. The π - π interactions are influenced by several factors related to the aromatic molecules, among them the electron-donating or -withdrawing ability,^{77,78} their substituents, size, and planarity.⁷⁹

Su et al.⁷⁸ used pyrene and perylenediimide derivatives to study the π - π interactions between electron donor and acceptor aromatic molecules with graphenic nanosheets. Both aromatic derivatives have been shown to interact strongly with rGO (symbolized as ReG in Figure 14), and the resulting hybrids were highly dispersible in water due to the sulfonic groups that, as part of the aromatic molecules, induce repulsive forces between the hybrid nanostructures. The π - π interactions of an electron donor such as pyrene-1-sulfonic acid (PyS) or an electron acceptor such as 3,4,9,10-perylenetetracarboxylic diimidebisbenzenesulfonic acid (PDI) and rGO are characterized by a remarkable charge-transfer effect that is confirmed by the Raman spectra of the hybrids as a shift of the G-band to lower or to higher frequencies, respectively (see Figure 14).

A similar change (upshift and downshift, respectively) was also observed for the C 1s XPS peaks of the hybrids that correspond to sp^2 carbon in the basal plane of graphenic sheets. The characterization of the hybrids by atomic force microscopy (AFM) revealed planar nanostructures with 1.7 nm thickness that corresponds to a two-phase functionalized graphenic monolayer or 3.4 nm thickness that corresponds to a tandem sandwich structure (see Figure 15).⁷⁸

Using 1-naphthylamine, 1-naphthol, and naphthalene as model aromatic molecules with different polarity, Li et al.⁸⁰ showed that polarity is connected to the adsorption ability on a magnetically modified GO. Zhang et al.⁸¹ have presented a detailed study on the ability of different carbon nanostructures to interact with π - π interactions (see Figure 16). They examined the binding ability of GO, rGO (it is characterized as chemically derived graphene, CDG), and single wall carbon nanotubes (SWNTs) using sulfonated aluminum phthalocyanine (AlPcS₄) as the second aromatic planar component.

The π - π interactions of rGO with AlPcS₄ lead to the formation of a ground-state complex between the two components, which is characterized by a remarkable red shift and decrease of the Q absorption band of phthalocyanine as presented in Figure 16. It is also recorded that when the concentration of rGO reaches 12 mg mL⁻¹, the free AlPcS₄ almost disappears, while a similar concentration of GO (16.2 mg mL⁻¹) decreased free AlPcS₄ by only 30%. The analogous interaction with respect to SWNTs appeared far weaker. The

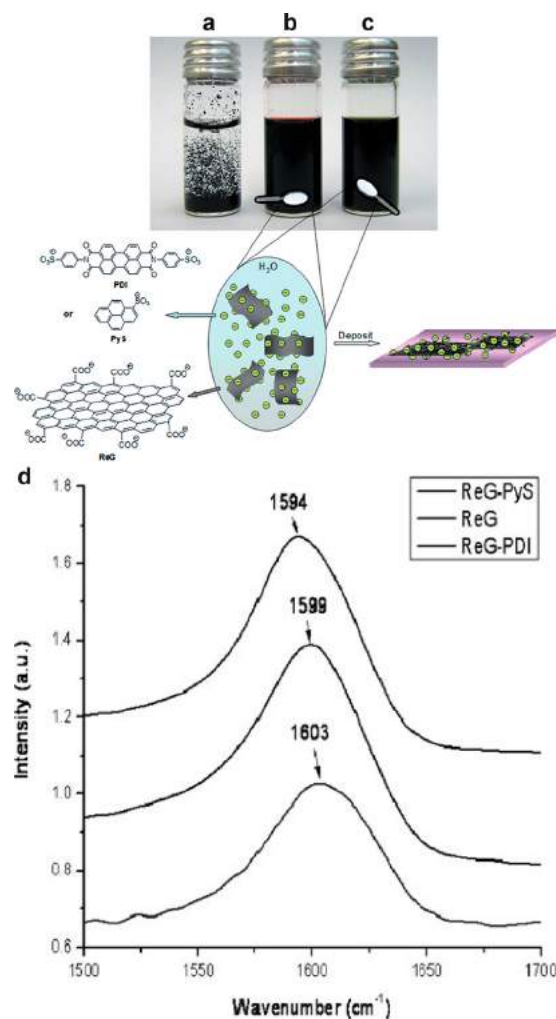


Figure 14. Aqueous dispersion of (a) rGO, (b) rGO-PDI, and (c) rGO-PyS after centrifugation. (d) G-bands of the Raman spectra of the rGO, rGO-PDI, and rGO-PyS hybrids. Reprinted with permission from ref 78. Copyright 2009 Wiley VCH.

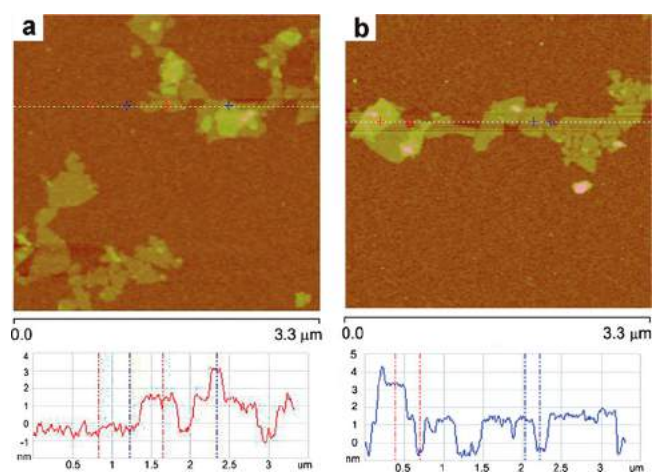


Figure 15. AFM images and cross-section analysis of (a) rGO/PyS and (b) rGO/PDI on mica. Reprinted with permission from ref 78. Copyright 2009 Wiley VCH.

binding capability as expressed by the formation constant K_f of the complex was estimated to be 21.6 for rGO, 0.31 for GO, and 0.012 g⁻¹ L for SWNT. It was concluded that the binding ability

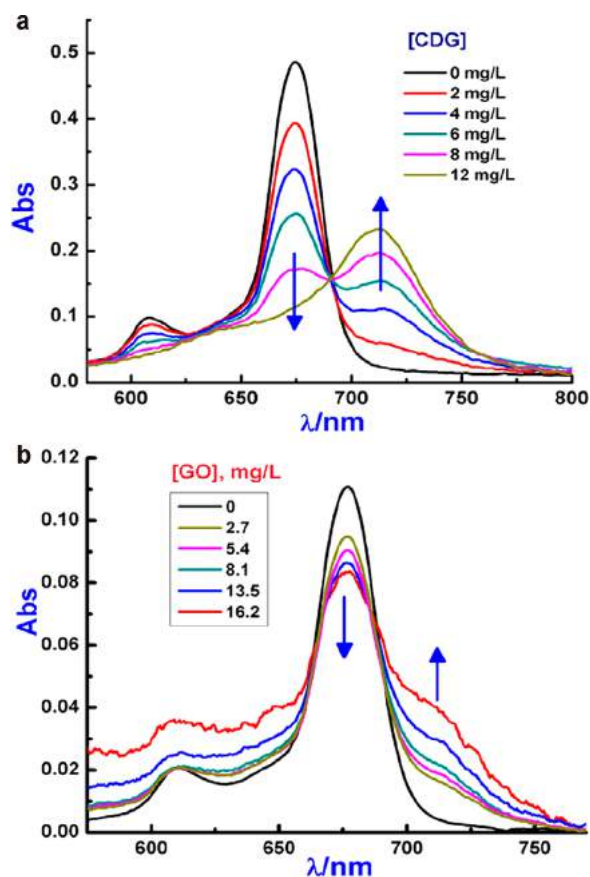


Figure 16. UV-vis absorption change of AlPcS₄ (15 μM for rGO and 3 μM for GO) by the interaction with increased amount of (a) rGO and (b) GO. Reprinted with permission from ref 81. Copyright 2014 Elsevier B.V.

of carbon nanostructures is analogous to the planarity of the structure, and to bind with the planar AlPcS₄, rGO is by far more favored while the most curved SWNTs are not. The interaction of carbon nanostructures with the excited state was examined by the photoluminescence spectrum of AlPcS₄ in the presence of carbon nanostructures. As presented in Figure 17, the characteristic emission band at 685 nm of AlPcS₄ (15 μM) was decreased by the addition of rGO and totally disappeared when the concentration of rGO reached 12 mg L⁻¹. The plot of intensity quenching as presented in Figure 17 showed that rGO (it is referred to as graphene in Figure 17) is much more efficient than GO, which means that rGO is also favored as regards the interaction of the excited state of AlPcS₄ with carbon nanostructures, due to the enhanced electron-deficient character in comparison with SWNTs or GO.

The adsorption capability of GO and rGO has been also studied by Chen et al.⁸⁰ using three simple aromatic hydrocarbons, naphthalene, phenanthrene, and pyrene, to compare their affinity to GO and rGO. The authors showed that hydrophobic character and the molecular size of the graphenic material affect the adsorption capability, as GO has far less adsorption capability than rGO.

Although pristine G was not a subject of the work by Zhang et al.⁸¹ or Chen et al.⁸² presented in the previous section, it can be easily concluded that G would be much more favored with π - π interactions than rGO or GO. G has a much more extended aromatic system and planarity, which means that the free surface that is offered to the aromatic molecules is much larger and so the

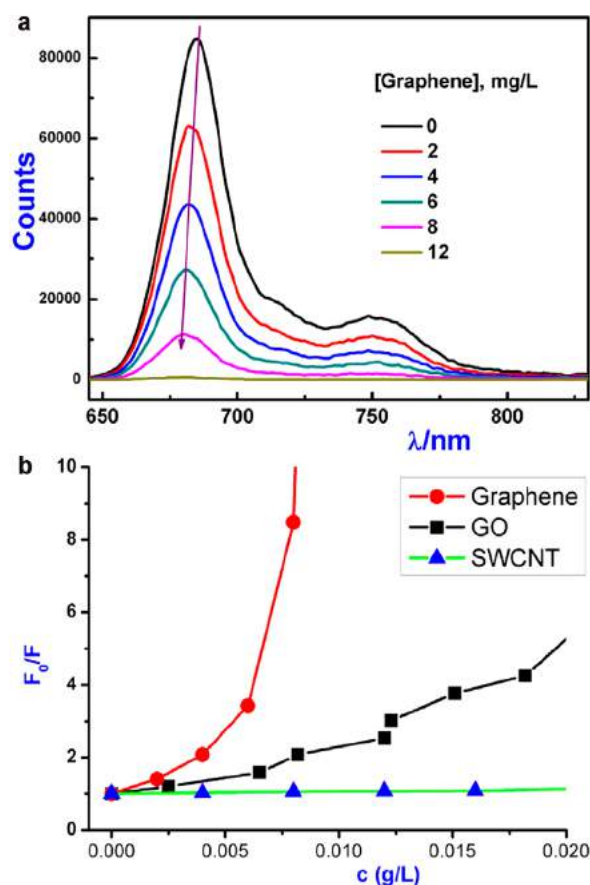


Figure 17. (a) PL of AlPcS₄ (15 μM) in the presence of rGO with excitation at 610 nm. (b) The plot of the intensity of quenching with the concentration of rGO, GO, and SWNTs. Reprinted with permission from ref 81. Copyright 2014 Elsevier B.V.

interactions are stronger. Because of these advantages, π - π interactions of G with small aromatic molecules such as pyridine and fluorinated benzene derivatives,^{83,84} quinoline,⁸⁵ pyrene,^{86–93} anthracene,^{94,95} triphenylene,⁹⁶ coronene,⁹⁷ ionic liquids,^{98–102} and polymer ionic liquids¹⁰³ or porphyrin derivatives¹⁰⁴ can cause the exfoliation of graphite and/or stabilization of the afforded G nanosheets in organic solvents or water. In other words, π - π interactions can be the driving force for the exfoliation of graphite and stabilization of G derivatives in dispersion. The aromatic molecules act as wedges and penetrate slowly between the graphenic layers usually by the assistant of sonication. By this method, the graphenic layers are gradually dissociated from each other, leading finally to a complete separation. The aromatic core of these molecules is usually decorated by hydrophilic or lipophilic chains or groups providing, and through this the liberated graphenic layers are stabilized in water or organic solvents, respectively. Pynidinium tribromide is, among others, a characteristic aromatic molecule that exfoliates graphite and stabilizes graphenic monolayers or multilayers in water thanks to the electrostatic repulsions between the charged pyridinium species that are attached.⁸³ Lee et al.⁸⁶ used a tetrapyrrene derivative (**1** in Figure 18) decorated by a oligoetherdendron to exfoliate graphite and stabilize graphenic layers. The tetrapyrrene aromatic skeleton interacted with G, while oligoether chains induce a high hydrophilic character to the hybrid. The authors showed also that the same tetrapyrrene derivative is unable to disperse SWNTs, indicating that the planarity of the carbon nanostructure

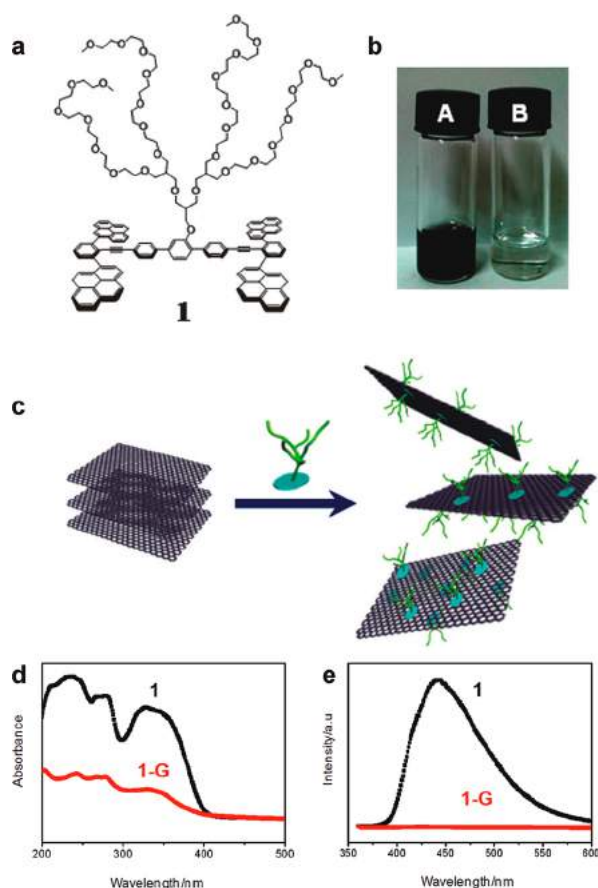


Figure 18. (a) Structure of the tetrapyrrene derivative. (b) The resulting hybrid is highly dispersible in water (1.5 mg mL^{-1}). (c) Schematic representation of exfoliation process. (d) Absorption and (e) emission spectra of **1** and **1-G** in 0.2 wt % (MeOH/H₂O); $\lambda_{\text{ex}} = 340 \text{ nm}$. Reprinted with permission from ref 86. Copyright 2011 Royal Society of Chemistry.

is a crucial factor for the formation of an effective π stacking. The π - π interactions are confirmed by the red-shifted absorption band and the quenching of the fluorescence band of pyrene when it interacts with G (product **1-G** in Figure 18).⁸⁶

Palermo et al.⁹² used a series of sulfonated pyrene derivatives to study graphite exfoliation and G stabilization. The pyrene core is functionalized with one, two, three, or four sulfonic groups, which are electron acceptors, while two of them are also functionalized with two and one hydroxyl groups, which are electron donors as presented in Figure 19. The authors studied the procedure in two steps. The first step was the absorption of the pyrene molecules on graphite surfaces without sonication to avoid changes in the initial free surface. Calculating the amount of the unabsorbed pyrene derivative, it was estimated that their



Figure 19. Four pyrene derivatives with increasing number of sulfonic groups used for the study of graphite exfoliation and G stabilization. Reprinted with permission from ref 92. Copyright 2013 Royal Society of Chemistry.

absorption on the graphite surface is inversely proportional to the number of the polar sulfonic groups. The second stage was the exfoliation and dispersion in water of the G/pyrene derivative hybrids. In this stage, the favorite molecule for exfoliation is that which has the highest dipole moment and the most asymmetric functionalization (PS2 in Figure 19).⁹²

Imidazolium salts have also been used to interact with rGO monolayers.^{98–102} These molecules interact with rGO monolayers by cation- π and π - π interactions, while electrostatic repulsions prevent aggregation between the rGO monolayers. In these studies, the role of these interactions is limited to the stabilization of G derivatives in polar solvents or water, because the oxygen groups of GO strongly favor exfoliation. By derivatization with phenyl vinyl groups, imidazolium ionic liquids that are π stacked on G are then copolymerized with vinyl monomers such as methyl methacrylate leading to a G-based polymer composite with homogeneous dispersion of G sheets and strong interaction between the components.¹⁰⁰

Geng et al.¹⁰⁴ showed that a negatively charged porphyrin derivative (TPP-SO₃Na in Figure 20) is a better dispersant than a

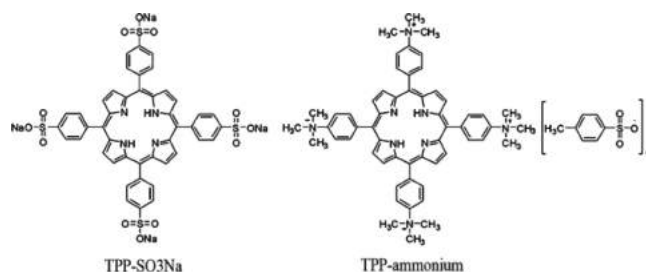


Figure 20. Porphyrin derivatives with sulfonate and ammonium groups. Reprinted with permission from ref 104. Copyright 2010 American Chemical Society.

positively charged one (TPP-ammonium in Figure 20). Although both derivatives strongly interacted with rGO, only the negatively charged porphyrin can keep the G sheets in dispersion due to the repulsive forces that developed between the negative charges after the noncovalent functionalization.

The role of the interaction between the π systems of the G structure and aromatic molecules in the final hybrid is so decisive that in some cases it can induce important changes in the structure of the molecules. For example, the introduction of methylpyridinium groups as substituents to the planar porphyrin causes deviation from planarity because pyridinium groups are aligned almost perpendicular to the porphyrin plane due to steric hindrance (see Figure 21). Xu et al.¹⁰⁵ showed that electrostatic and mainly π - π interactions of this tetrapyrrolium porphyrin derivative with G forced pyridinium groups to be aligned in the plane with the porphyrin, resulting in a further increase of the π - π interaction.

As regards the electronic properties of graphenic structures, Arramel et al.¹⁰⁶ showed that interaction with metallic porphyrins can cause a band gap opening in G, which could be further tuned depending on the metal cation of the porphyrin. For example, π stacking of iron protoporphyrin on G yields a band gap of 0.45 eV, while the zinc analogue gives a smaller band gap of about 0.23 eV.

The π system of organic molecules that interact with graphenic nanostructures is also responsible for the photophysical properties of these compounds, and usually the noncovalent

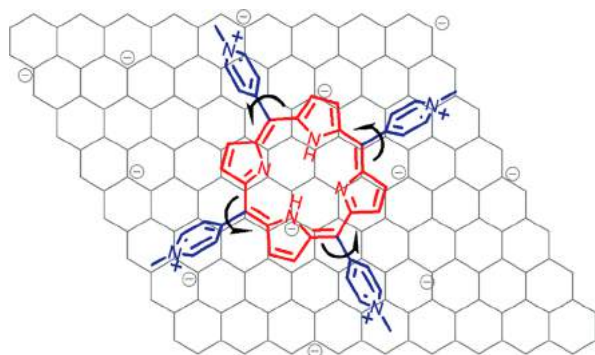


Figure 21. Schematic representation of pyridinium-functionalized porphyrin interacting with G by π stacking. Reprinted with permission from ref 105. Copyright 2009 American Chemical Society.

interaction with G nanostructures causes important changes.^{107,108}

Phthalocyanine is a highly active chromophore, and its tetrasulfonated derivative (TSCuPc) is totally soluble in water. As a consequence of its aromaticity, it is easily attached onto G nanosheets by π stacking forming highly hydrophilic hybrids (see Figure 22).¹⁰⁸

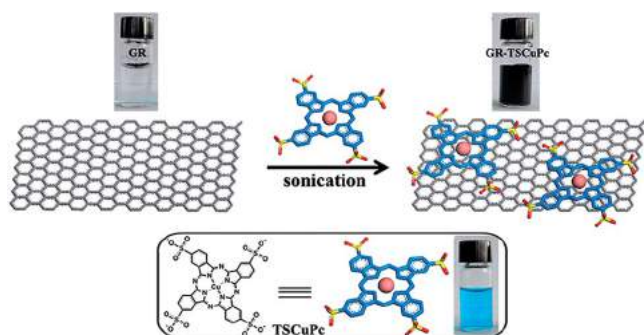


Figure 22. π - π interaction of phthalocyanine TSCuPc with G (GR in the image). Reprinted with permission from ref 108. Copyright 2014 Royal Society of Chemistry.

The effective π - π interaction is revealed by the UV-vis spectrum of the hybrid where the characteristic band of the phthalocyanine dimer is not presented because interactions with G prevent the dimerization of phthalocyanine; additionally the Q-band of the monomer, which normally occurs at 663 nm, has been shifted to 705 nm (see Figure 23).¹⁰⁸

The use of the G/TSCuPc hybrid as an agent for photothermal and photodynamic therapies has been further examined. As presented in Figure 24, the hybrid irradiated at 650 nm in a water solution can raise the temperature of the solution close to 55 °C after 10 min of irradiation.¹⁰⁸

In comparison with G, the noncovalent interactions of aromatic chromophores with GO or rGO provide different results. G does not exhibit any photoluminescence activity, and π stacking of aromatic molecules results in the quenching of their fluorescence emission as described above. On the other hand, GO, due to its chemical structure, exhibits a broad fluorescence band with λ_{max} around 600–700 nm (attributed to π - π^* transition), and in some cases a second more intense band has been recorded near 450 nm (attributed to n - π^* transition). The quantum yield of the photoluminescence of GO is generally

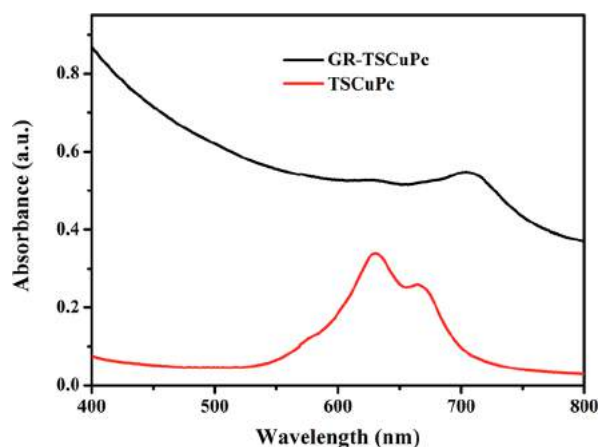


Figure 23. UV-vis spectra of TSCuPc and the hybrid G/TSCuPc. Reprinted with permission from ref 108. Copyright 2014 Royal Society of Chemistry.

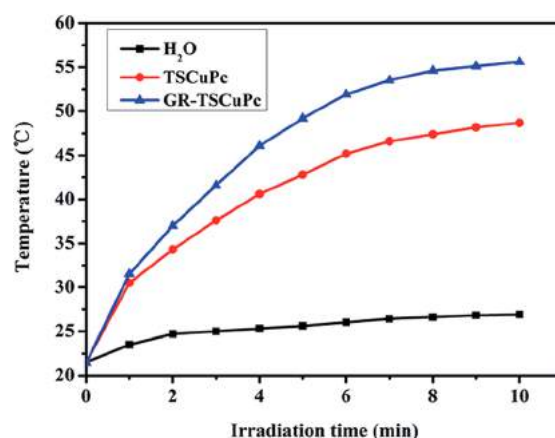


Figure 24. Time-dependent photothermal curves of G/TSCuPc and TSCuPc solutions. Reprinted with permission from ref 108. Copyright 2014 Royal Society of Chemistry.

small, and during reduction to rGO it is further lowered while the fluorescence bands are tuned to shorter wavelengths.^{109–111}

The π - π interactions of rGO with chromophores seem to enhance the fluorescence emission of rGO, while, at the same time, quenching the fluorescence band of the chromophore. A characteristic example of this behavior is recorded by examining the interaction of riboflavin with rGO. Riboflavin (Rb) (vitamin B12) is an amphiphilic organic molecule that consists of a hydrophilic hydroxylated aliphatic chain and a hydrophobic aromatic isoalloxazine part that causes the effective π stacking of Rb on rGO. By excitation at 375 nm, the rGO/Rb hybrid showed a strong emission band at 430 nm remarkably more intense than that of rGO in the same region, while the fluorescence band of Rb, which normally appears near 530 nm, is almost quenched (see Figure 25).¹¹²

3.2. van der Waals, Ionic Interactions, and Hydrogen Bonding

Apart from the aromaticity that is involved in the π - π interactions, G is also characterized by its hydrophobic character, which promotes interactions of G with hydrophobic or partially hydrophobic organic molecules such as surfactants, ionic liquids, or macromolecules. These interactions are mostly used for the dispersion of G nanosheets in both aqueous and organic media or their incorporation in polymers. These hydrophobic interactions

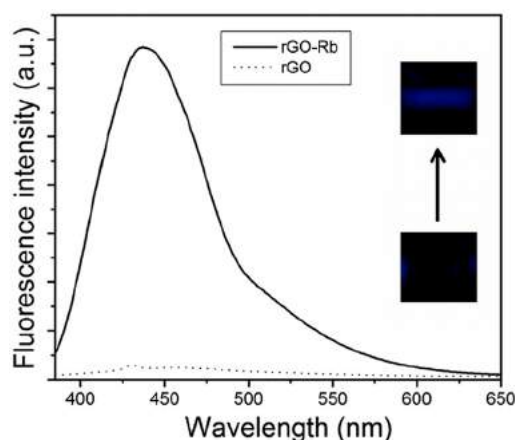


Figure 25. PL spectra of the rGO/Rb hybrid and rGO. Reprinted with permission from ref 112. Copyright 2013 Elsevier B.V.

are also found in rGO, which is closer to G as regards aromatic character and hydrophobicity than GO, which has only a few aromatic regions on its surface and is hydrophilic. GO and, to a lesser degree, rGO also have a number of ionic groups, that is, mainly carboxylate and hydroxylate, which can take part in ionic interactions or hydrogen bonds with the analogous ionic parts of molecules or macromolecules.

The hydrophobic interaction of G or rGO with the aliphatic part of surfactants is often used to achieve an enhanced stability of G or rGO in water. The hydrophilic part of the surfactant responsible for this interaction could be an ionic, zwitterionic, or highly polar group.¹¹³ Cellulose derivatives,^{114–116} lignin,¹¹⁴ albumin,¹¹⁴ sodium cholate,¹¹⁷ and sodium dodecyl benzenesulfonate¹¹⁸ are just some of the amphiphilic organic molecules and macromolecules that have been used successfully as G dispersants and stabilizers.¹¹⁹ Bourlinos et al.¹¹⁴ have shown the stable dispersion of pristine G nanosheets with albumin or sodium carboxymethyl cellulose in water. Using liquid exfoliation technique, Lotya et al.¹¹⁷ have achieved the stable dispersion of 0.3 mg mL⁻¹ of pristine G nanosheets, with an average thickness of 4 layers, in water using sodium cholate as surfactant.

Stable aqueous suspensions of rGO have also been produced by the assistance of several lignin and cellulose derivatives. Sodium lignosulfonate (SLS) is an amphiphilic polymer, which is attached on rGO by both hydrophobic and π - π interactions due to the coexistence in the macromolecule of aromatic and aliphatic parts. The sulfonic groups of this polymer are responsible for the dispersion of the composite in water. Similarly, sodium carboxymethyl cellulose, a natural polysaccharide, can be attached to G, and stable water dispersions are formed. It should be noted here that π - π stacking is not involved because cellulose is totally aliphatic. Finally, hydroxypropyl cellulose is able to disperse rGO, but the resulting composite is not stable in water unless the cellulose is primarily functionalized with pyrene groups. In this case, the polysaccharide is better attached onto the G surfaces thanks to enhanced π - π interactions, and the resulting composite is stable in water.¹²⁰

On the other hand, when an amphiphilic molecule is attached to the graphenic surface by ionic interactions, the hydrophobic part enhances the stability of G in organic solvents. A representative example is the work of Liang et al.¹¹⁵ who showed that GO and rGO can be functionalized with quaternary ammonium salts such as tetradecyl-trimethylammonium bromide. The positive “heads” of the surfactants interact with

carboxylate and hydroxylate groups on GO or rGO through electrostatic interactions, while the aliphatic chains of the surfactants provide G with the necessary lipophilicity and stability in organic solvents.¹¹⁵

Ionic interactions also occur between end functionalized polymers, such as amine terminated polystyrene, and rGO, which lead to the transformation of the hydrophilic rGO into a lipophilic rGO/polymer composite dispersible in organic solvents (see Figure 26).¹²¹

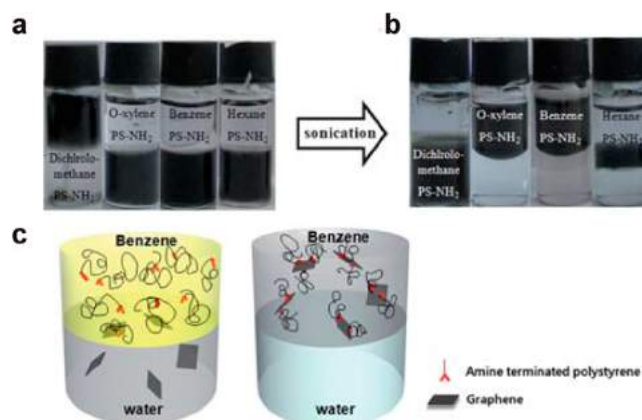


Figure 26. Transformation of the hydrophilic rGO to an organophilic rGO/polymer composite using an amine terminated polystyrene. Reprinted with permission from ref 121. Copyright 2010 Royal Society of Chemistry.

4. NONCOVALENTLY FUNCTIONALIZING AGENTS OF GRAPHENE AND GRAPHENE OXIDE

4.1. Functionalization with Polymers

G derivatives usually have excellent mechanical, thermal, and electrical properties. A simple way to utilize these properties is their incorporation in polymer composites. A key factor for the ideal incorporation of graphenic nanostructures into polymer matrixes is the covalent or noncovalent interactions, which determine the homogeneity of the composite and the extent of the cooperation between the two components. The existence of π - π interactions between graphenic derivatives and polymers that contain aromatic rings is an excellent example in this case. A repeating aromatic polymer unit can strongly bind graphenic monolayers leading to highly homogeneous polymer composites with enhanced mechanical, electrical, and thermal properties.^{122–125} Kevlar is a characteristic polymer with aromatic rings, which can interact strongly with G by π stacking as presented in Figure 27. Lian et al.¹²² have used a Kevlar/graphene nanoribbon (GNR) composite to reinforce polyvinyl chloride (PVC). The afforded Kevlar/GNR/PVC composite (containing 1 wt % GNR) demonstrated an increase of about 72.3% and 106% in Young's modulus and yield strength, respectively.

The sulfonated derivative of polyaniline can also interact with G through π stacking providing a water dispersible composite.¹²⁶ Zhang et al.¹²³ used a series of phenyl or pyrene terminated functionalized polyethylene glycols (f-PEG) to interact with rGO via π stacking (see Figure 28). The pyrene groups were attached onto the G surface, while the flexible ethylene glycol chains allowed interconnection of the nanocomponents, thereby affording a stiff composite with enhanced mechanical properties.

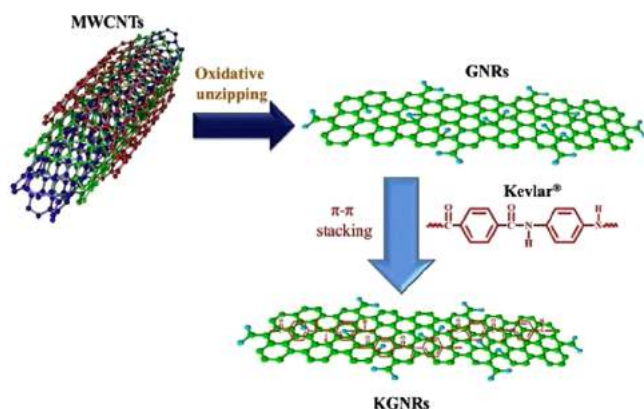


Figure 27. Interaction of Kevlar with graphene nanoribbons. Reprinted with permission from ref 122. Copyright 2014 Elsevier B.V.

The electrical conductivity of these polymer composites is a result of the mixture of a nonconductive component such as the polymer and a conductive part such as G. The authors also studied the role of the aromatic end groups in the electrical conductivity of the final product. As shown in Figure 29, apart from the decrease of the conductivity as the amount of the polymer increased, the aromatic end groups influence the conductivity of the material with the terminal phenyl group giving the most favored conductivity.¹²³

Polymers without an aromatic part have been also reinforced with G or rGO nanosheets. For example, cetyltrimethylammonium bromide surfactant (CTAB) has been used to disperse GO or rGO into natural rubber providing a polymer composite with improved electrical, chemical, and mechanical properties.¹²⁷ Surfactant-assisted mixing has been also used to disperse surfactant functionalized rGO into water-soluble polyurethane (WPU, polyurethane functionalized by sulfonate groups). The

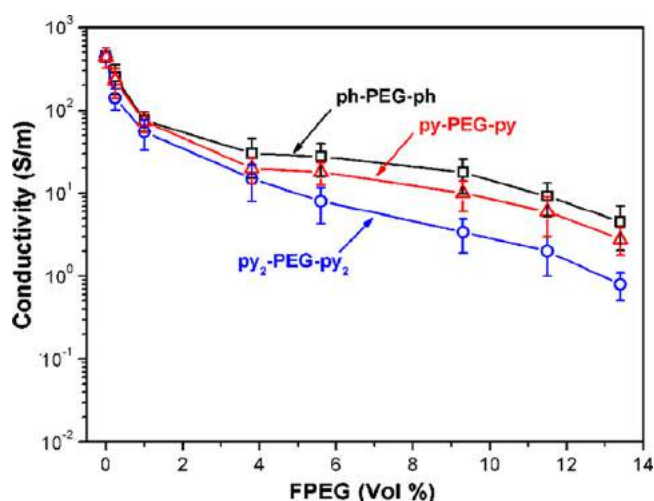


Figure 29. Electrical conductivity of the PEG/rGO composites with different polymer loadings. Reprinted with permission from ref 123. Copyright 2015 Elsevier B.V.

ionic interaction between the sulfonate group of WPU and the tertiary amine group of the surfactant is the driving force for the homogeneous dispersion (see Figure 30).¹²⁸

4.2. Functionalization with Biomolecules

In a manner similar to polymer composites, G and rGO have been combined successfully with biomolecules. For example, heparin is a biomolecule, which consists of a relatively hydrophobic cellulose backbone that is covered by a dense hydrophilic net of negatively charged carboxylates and sulfonate groups. The interaction of rGO and heparin is favored by the hydrophobic character of the heparin backbone and the rGO surface, while the repulsive forces between the charged surfaces of the composite keep it stable in aqueous biological media

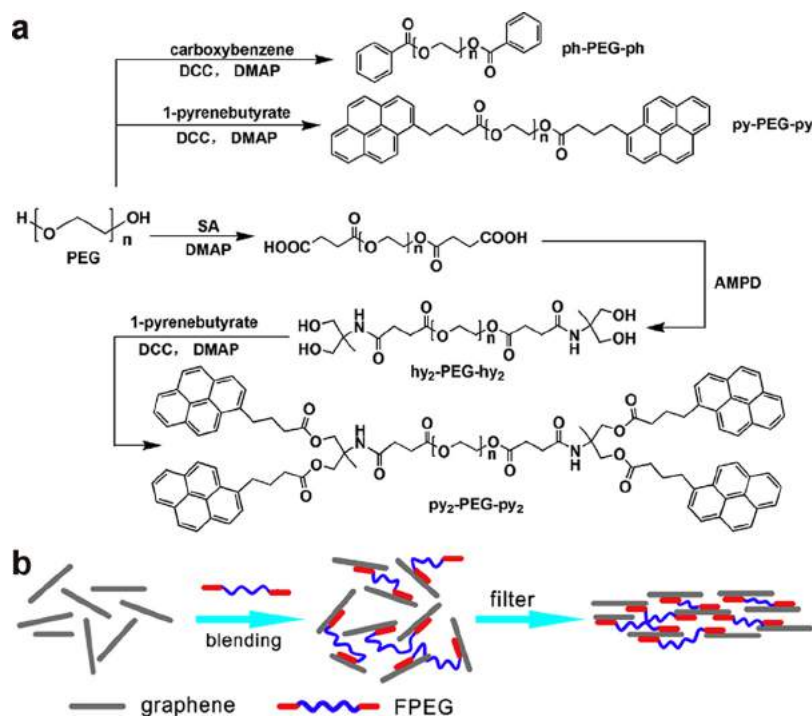


Figure 28. (a) Synthetic procedure of adding aromatic end groups to polyethylene glycol and (b) schematic presentation of the f-PEG/rGO composite formation. Reprinted with permission from ref 123. Copyright 2015 Elsevier B.V.

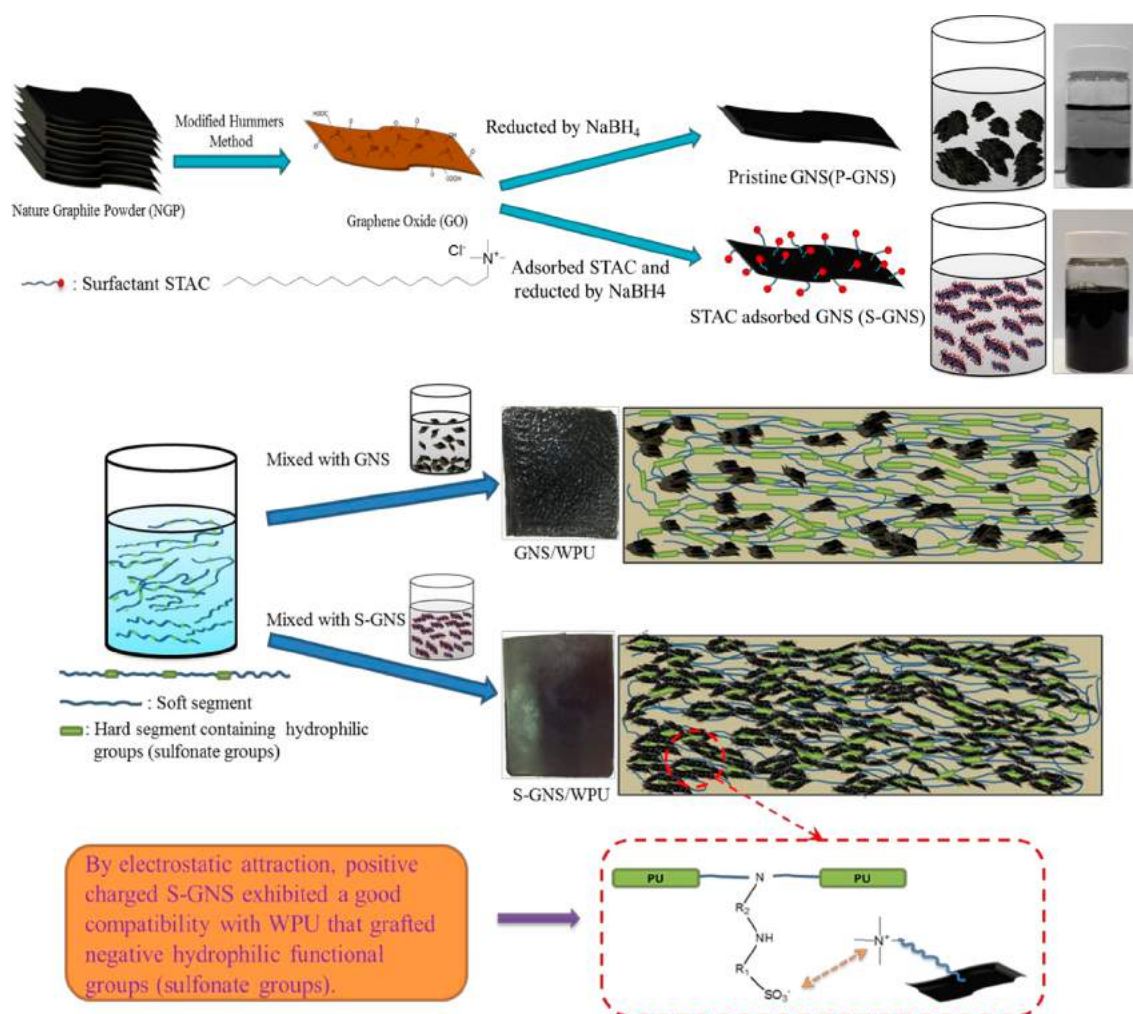


Figure 30. Preparation of a composite material with waterborn polyurethane and surfactant covered rGO. Reprinted with permission from ref 128. Copyright 2013 Elsevier B.V.

dispersion.¹²⁹ Hydrophobic interactions are also responsible for the immobilization of horseradish peroxidase on rGO.¹³⁰ When GO is used instead of rGO, the immobilization of enzymes such as horseradish peroxidase and lysozyme is dominated by strong electrostatic and hydrogen-bond interactions between oxygen groups of the GO and nitrogen groups of the enzymes (see Figure 31).¹³¹

On the other hand, biomolecules with aromatic parts can interact with G through π - π interactions. A characteristic case is the immobilization of glucose oxidase on G.¹³² Dopamine is a biological substance with remarkable contributions in the central nervous, renal, and hormonal systems, it acts as a neurotransmitter, and thus its detection and quantitative determination is very important for human health.¹³³ Usually, its presence is accompanied by the presence of ascorbic acid in much higher concentrations that cause interferences in the detection of dopamine. Electroanalysis has been used to establish effective methods for the determination of biological molecules with electrochemical activity, such as dopamine and ascorbic acid. The role of G here is very important because it has been shown that electrodes covered with G can discriminate between the presence of dopamine from that of ascorbic acid-based, due to the selective π - π interactions of dopamine with the graphenic surface. In this way, G modified electrodes can be used as selective sensors of dopamine in the presence of ascorbic acid

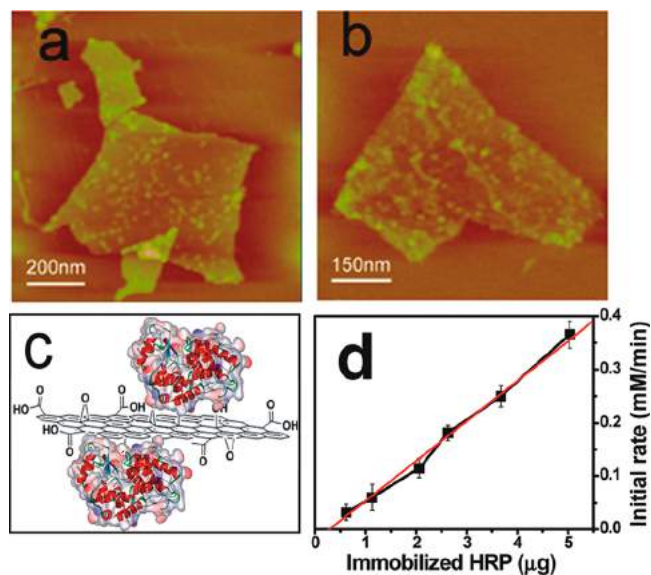


Figure 31. Tapping mode AFM images of horseradish peroxidase (HRP) immobilized on GO at (a) small and (b) large enzyme loadings. (c) Schematic model of the GO-bound HRP. (d) Initial reaction rates of GO-bound HRP versus HRP concentration. Reprinted with permission from ref 131. Copyright 2010 American Chemical Society.

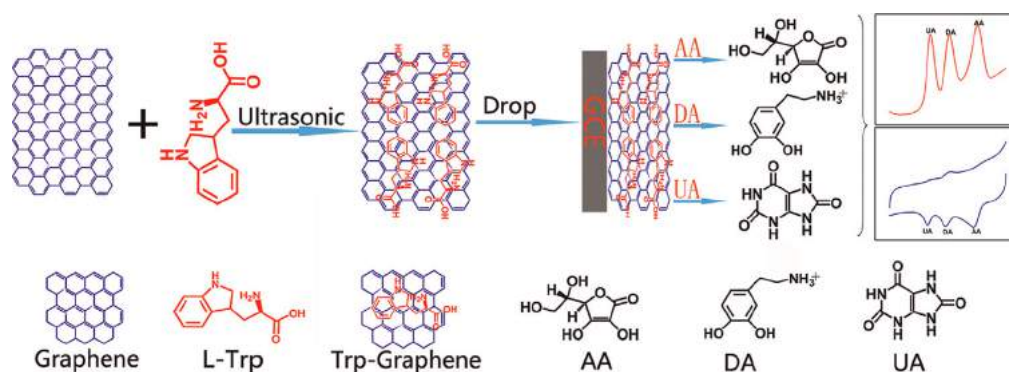


Figure 32. Deposition of tryptophane/G on a glassy carbon electrode (GCE) for the determination of dopamine. Reprinted with permission from ref 136. Copyright 2014 Elsevier B.V.

that does not interact with the G surface.^{134,135} The linear range of these electrodes varies from 5–200 μM ,^{134,135} and a detection limit of close to 2.64 μM has been reported.¹³⁴ G has been further modified to achieve better analytical results with regards to the determination of dopamine in the presence of other biological molecules.^{136–140} The role of π – π interactions in these materials is also decisive. As shown in Figure 32, tryptophane can be attached by π stacking onto the G surface, and then this composite material is used to modify the electrode surface.¹³⁶ In this way, the linearity for the determination of dopamine ranges between 0.5 and 110 μM , and the detection limit is 0.29 μM .¹³⁶ Similar results have been achieved for an electrode coated with G modified with 3,4,9,10-perylenetetracarboxylic acid (PTCA).¹³⁷

In another approach, water-soluble porphyrin and rGO have been examined as an electrochemical detector for the determination of dopamine. The electrode formed in this study displays a detection limit of 9×10^{-9} M and a linear range between 10^{-6} and 7×10^{-5} M. Importantly, the detection of dopamine was not influenced by the presence of other interfering compounds such as uric and ascorbic acid.¹³⁸ Interesting results have also been reported for a hemin modified G electrode. Hemin is an iron-containing protoporphyrin known by its existence in the active site of heme protein.¹³⁹

A great development has been recorded the last years in the area of hybrid nanomaterials based on the interactions of graphenic nanostructures with DNA probes. Single-stranded DNA (ss-DNA) macromolecules are easily immobilized on the surface of graphenic layers through π – π interactions between the hexagonal cells of G or GO and the aromatic bases.¹⁴¹ Such G or GO/ss-DNA hybrids have been used as biosensors for the detection of DNA sequences that are linked to several diseases and genetic disorders based on the strong interactions that developed between the complementary DNA strands. G or GO/DNA hybrids as biosensors have been presented in detail in several significant review articles.^{142–144}

In a characteristic example, Yang et al. showed that the fluorescence quenching of a dye labeled ss-DNA after the interaction with a GO surface was recovered in the presence of the complementary target DNA due to the interaction of complementary DNA strands, as presented in Figure 33. The presence of a noncomplementary ss-DNA has no effect on the situation of the hybrid.¹⁴⁵

Pumera et al. have also developed G platforms for the detection using as detection techniques the electrochemical impedance spectroscopy (EIS)^{146–149} or the redox properties of GO.¹⁵⁰ Here, a very sensitive detection technique such as EIS and hairpin shaped DNA probes, which offer high selectivity, are

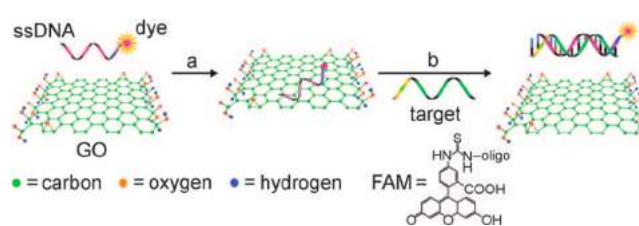


Figure 33. Schematic representation of the target-induced fluorescence change of a dye labeled ssDNA/GO hybrid. FAM is the fluorescein-based fluorescent dye. Reprinted with permission from ref 145. Copyright 2009 Wiley-VCH.

combined successfully in the detection of immunoglobulin (IgG) and DNA single nucleotide polymorphism, which is correlated to the development of Alzheimer's disease.

A very simple electrochemical detection of a DNA sequence is described in Figure 34. The surface of three electrodes was covered by ssDNA through π – π interactions and then was exposed to complementary, one-mismatch target, and non-complementary target DNA, respectively. The three electrodes then are exposed to a suspension of GO nanoplatelets. The electrode with the complementary DNA strands has significantly different behavior due to the interactions of the complementary DNA strands. In fact, the interaction of the complementary DNA strands favors the formation of double strands on the electrode surface, which have much lower conjugation ability with the free GO nanoplatelets in comparison with the electrode exposed to the noncomplementary target that remains covered by single strands. This different behavior in the electrochemical reduction of GO was recorded by cyclic voltammetry.¹⁵⁰

In a different approach as regards their interaction with biomolecules, GO has been presented to work successfully as modulators against protein misfolding and aggregations known as amyloidosis which, are correlated with Alzheimer's¹⁵¹ and other similar diseases.^{152,153} GO has been shown to prevent in vitro the amyloid fibril formation in peptide solution thanks to noncovalent interactions between graphenic nanostructures and peptides that overcome peptide interactions. Furthermore, according to recent work, the modulation effect of GO seems to be size dependent with the large GO nanostructures having a better function on $A\beta_{33-44}$ aggregation than GO with size of less than 50 nm (see Figure 35).¹⁵⁴

4.3. Functionalization with Drugs

An interesting application of graphenic nanostructures is their utility as platforms for the stabilization and the delivery of organic molecules that are used as drugs in therapeutic protocols. This

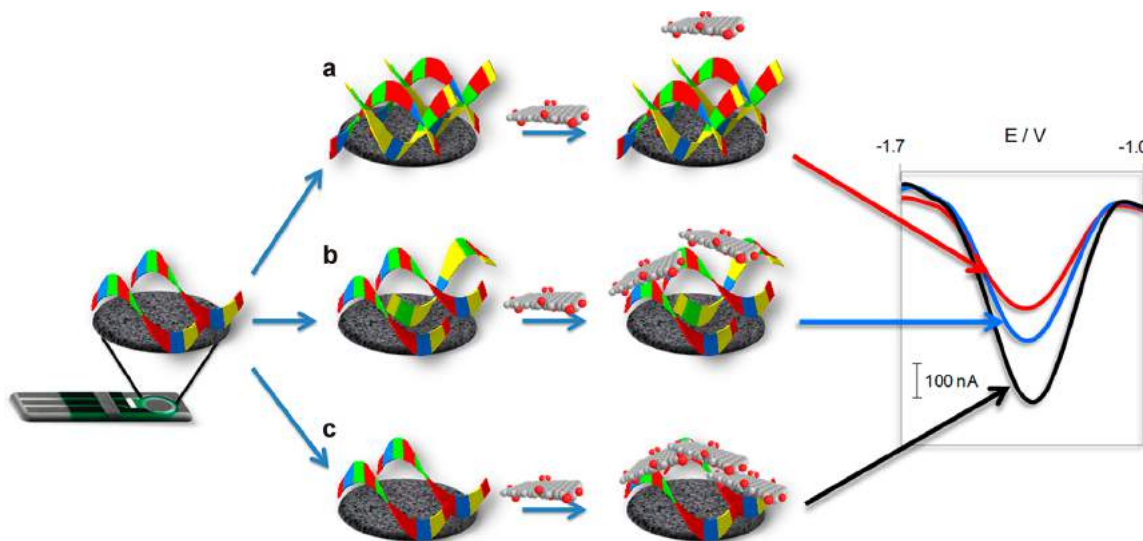


Figure 34. Electrochemical behavior of GO nanoplatelets after the interaction with ssDNA modified electrodes exposed to (a) complementary, (b) one-mismatch, and (c) noncomplementary targets. Reprinted with permission from ref 150. Copyright 2012 American Chemical Society.

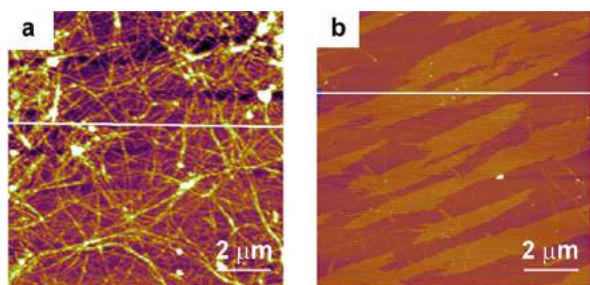


Figure 35. AFM images showing (a) the formation of fibrils after aggregation in a solution of $A\beta_{33-44}$ peptide and (b) the absence of fibrils when in the peptide solution with GO nanoplatelets. Reprinted with permission from ref 154. Copyright 2015 Wiley VCH.

specific role needs two important requirements from the graphenic nanostructures: a covalent or a noncovalent interaction with the organic molecules and the necessary hydrophilicity that promotes the easy dispersion of the hybrid in water or biological fluids. The hydrophilic character of GO is ensured by its carboxylate and hydroxylate groups, while pristine G or rGO has to be functionalized with hydrophilic groups or polymers before their use as drug delivery platforms. As regards the immobilization of the molecules, noncovalent interactions such as π - π stacking are preferable in most cases (i.e., precondition of the aromatic character of the molecule) because the release of the molecules is much easier to manipulate in comparison with that of covalently bonded molecules on the graphenic surface. Ramisol is an example of an aromatic organic molecule with antimicrobial and antioxidant activity that can be attached to G by π - π stacking.¹⁵⁵ The three carboxylates, present at the ends of the molecule, offer the necessary water solubility for the pristine G nanosheets (see Figure 36).¹⁵⁵

Hypocrellins are naturally occurring perylenequinonoid pigments that have been intensively studied as photosensitizers in photodynamic therapy. They include two similar molecular structures, hypocrellin A and B, and their major advantage is the very high quantum yield in the production of singlet oxygen. Although hypocrellins are highly active toward many kinds of tumor cells, their use in vivo is almost prohibited by its poor

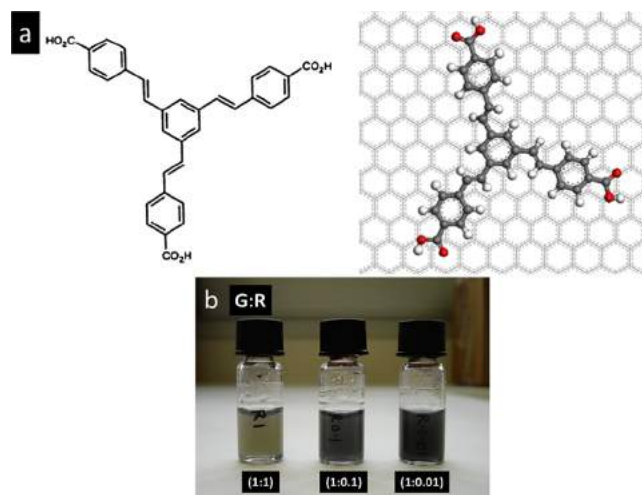


Figure 36. (a) Molecular structure of Ramisol and the hybrid with a G layer. (b) Dispersion of the hybrid in water with different ratios. Reprinted with permission from ref 155. Copyright 2015 Elsevier B.V.

solubility in water. Zhou et al.¹⁵⁶ showed that hypocrellins can be made more water-soluble by interaction with a GO surface mainly by π - π interaction as well as hydrogen bonds between the hydrogen and the oxygen groups of both components (see Figure 37). In vitro experiments showed an effective uptake of GO/HB into the tumor cells and the subsequent damage upon irradiation.¹⁵⁴

Water dispersible PEGylated graphene nanoribbons have been also used as platforms for the effective delivery of luanthone (a thioxanthone-based antitumor drug that targets base excision repair enzyme APE-1 (Apurinic endonuclease-1)) into glioblastoma multiformae (GBM) cells. The aromatic character of luanthone favors the stabilization of large amounts of the drug on the graphenic platform by π stacking (310 μ m onto each mg of G material).¹⁵⁷

Quercetin is a natural product of the family of bioflavonoids found in fruits and vegetables. It is well-known for its antioxidant and anticancer activity as well as for a broad range of health benefits. Even though quercetin has hydroxyl groups, it has low

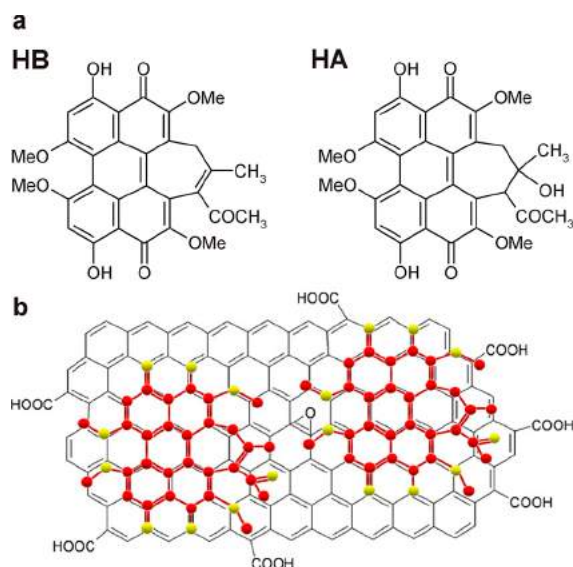


Figure 37. (a) Molecular structure of hypocrellin A and B. (b) Schematic representation of the GO/HB hybrid. Reprinted with permission from ref 156. Copyright 2012 Elsevier B.V.

solubility in water and serious instability in the intestinal fluids. Rahmanian et al.¹⁵⁸ showed that quercetin can be immobilized onto a GO surface by π stacking, and the formed hybrid showed the necessary stability in physiological solutions and no toxicity in vitro.

Enhanced hydrophilic character and biocompatibility can be achieved with GO after its covalent functionalization by PEG chains. The PEGylated GO was then modified with an insoluble aromatic molecule SN38 (a camptothecin analogue) with anticancer activity, and water solubility was achieved.¹⁵⁹ The anticancer drug CPT has been also immobilized on pristine G nanosheets functionalized by dihydroxy phenyl groups that induce hydrophilicity.¹⁶⁰ Other drugs that have been attached by π - π stacking on G or GO surfaces are doxorubicin¹⁶¹ and ellipticine.¹⁶²

Koninti et al.¹⁶² have presented the effective loading of ellipticine (an anticancer drug) on GO and its release to intracellular biomolecules like DNA/RNA. Ellipticine (E) is an aromatic alkaloid that is stable in two forms (i.e., neutral and protonated), intercalates DNA, and acts as topoisomerase II inhibitor (see Figure 38). E is characterized by a strong dual photoluminescence while its λ_{max} moves between green and blue or dark blue upon interaction of the molecule with GO, proteins, DNA or RNA, and sugar. As presented schematically in Figure 38, when the green emitting protonated E ($\lambda_{\text{max}} = 520$ nm) is immobilized on GO in the neutral form by π - π interactions, it is not fully quenched as expected but still emits blue light with λ_{max} at 450 nm. The interaction of DNA or RNA with the GO/E sample resulted in the return of the green fluorescence emission ($\lambda_{\text{max}} = 520$ nm) in the complex showing the progressive release of E from GO surface and its strong interaction with these biomolecules. The addition of serum albumin protein (HSA) in the GO/E sample strengthened the luminescence of the complex, which is not shifted in the presence of DNA, showing that the protein can protect E from unwanted release (see Figure 38).¹⁶²

4.4. Functionalization toward 3D Superstructures

Noncovalent interactions have been used for a special kind of nanoarchitecture creating superstructures based on G or GO

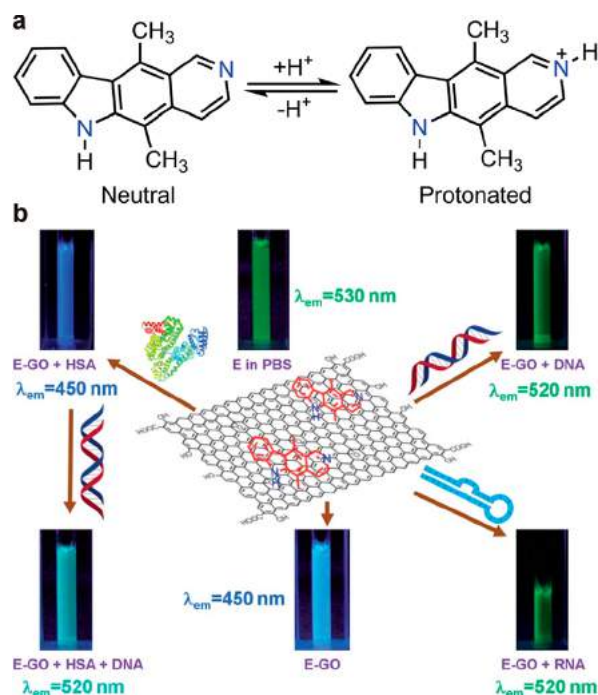


Figure 38. (a) Neutral and protonated forms of ellipticine. (b) Photoluminescence of E free and after its π - π interaction with GO and changes in the presence of HSA, DNA, RNA, or HSA and DNA. Reprinted with permission from ref 162. Copyright 2014 Royal Society of Chemistry.

nanosheets. In these structures, several aromatic molecules have been used as bridges, linkers, and spacers between graphenic sheets and other surfaces.

Noncovalent interaction has often been used to promote the use of small aromatic molecules such as pyrene derivatives as linkers for the connection of graphenic layers to other bodies. Chia et al.¹⁶³ have presented a pyrene derivative as a linker between G and glucose oxidase in a bioelectrochemical sensor of glucose (see Figure 39).

In a similar approach, pyrene groups can form a bridge between G layers and a gold electrode (see Figure 40).^{164,165}

Porphyrin functionalized rGO has also been used as biosensor for glucose in human serum thanks to its excellent electrocatalytic activity toward the reduction of dissolved oxygen.¹⁶⁶ Thanks to their aromatic part, cyclophanes can be entrapped between graphenic layers forming a characteristic host-guest 3D superstructure. The driving force here is the π - π interactions between the aromatic system of cyclophane and that of CBDAP⁴⁺/GO. A cyclophane with diazapyrenium and benzene units (see Figure 41) has been shown to interact effectively with GO nanosheets forming a supramolecular organogel. The position of cyclophane between the two GO nanosheets is suggested by the arising distance of 13.3 Å as estimated by the powder X-ray diffraction analysis of the superstructure.¹⁶⁷

4.5. Functionalization with Carbon Nanoallotropes

Carbon nanotubes have a strong aromatic character that promotes π - π interactions, although their curved shape deteriorates this trend. In general, there is a remarkable noncovalent interaction between carbon nanotubes and G nanostructures that leads to stable superstructures of these carbon hybrids. Several nanoarchitected aerogels, foams, thin films, membranes, and paper-like sheets constructed by a combination of graphenic nanostructures and carbon nanotubes

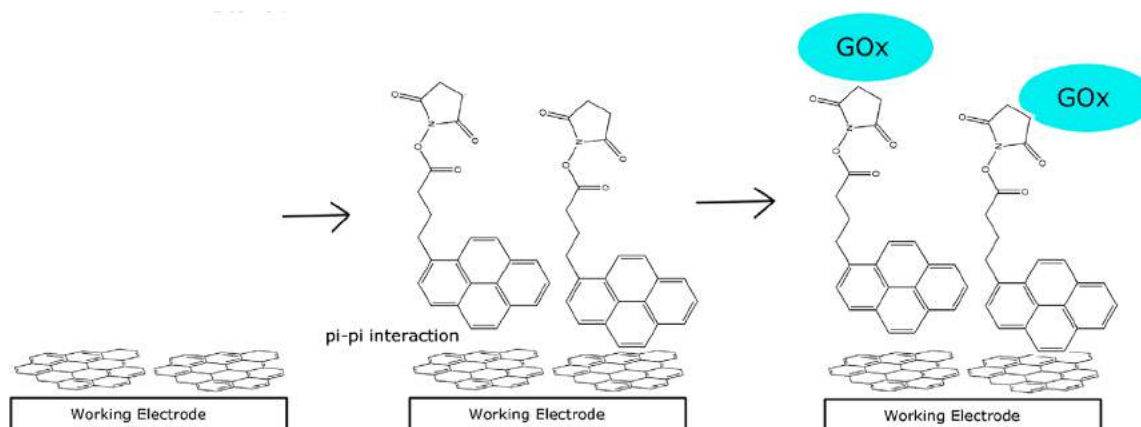


Figure 39. Pyrene links graphene and glucose oxidase through π - π stacking. Reprinted with permission from ref 163. Copyright 2015 Elsevier B.V.



Figure 40. Pyrene interconnection between G and gold electrode. Reprinted with permission from ref 164. Copyright 2013 Elsevier B.V.

have been described in a recent review.¹⁶⁸ For example, the presence of dispersed SWNTs in a suspension of GO in water during hydrothermal reduction of the GO to rGO resulted in the formation of an aerogel superstructure after solvent removal by a freeze-drying procedure (see Figure 42).¹⁶⁹

Georgakilas et al. has recently developed a hybrid nanostructure by combining hydroxy functionalized multiwalled carbon nanotubes (MWNTs) with pristine G through π - π interactions; the as-formed material exhibited high dispersibility in water and remarkable electrical conductivity (see Figure 43).¹⁷⁰ The hydrophobic G nanosheets are covered by the hydrophilic MWNTs affording a hydrophilic hybrid. Furthermore, the MWNTs act as conductive interconnectors between the G layers, improving the conductivity of the final hybrid.¹⁷⁰

Hydrophilic GO has been also used for the creation of stable dispersions of nonpolar pristine carbon nanotubes in water through π - π interactions.¹⁷¹ The electron acceptor [6,6]-phenyl- C_{61} -butyric acid methyl ester (PCBM) is the most commonly used fullerene derivative in bulk heterojunction

polymer solar cells (BHJ-PSC).^{172–175} G could be used in combination with PCBM, offering an excellent road for charge transportation during the solar cell function. Yang et al.¹⁷⁶ used a pyrene derivative of PCBM for its better adhesion onto rGO through π - π stacking, although fullerene derivatives could be also stacked onto the G surface (see Figure 44).

From the two possible configurations presented, microscopic and spectroscopic data show that the proposed structure is that where C_{60} is kept far from the G surface and pyrene is the adhesion medium. The use of the hybrid in BHJ solar cell increases the efficiency 15%, while the use of pyrene-PCBM or rGO separately decreases the efficiency. However, as mentioned above, C_{60} moieties can be grafted on graphenic surfaces by π -stacking without the use of other aromatic linkers. A simple grinding of a mixture of GO and C_{60} led to the formation of a GO/ C_{60} hybrid, which is stable in water at significant concentrations due to the high hydrophilicity of GO that dominates over the hydrophobic character of C_{60} . The GO/ C_{60} hybrid has been used as substrate for the immobilization of phosphotungstic acid (PTA); this material is then electro-deposited to form a thin film electrode of the PTA/GO/ C_{60} composite. PTA is a highly active redox catalyst; therefore, the use of the PTA/GO/ C_{60} composite showed enhanced catalytic activity toward the electrochemical redox reactions of several organic compounds such as dopamine, ascorbic acid, uric acid, etc.¹⁷⁷

Recently, a few-layer G/nanodiamond (FLG/NDs) hybrid has been prepared as a carbon-based catalyst for the steam-free dehydrogenation of ethylbenzene to styrene. The enhanced amount of nanodiamonds that are dispersed on FLG surface is promoted by the large number of defects and vacancies of the FLG. The specific surface area of the hybrid is $330 \text{ m}^2 \text{ g}^{-1}$, much

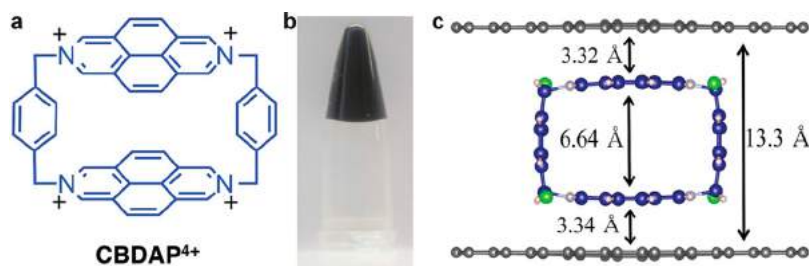


Figure 41. (a) Structure of a cyclophane with diazapyrenium units (CBDAP⁴⁺), (b) photo of CBDAP⁴⁺/GO gel, and (c) representation of the possible position of cyclophane/CBDAP between GO layers. Reprinted with permission from ref 167. Copyright 2014 Wiley-VCH.

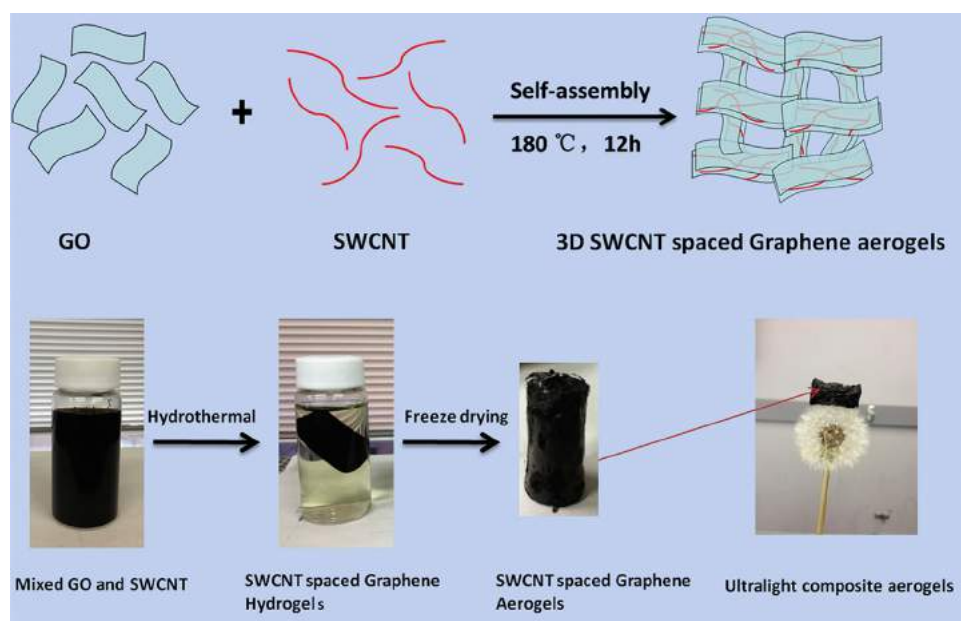


Figure 42. Schematic representation of aerogel formation toward the rGO/SWNT hybrid. Reprinted with permission from ref 169. Copyright 2015 Elsevier B.V.

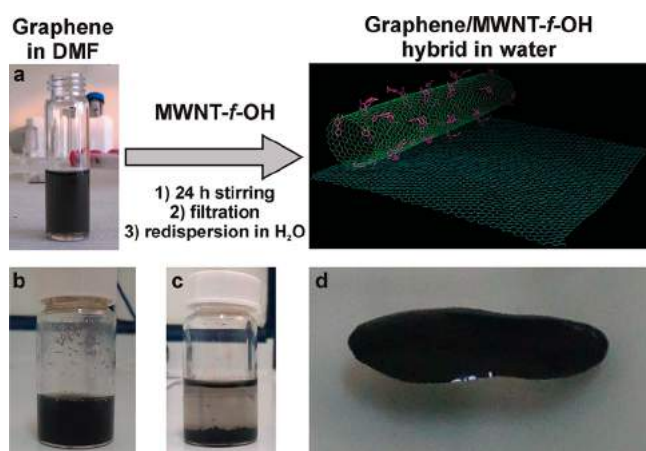


Figure 43. (a) Formation of G/MWNTs-f-OH hybrid and (b) its dispersion in water. (c) Graphene precipitate without MWNTs-f-OH following the same procedure and (d) the hybrid in ethylene glycol at high concentration. Reprinted with permission from ref 170. Copyright 2015 Wiley-VCH.

larger than that of pure FLG, which is about $30 \text{ m}^2 \text{ g}^{-1}$, because NDs are inserted between the FLG layers and prevent restacking. Acting as catalyst, the hybrid showed 4 times higher dehydrogenation activity as compared to unsupported NDs (see Figure 45).¹⁷⁸

Finally, π - π and hydrophobic interactions have been shown to be responsible for the strong attachment on GO of small polyaromatic and oxygenated species, which are coproduced during the oxidative procedure of graphite and usually called oxidative debris.¹⁷⁹ Many researchers have studied the last years the role of the oxidative debris in several properties of the as-prepared GO, revealing a significant contribution such as in water dispersibility,¹⁸⁰ fluorescence,¹⁸¹ electroactivity,¹⁸² and chemical reactivity.¹⁸³ In contrast with the early suggestions about the structure of GO, recent studies have shown that the product of the strong oxidation procedure that was applied on graphite according to the known well-established methods such as

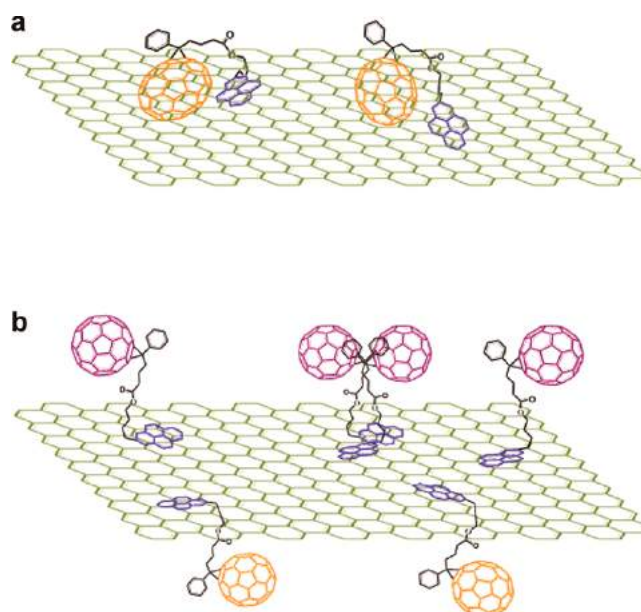


Figure 44. Schematic representation of the two possible conformations of the pyrene-PCBM/rGO hybrid: (a) C_{60} is attached on the graphenic surface simultaneously with the pyrene stacking, and (b) C_{60} is kept far from G and pyrene. Reprinted with permission from ref 176. Copyright 2013 American Chemical Society.

Staudenmaier, Hofmann, Hummers, and Tour oxidations consisted mainly of poorly oxidized large G nanosheets and highly oxidized relatively small aromatic species, which are strongly attached on the surface of GO. It is concluded that most of the oxygen functionalities on the product of graphite oxidation are concentrated on these small polyaromatic species. The so-called oxidative debris has a humic- or fulvic-like structure with carboxy, hydroxyl, and epoxy functionalities anchored to the edges. Because of their large number of hydrophilic oxygen groups, they act as surfactant and contribute to the dispersibility of GO in water. Consequently, pure GO nanosheets that arise

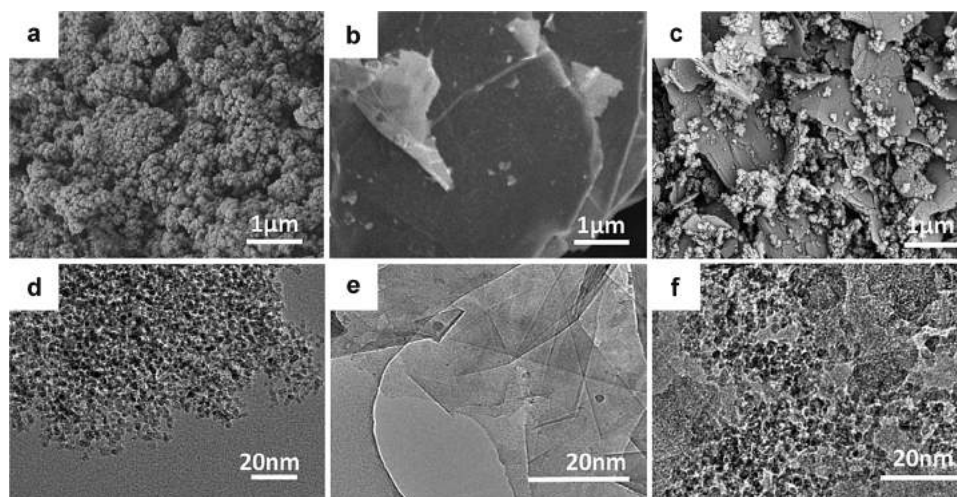


Figure 45. SEM and TEM micrographs of (a,d) bulk nanodiamonds, (b,e) few-layer graphene (FLG), and (c,f) the FLG/NDs hybrid. Reprinted with permission from ref 178. Copyright 2015 Elsevier B.V.

after removal of debris by ultrasonication are not so poorly dispersible in water and more electrically conductive than before debris removal.¹⁷⁹ In addition, Coluci et al.¹⁸³ have shown that pure GO is much more effective in noncovalent interactions.

Pumera et al.¹⁸² showed by using cyclic voltammetry that a stepwise decrement in the inherent electroactivity of GO is observed by increasing the ultrasonication time from 2 to 24 h, which is attributed to the analogous removal of oxidative debris, concluding that inherent electroactivity came mostly from the oxidation debris (see Figure 46).

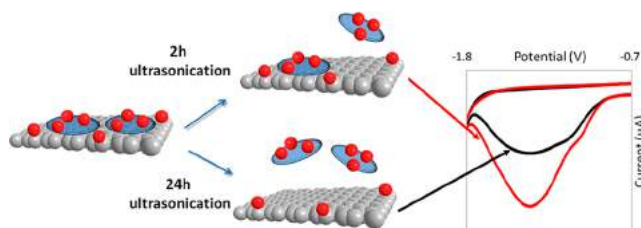


Figure 46. Schematic representation that shows how the removal of oxidative debris is correlated with the reduced electroactivity of GO in cyclic voltammetry. Reprinted with permission from ref 182. Copyright 2014 American Chemical Society.

4.6. Functionalization with 2D Graphene Analogues

The tremendous interest in G inspired researchers to develop 2D inorganic monolayers from transition metal oxides and dichalcogenides that have a layered structure.^{69,184,185} The atomic thin layers are constructed by covalent bonds between transition metals such as Ni, V, W, Mo, Nb, Bi, Ta, and oxygens or nonmetallic elements such as S, Te, and Se. The layers are held together by van der Waals interactions. Although the layered structure and the properties of these inorganic compounds were known several decades ago, it was only recently confirmed that the monolayered structures can be stable. Additionally, these materials exhibit interesting electronic, magnetic, optical, and mechanical properties different from their 3D analogues. For example, bulk molybdenum sulfide (MoS_2) is an indirect band gap semiconductor, while a MoS_2 monolayered structure has a direct band gap and strong photoluminescence.¹⁸⁶ This observation gave the necessary motivation for the development of inorganic 2D materials for potential application in

optoelectronics devices, catalysis, photovoltaics, batteries, etc. A recent review on 2D materials has been presented by Gupta et al.¹⁸⁴ where synthetic methods, characterization techniques, properties, and applications are described.

Supporting the similarity with G, 2D inorganic materials can be produced by methods such as mechanical cleavage,^{187–189} liquid phase exfoliation (see Figure 47 and Figure 48),^{69,190,191} chemical vapor deposition (CVD),^{192,193} and molecular beam epitaxy.¹⁹⁴

The next step following the deconstruction of graphite and inorganic layered materials down to G and inorganic monolayers, respectively, was the reorganization of the different monolayers into new 3D or few layered 2D heterostructured hybrids with combined properties. The advantage of this research is that the properties of the final hybrid can be predetermined by a careful selection of the starting components and the way that they are placed in the hybrid. Up to now, the most used methods for the development of layered heterostructures are CVD growth,^{195,196} and the mechanical transfer or deposition of chemically exfoliated 2D crystals layer by layer.¹⁹⁷ One of the simplest ways to make a hybrid heterostructure is illustrated for the G/ MoS_2 hybrid material, which is produced by bringing in contact a glass slide with micrometer-sized exfoliated G nanosheets and a Si/ SiO_2 substrate decorated by MoS_2 layers mechanically deposited.^{198,199} The G/ MoS_2 hybrid combines the electrical properties of G with the optical activity of semiconductor. Interestingly, a persisted photoconductivity in G was induced, which can be reverted back to the dark state by a voltage pulse application; this results in an electrically controlled photo-induced memory device (see Figure 49).¹⁹⁸

On the other hand, the MoS_2 /G heterostructure where MoS_2 is covered by a layer of G has been applied for the ultrasensitive detection of DNA hybridization,²⁰⁰ as a nanobiosensor,²⁰¹ and a p–n junction.²⁰²

Tungsten sulfide (WS_2) has been also deposited as few layered nanosheet supported on rGO through a hydrothermal procedure. The rGO/ WS_2 hybrid heterostructure showed enhanced electrochemical and rate capability performance as an anode for lithium-ion batteries (LIBs). The characterization of the hybrid is based on X-ray diffraction patterns and Raman spectra, while the two components were also indicated by TEM micrographs. X-ray diffraction mostly indicates the hexagonal

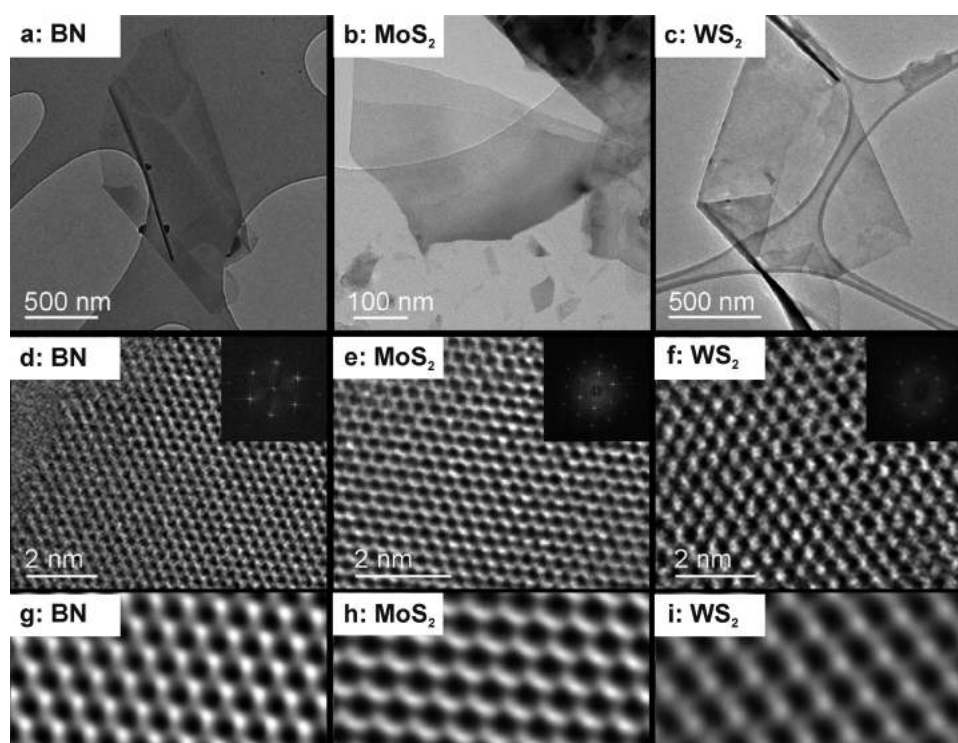


Figure 47. (a–c) Low-resolution TEM images of BN, MoS₂, and WS₂ layered flakes. (d–f) High-resolution TEM images of BN, MoS₂, and WS₂ monolayers. The insets show fast Fourier transforms of the images. (g–i) Butterworth-filtered images of sections of the images in panels (d), (e), and (f), respectively. Reprinted with permission from ref 190. Copyright 2011 American Association for the Advancement of Science.

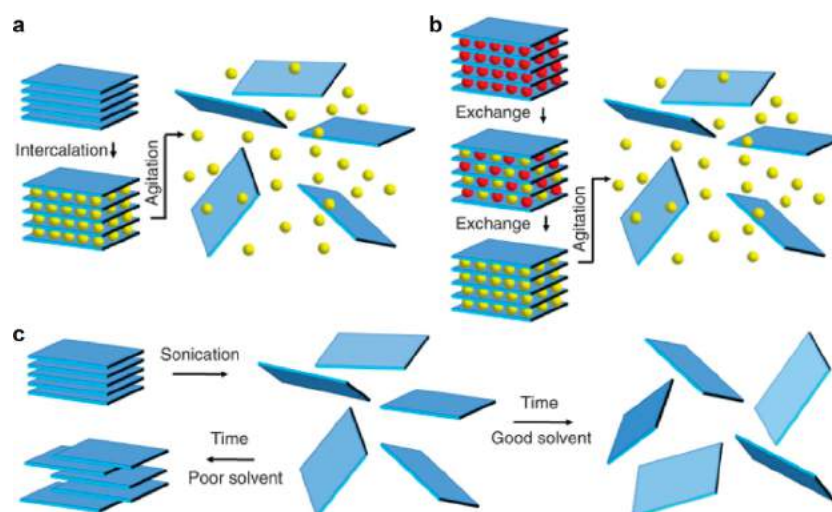


Figure 48. Schematic representation of three similar liquid exfoliation processes based on (a) intercalation, (b) ion exchange, and (c) ultrasonic exfoliation. Reprinted with permission from ref 69. Copyright 2013 American Association for the Advancement of Science.

structure of WS₂ monolayer, while the presence of the (002), (100), and (110) reflections are due to the few layered structure of WS₂ (see Figure 50). The decreased crystallinity of the hybrid due to the presence of rGO in the hybrid is also observed. The Raman spectrum of the hybrid showed the characteristic G and D bands of graphene at 1585 and 1350 cm^{−1}, respectively, and the characteristic band of WS₂ at 350 and 415 cm^{−1} due to the E_{2g} and A_{1g} modes, respectively.²⁰³

The layered structure of these materials offers the opportunity to combine more than two different nanostructures in a 3D assembly. Recently, Roy et al.²⁰⁴ have shown the construction of a field-effect transistor combining G nanosheets with MoS₂ and

h-BN monolayers. G has the role of source/drain and the top-gate contacts, h-BN is the top-gate dielectric, and MoS₂ is the active channel material (see Figure 51).

4.7. Functionalization with Nanostructures

It is well-known that the use of nanoparticles in various applications depends on a multitude of factors such as size, number of facets, facet order, shape, surface area, etc.²⁰⁵ These factors are in turn dependent on a vast number of reaction conditions such as temperature, concentration, time, precursors, and many more. Additionally, in many applications, the use of nanoparticles requires immobilization on a substrate surface. In this regard, G and GO can act as a substrate for nanoparticles in

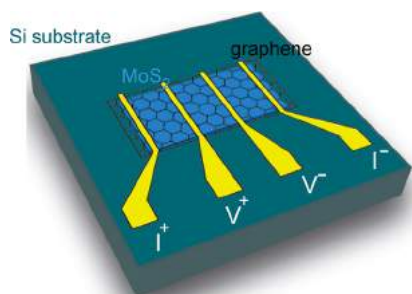


Figure 49. Schematic representation of the device with G and MoS₂. Reprinted with permission from ref 198. Copyright 2013 Elsevier B.V.

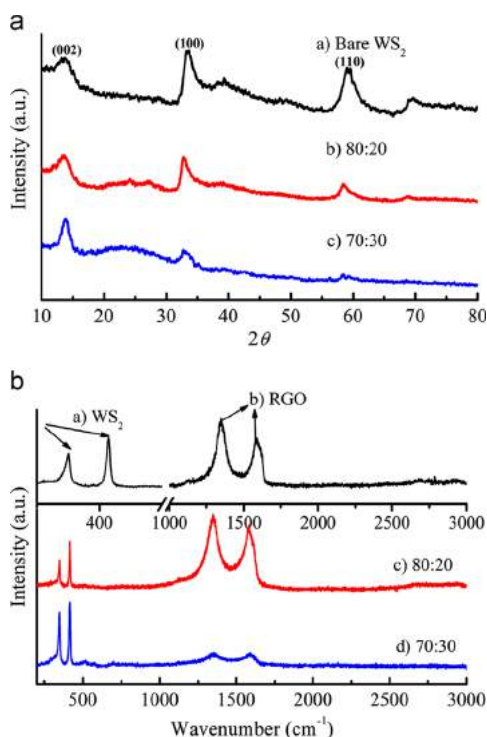


Figure 50. (a) X-ray diffraction patterns and (b) Raman spectra of bare WS₂ and the hybrids WS₂/rGO in two different ratios. Reprinted with permission from ref 203. Copyright 2013 Elsevier B.V.

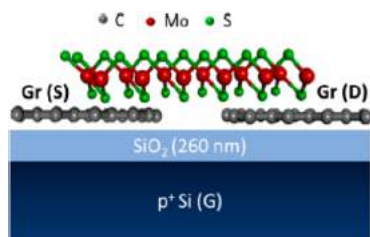


Figure 51. Schematic representation of a field-effect transistor constructed by graphene, MoS₂, and h-BN layers. Reprinted with permission from ref 204. Copyright 2014 American Chemical Society.

many applications where the inherent properties of G, such as conductivity or anchoring sites, could be beneficial.^{206,207}

Depending on the G substrate used, the nanoparticles can either be deposited directly onto the surface or be grown on the surface. For example, it may be easier to grow nanoparticles directly onto the surface when using GO as a substrate, as it has

multiple oxygen functionalities where seeding can take place.²⁰⁸ On the other hand, it may be easier to deposit already grown nanoparticles onto pristine G as it should lack vast numbers of seeding sites.²⁰⁹ Obviously, these two examples are broad generalizations, but they demonstrate the uniqueness of G as a substrate for nanoparticle deposition.

It should be pointed out here that in many reports the nanoparticle deposition claimed as noncovalent could in fact be covalent bonding occurring between the G surface and the nanoparticle. However, multiple groups have not offered detailed confirmation of either covalent or noncovalent bonding between the G surface and the nanoparticle. As such, we present here materials that have been reported either as (i) noncovalent interactions or as (ii) interactions that could be noncovalent based on prior studies.

4.7.1. Synthetic Methods toward Graphene/Nanostructure Hybrids. Multiple methods have been developed to deposit nanoparticles onto G ranging from the traditionally applied chemical solution deposition methods^{210–212} to electrochemical,²¹³ ultrasonication,²¹⁴ and laser synthesis²¹⁵ deposition methods, among many others. In this section, a few of the novel techniques toward G nanoparticle materials are described.

Liu et al.²¹⁶ have demonstrated the simultaneous reduction of GO and deposition of Ag nanoparticles onto the rGO surface using an electron beam method. The authors of this study showed that the resistivity of the Ag/rGO material as well as the Ag nanoparticle size decreased with an increase in electron beam radiation dosage (167.96 and 27.52 nm at 70 and 350 kGy, respectively). The benefits of this method are apparent with the short time needed for synthesis as well as the ease of nanoparticle manipulation by dosage variation. In another study, Hui and co-workers²¹⁴ have shown that Ag nanoparticles of varying sizes can be uniformly deposited onto a GO substrate using ultrasonication in the presence of Vitamin C as a reducing agent. The authors showed that, in general, the size of the Ag nanoparticles is related to ultrasonication time with longer times resulting in larger nanoparticles. This observation of increasing size with ultrasonication time was attributed to the Ostwald ripening process. However, it should be noted that at sonication times above 20 min, both small and large nanoparticles are obtained, and a decrease in uniformity is also observed. The size of Ag nanoparticles deposited on rGO surfaces has been elaborated on further by Haider et al.²¹⁷ who showed that by using very dilute concentrations of AgNO₃ in sequential reduction reactions, a nanoparticle size of 4–50 nm can be obtained. This size modification was shown to be critical to the antibacterial properties of the Ag nanoparticle-rGO material against *E. coli* with an average size of 20 nm proving most efficient.

In another study, Shi et al.²¹⁸ have shown that a CuS/rGO composite can be prepared using a sonochemical method where CuCl₂ and GO were dispersed in ethylene glycol with the use of thioacetamide as a reducing agent. The as-prepared material exhibited a large surface area of 993.5 m² g^{−1} and a much improved methylene blue photocatalytic activity as compared to bare CuS nanoparticles. It should be noted that these sonochemical methods are probably beneficial toward industrial scale synthesis as they can proceed on a large scale and at low synthesis temperatures. GO has also proved to be a suitable substrate for the challenging synthesis of single phase nanoparticles such as Cu₂ZnSnS₄, as demonstrated by Thangaraju and colleagues.²¹⁹ In this study, they showed that Cu₂ZnSnS₄ nanoparticles can either be deposited on GO by sonication in

oleylamine or grown in situ using a hot injection method under a N_2 atmosphere. The benefit of these growth methods for the Cu_2ZnSnS_4 material is that it affords a relatively simple approach whereby one is able to tune the absorption nature of the optoelectronic material.

Multiple groups have coated nanoparticles with polymers or other surfactants, which can then be attached to G-based templates. For example, Bera et al.²²⁰ have shown that rGO can be functionalized with 0D, 1D, and 2D CdS nanoparticles; in this method, the nanoparticles are functionalized with 4-aminothiophenol before sonication with GO and subsequent hydrazine reduction. It should be noted that surfactant use is not limited to nanoparticle modification, with Wang and colleagues²²¹ showing that Pt nanoparticle decorated 3D G assemblies can be obtained when the amphoteric surfactant sodium lauryl aminopropionate (SLA) is used. Initially, the 3D GO structure is formed by sonicating GO with SLA. This formed 3D material was then modified with Pt nanoparticles using a hydrothermal synthesis method, which employs the added sodium lauryl aminopropionate as a reducing agent. On the other hand, it is also possible to modify the G surface with an organic functionality that is then able to attach a nanoparticle through well-known ionic interactions. In this way, Atar and colleagues²²² have shown that a GO modified using 2-aminoethanethiol can be successfully used to attach Fe@Ag core-shell nanoparticles through formation of an Ag-S ionic bond. Through functionalization of GO nanoribbons with cysteamine, it has been shown that Ag nanoparticles can not only be attached to the cysteamine chain through Ag-S bonds, but also on the GO basal surface.²²³ These Ag nanoparticle functionalized GO nanoribbons then assemble into cube-like Ag nanoparticles agglomerates, which are believed to form through the initial cubic shape formation of the cysteamine functionalized GO nanoribbons.

The synthesis of CVD G with nanoparticles deposited on one side (asymmetrically) or both sides (symmetrically) has been reported by Toth et al.²²⁴ Remarkably, the authors showed that in the symmetric deposition of nanoparticles, it is possible to deposit either the same metal or different metals. To obtain the single sided deposition, the authors used a redox reaction, which relied on the simultaneous oxidative etching of the Cu foil on which the G was grown and the reductive deposition of the desired nanoparticles. To deposit the second metal on the opposite side, the asymmetrically deposited G is floated on an aqueous solution containing the desired metal salt; after this flotation an organic layer containing a reducing agent is layered over the G sheet. As such, the second deposition occurs at an aqueous-organic liquid/liquid interface (see Figure S2).

The layer by layer self-assembly of negatively charged CdS quantum dots onto GO modified with poly(allylamine hydrochloride), that is, positively charged, has been reported by Xiao et al.²²⁵ toward forming nanofilms with photoelectrochemical and

photocatalytic applications. This self-assembly method affords the electrodes formed with a highly efficient charge separation under photoelectrochemical conditions due to the stacked nature of the material, which results in close interfacial contact between the rGO and the CdS. The improved charge separation was also noted in the photocatalytic reduction of aromatic nitro compounds, with the CdS/rGO layered material showing almost double efficiency as compared to the layered CdS sample. One of the major challenges facing G materials in photoelectrochemical water splitting applications is the creation of uniform films with active sites for the catalytic oxygen and/or hydrogen reactions, and as such this layer-by-layer method holds promise for future applications.

The deposition of nanoparticles onto doped and/or functionalized G is another important and growing field of research in G nanoparticle systems. In this field of study, noble metal nanoparticles have been deposited on various doped G materials. Normally, nitrogen-doped G is used, see section 4.7.2,^{213,226} and this is probably due to the ease with which N-doped G can be synthesized.^{227,228} The deposition of Pt nanoparticles onto thiol functionalized thermally reduced graphene oxide (TrGO) by the thermal decomposition of the organometallic precursor methylcyclopentadienyl-trimethylplatinum(IV) in ionic liquid systems has been demonstrated by Marquardt et al.²²⁹ In this synthesis procedure, thiol functionalized TrGO with varying amounts of thiol functionality can be achieved using various sulfur sources; it should be noted that the sulfur source used determines the thermal stability of the prepared materials during the high temperature Pt deposition process. The authors believe these methods can be applied to produce catalysts toward fuel cell technology, and as the materials display high thermal stability during Pt deposition this seems a reasonable assumption. In another high temperature process, Bi nanoparticle enriched nanoporous carbon has been formed on TrGO through the thermal decomposition of a Zn containing zeolitic imidazolate framework-8/GO hybrid material, followed by infiltration and chemical reduction of $Bi(NO_3)_3$.²³⁰ This material was then applied in the fabrication of a selective and sensitive heavy metal electrochemical sensor.

A study by Wei and co-workers²³¹ has shown that electrochemically exfoliated G can be functionalized with Si, Fe_3O_4 , and Pt nanoparticles by use of the solution-processable polyaniline emeraldine base (PANB), which provides functionalization sites. The use of the PANB is interesting as it leads to uniform coating of nanoparticles on the G surface, while the coating concentration can be determined by adjusting the ratio of PANB used in the synthesis step. An additional use of the PANB is that it provides unique electrical properties to the G by acting as a dopant. Because of these properties, the Si/PANB/G material was successfully applied in LIBs as an anode, and these properties are further discussed in section 4.7.2.

The growth of precisely aligned AuCN nanowires on CVD G has been reported by Lee et al.,²³² who used a simple room-temperature solution growth method where the graphene substrate is floated on the surface of a precursor containing solution. The nanowires formed have dimensions of approximately $94\text{ nm} \times 10\text{ nm} \times 3\text{ nm}$, and are aligned along the zigzag lattice directions of the graphene. This result is of interest as the precise control of nanoparticles in G-based materials is essential toward novel applications of nanoparticles, as well as G-nanoparticle systems. Additionally, they showed that the G-AuCN nanowire system can be used to create precise G nanoribbons by oxidizing the unprotected G using O_2 plasma

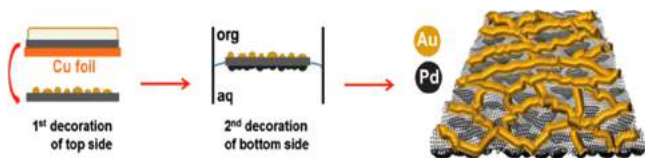


Figure S2. Schematic of the synthesis method used to prepare symmetrically deposited CVD graphene sheets with different metals on either side. Reprinted with permission from ref 224. Copyright 2015 Wiley-VCH.

and then removing the AuCN. The authors also noted that the grain boundaries of G can be visualized using this nanowire technique, with similar results reported by Yu et al.²³³ who showed that the deposition of Au nanoparticles using thermal evaporation can be used to visualize grain boundaries. Importantly, in this study, the authors showed that different types of grain boundaries and wrinkles on the G surface can be differentiated; this is in contrast to previous G boundary visualization studies, which have focused only on defects and not the type of defect present.^{234–236}

A novel method to obtain Ni₃S₂/rGO 3D frameworks using bacteria has been presented by Zhang and colleagues.²³⁷ In this study, *Bacillus subtilis* was mixed with an aqueous solution of nickel acetate and GO, after which the solution was reduced and spray deposited onto a Ni foam substrate (see Figure 53). This

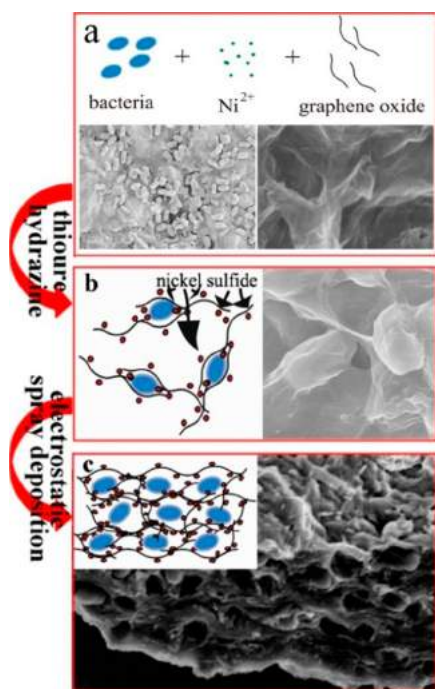


Figure 53. Schematic showing the synthesis of the Ni₃S₂/rGO 3D framework. Reprinted with permission from ref 237. Copyright 2013 American Chemical Society.

porous Ni₃S₂/rGO material was then applied as a supercapacitor with a specific capacitance of 1424 F g^{−1} at a current density of 0.75 A g^{−1}. Additionally, with cycling, that is, 3000 cycles at 15 A g^{−1}, 89.6% of the initial capacitance of 1242 F g^{−1} was still delivered.

Nanoparticles coated with a carbon layer are of importance to Li-ion batteries as well as other applications.^{238–240} Sengar and colleagues²⁴⁰ have shown that metal (Pd or Cu)/G core/shell materials can be produced using a continuous flow gas-phase synthesis setup. The use of a spark generator using Pd or Cu electrodes was applied in this setup to form the metal core, and as such it is possible that this method could be expanded to multiple other metal/G core/shell materials. An additional benefit of this setup is that it employs an electrostatic precipitator, which allowed the authors to deposit the as-formed composite material on any substrate desired. In a study by Moon and colleagues,²⁴¹ it has been shown that Au nanorods coated with rGO, formed using a Xe lamp irradiation process with ammonium hydroxide as a reducing agent, are far more impressive photoacoustic

bioimaging agents than uncoated Au nanorods. The authors believe the photoacoustic signal in this material is amplified due to (i) rGO being a very efficient heat transfer layer, and (ii) the Au nanorods' ability to enhance the light absorbing properties of the rGO.

The use of Pt nanoparticles to combat restacking of G sheets was reported early on by Si and Samulski.²⁴² These authors showed that the capacitance of this Pt–G material can be increased 19 times as compared to stacked G sheets. In a similar manner, Au nanoparticles deposited on ErGO²⁴³ and Co₃O₄ nanoparticles deposited on G²⁴⁴ have been utilized as spacers to prevent G sheet restacking, thereby increasing the capacitance of the as-formed materials. Likewise, a report by Liu et al.²⁴⁵ has shown that ultrasmall Ni(OH)₂ nanoparticles can be used to prevent restacking in rGO sheets when forming a Ni(OH)₂–rGO material. Interestingly, in this report the authors showed that the Ni(OH)₂ nanoparticles can also be used as a recyclable sacrificial spacer, with the rGO material formed using an acid dissolution process of the Ni(OH)₂–rGO material maintaining the nonstacked structure.

4.7.2. Decoration of Graphene and Graphene Oxide with Nanostructures for Catalytic Applications. Besides the novel techniques mentioned in the previous section, traditional solution-based methods are being developed for G/nanoparticle systems, and exciting developments are being obtained when templates are used. For example, it has been shown by Tiwari et al.^{246,247} that ultrasmall Pt nanoclusters (~1 nm) and Pt nanodendrites can be deposited onto a GO scaffold using ssDNA as a template. In these synthetic methods, the authors showed that the Pt nanostructure formed was determined by the Pt salt used in the synthesis (see Figure 54). Remarkably, these systems prove to be excellent catalysts for the oxygen reduction reaction (ORR), with catalytic activities higher than the 2015 U.S. Department of Energy targets. Importantly, these catalysts also exhibited an impressive stability (~95% after 10 000 cycles) when compared to commercially available ORR catalysts (~40% after 10 000 cycles), thereby showing their applicability in commercial systems.

One well-known benefit of using graphene-based materials as a scaffold for nanoparticles in catalytic reactions is the enhanced stability that this affords the nanoparticles. For example, this phenomenon has been noted in the research conducted by Huang et al.²⁴⁸ who showed that Pd nanoparticles deposited on chemically rGO (CrGO) show enhanced stability in electrocatalytic activity toward the ORR in the presence of ethanol as compared to commercially available catalysts, that is, a current density of 0.055 versus 0.007 A mg^{−1}. This composite material was formed through a citrate catalyzed redox reaction initiated by irradiation using a 500 W mercury lamp, with the authors showing that this synthesis procedure can be extended toward Au–CrGO and Pt–CrGO composites. In another study, Yin and co-workers²⁴⁹ have shown that Au, Pd, and Pt nanoclusters can be deposited onto CrGO sheets without the use of surfactants by simple sonication of dilute AuCl₄^{3−}, PdCl₄^{2−}, and PtCl₆^{4−} solutions with CrGO dispersions. The Au/CrGO material was tested as an ORR catalyst, and while the performance of this catalyst was not comparable to commercial Pt/C ORR catalysts, it displayed an enhanced tolerance to methanol as well as a higher stability (16% versus 50% activity loss after 40 000 s).

The oxidation of CO over a rGO supported Pd nanoparticle catalyst has been demonstrated by Liu and co-workers.²⁵⁰ The catalyst was produced using an impregnation and hydrogen reduction method, with the authors showing that the Pd surface

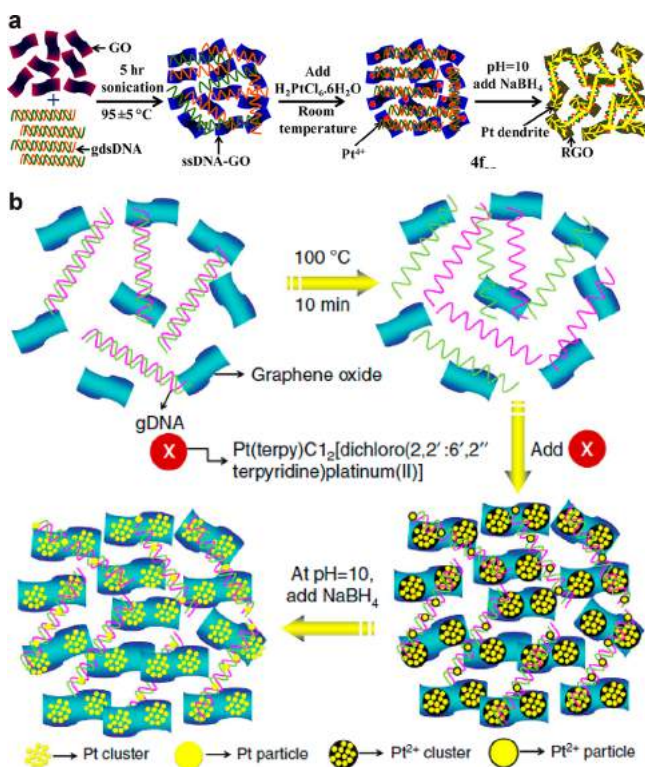


Figure 54. Synthesis of (a) Pt nanodendrites and (b) Pt nanoclusters deposited onto GO using DNA as a template. Panel (a) reprinted with permission from ref 246. Copyright 2013 American Chemical Society. Panel (b) reprinted with permission from ref 247. Copyright 2013 Nature Publishing Group.

is essential to the oxidation even though the catalyst presents with a layer of PdO_x. The as-produced catalysts were shown to be very stable for CO oxidation at temperatures of 120 °C with no observable decrease in catalytic activity even after 24 h time on stream; in contrast, at 100 °C a decrease in activity was noted, which was attributed to difficulty in dissociation of adsorbed O₂ on the Pd nanoparticles. Similar studies have shown that Pt-rGO²⁵¹ and Pt-Ni-rGO²⁵² can be used in the oxidation of CO, although these studies did not report long-term catalytic stability.

Most high activity ORR catalysts reported make use of precious transition metals; however, high cost of these metals limits their application, and as such the search for cheaper transition metals is highly desired. In this regard, Guo et al.²⁰⁹ have shown that Co/CoO (8 nm core/1 nm shell) nanoparticles deposited onto a TrGO substrate display an activity equivalent to commercially available Pt/C ORR catalysts in alkaline media. The catalytic activity is determined not only by favorable interactions between the TrGO and the nanoparticles, but also size tuning of the Co/CoO core/shell. Interestingly, the ideal core/shell dimension could be obtained by simple exposure of the as-formed Co nanoparticles to ambient conditions, thereby avoiding costly and time-consuming tuning steps. Last, while these catalysts did degrade with time, their stability was far improved as compared to the commercial Pt/C catalyst and Co/CoO nanoparticles deposited on Ketjen carbon.

The use of doped graphene materials has garnered wide interest due to the intrinsic ORR catalytic activity of N-, S-, and P-doped G.^{253–255} Doubt has been cast on this ORR activity being due to the G material, with Wang and colleagues^{256,257} showing that this activity is instead caused by trace metal impurities. Regardless, Zhou and co-workers²²⁶ have shown that

Ag nanoparticles can be deposited onto N-doped rGO using a simple solution method, and these materials outperform Ag nanoparticles deposited onto rGO as ORR catalysts. The authors of this study showed for the first time that there is a chemical interaction between the Ag nanoparticles and the N-doped CrGO. As this interaction is not present in the case of Ag/CrGO, Ag nanoparticles, and CrGO, the authors believe this Ag–N interaction is the origin of the ORR activity. This material is interesting as it is cheaper than traditional ORR catalysts and shows methanol tolerance, which is in contrast to commercially available Pt-based ORR catalysts that show negligible activity when methanol is introduced into the test system. In a related study, Jin et al.²¹³ have shown that Ag nanoclusters (~2 nm) can be electrochemically deposited onto a N-doped GO surface using ssDNA as a template. These Ag–GO catalysts were then applied as ORR catalysts, and while these systems do not exhibit activities that can rival the Pt–GO-based systems, the authors did show that these Ag-based ORR catalysts are tolerant toward methanol, showing no decrease in catalytic activity.

A recent report by Duan and colleagues²⁰⁷ has shown that not only is the doped graphene material important, but the catalytic activity can be further tuned by altering the nanoparticle shape. In this study, the authors utilized hydrothermal conditions with the addition of either 1-butanol, ethanol, or 1-pentanol in the presence of NH₄OH to deposit sphere, cubic, or ellipsoid Mn₃O₄ nanoparticles onto N-doped CrGO, respectively. The ellipsoid Mn₃O₄ nanoparticle N-doped CrGO material exhibited an onset potential of –0.13 V and a current density of 11.69 mA cm^{–2} at –0.6 V, as compared to the cubic material, which exhibited an onset potential of –0.16 V and a current density of 9.38 mA cm^{–2}. Additionally, as for the other N-doped G materials, the Mn₃O₄ containing catalyst displayed enhanced tolerance to methanol as compared to a commercial Pt/C ORR catalyst.

The application of G materials as catalysts in the important electrochemical hydrogen evolution reaction (EHER) has been reported by various groups.^{258–261} The use of Pt metal as the EHER catalyst is widely known; however, the cost of this metal requires innovative methods to either reduce its usage or replace it. In this vain, Bai and colleagues²⁶² have shown that Pd–Pt core–shell nanocube structures deposited onto rGO can be used as effective EHER catalysts. The authors showed that a 0.8 nm thin layer of Pt deposited onto a Pd nanocube resulted in the largest current density, and as such a large reduction in the Pt metal affords improved activity, which is desirable for industrial applications (see Figure 55).²⁶⁰ The increased reactivity of this core–shell nanocube design is attributed to the surface polarization that occurs due to differences in the work functions between the Pt and Pd, which then increases the EHER performance of the Pt surface.

In attempts to replace Pt as the catalyst, Youn et al.²⁶¹ showed that Mo₂C, Mo₂N, and MoS₂ nanoparticles can be deposited onto a CNT–GO support using a urea or thiourea-glass route. The as-obtained material was dried and calcined at 750 °C to afford Mo₂C, Mo₂N, or MoS₂/CNT–TrGO catalysts, which were applied toward the EHER, with the Mo₂C/CNT–TrGO catalysts affording the best activity of the three newly synthesized catalysts. It was further shown that the Mo₂C/CNT–TrGO materials' onset potential (62 mV) was far improved as compared to Mo₂C deposited on CNT (120 mV), TrGO (150 mV), and carbon black (135 mV). This improvement in activity is believed to be due to the excellent conductivity of the CNT–TrGO support, as well as the three-dimensional stacking structure of the support. Building on this work, He and Tao²⁶⁰ showed that MoC

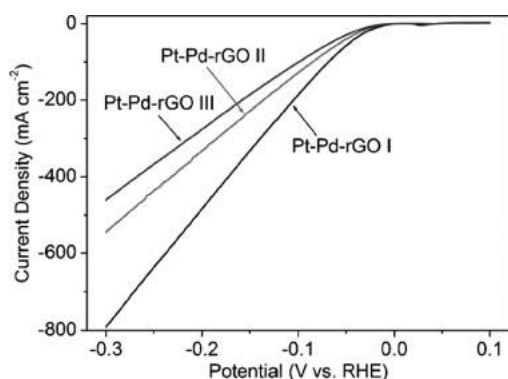


Figure 55. Polarization curves obtained for the Pt–Pd–rGO EHER catalysts, with different Pt thickness and equal Pd loading amounts. Pt–Pd–rGO I, Pt–Pd–rGO II, and Pt–Pd–rGO III show Pt layer thicknesses of 0.8, 1.8, and 3.2 nm, respectively. Reprinted with permission from ref 262. Copyright 2014 Wiley-VCH.

(~ 2.5 nm) and Mo_2C (~ 5.0 nm) nanoparticles can be deposited onto TrGO surfaces, and these catalysts were found to be highly stable with a negligible decrease in current density after 20 h of continuous EHER catalysis. Yan et al.²⁶³ have shown that a WN/rGO (3 nm WN nanoparticles) material can be phosphorylated post synthetically using NaH_2PO_2 as a phosphorus source in a furnace at 800 °C, and this resulting P–WN/rGO (4 nm WN nanoparticles) material can be used as an EHER catalyst. This phosphorylation step is beneficial, as it affords the catalyst enhanced stability upon recycling with only a 34 mV loss as compared to a 111 mV loss for the WN/rGO material after 5000 cycles. Additionally, a lower onset overpotential for the EHER is required for the P–WN/rGO material as compared to the WN/rGO material, that is, 46 versus 114 mV, respectively.

G-based materials have additionally been tested as methanol oxidation catalysts and hydrogen generation catalysts from formic acid, for application in fuel cells.^{264,265} Chen et al.²⁶⁴ have shown that highly dispersed AgPd nanoparticles can be deposited onto a rGO surface using a $\text{Co}_3(\text{BO}_3)_2$ coprecipitation and subsequent etching method. The authors showed that the coprecipitation and etching method prevents aggregation of the AgPd nanoparticles on the rGO surface. The resulting $(\text{Co}_6)\text{Ag}_{0.1}\text{Pd}_{0.9}/\text{rGO}$ catalyst exhibited an enhanced formic acid dehydrogenation activity as compared to the $\text{Ag}_{0.1}\text{Pd}_{0.9}/\text{rGO}$ catalyst prepared using a direct deposition method. Interestingly, this catalyst exhibited the highest turnover frequency, 2756 h^{-1} , reported for the formic acid dehydrogenation reaction at 323 K as compared to the previous 2623 h^{-1} reported for Pd/MSC-30. However, it should be noted that this trend is reversed at an operation temperature of 298 K, 453 versus 750 h^{-1} . Yang et al.²⁶⁵ have shown that preformed Pt nanoparticles can be deposited onto a sulfonated G (sG) support with a far greater density to give Pt/sG. The as-formed Pt/sG material was subsequently adhered to a glassy carbon electrode using poly(vinyl alcohol) and then applied as a methanol oxidation catalyst. The authors showed that the use of this sG support leads to an enhanced catalytic stability (9% activity loss) as compared to the use of an rGO support ($\sim 20\%$ activity loss). Additionally, the Pt/sG catalyst exhibited an enhanced catalytic activity as compared to Pt/C and Pt/rGO with mass activities after 200 cycles of 2156.54, 294.09, and 1162.03 mA mg^{-1} Pt, respectively. Utilizing a surfactant-less two-step solvothermal and microwave synthetic method, Chen et al.²⁶⁶ have shown that a Pd@Pt core–shell nanoflower supported on rGO can be

synthesized. Remarkably, the nanocrystals produced using this method exhibit an extremely high lattice matching ratio, and as such no grain boundary is observed and the material can be considered as a pseudo Pd–Pt alloy. The as-synthesized material was applied as a methanol oxidation catalyst and exhibited an impressive mass activity of 9.23 A mg^{-1} Pt with enhanced stability upon recycling as compared to other tested catalysts. The authors believe this enhanced activity is largely due to the surface-clean multimetallic nanocrystals produced in the surfactant free process.

The use of catalysts in organic reactions is very well-known, and as G has been shown to improve catalytic ability due to enhanced stability, there is an expanding field wherein G/nanoparticle systems are being applied in organic catalysis. For example, Moussa and colleagues²¹⁵ have shown that Suzuki–Miyaru, Heck, and Sonogashira cross-coupling can be achieved using Pd nanoparticles deposited on partially CrGO. In this study, the nanoparticles were deposited onto the GO surface, which was simultaneously reduced, through a redox reaction that was initiated by irradiation using a 532 nm laser source. It should be noted that, while these catalysts displayed extremely high activity, this activity dramatically decreased upon recycling with an average activity loss of $\sim 50\%$ after 4 cycles. This loss in activity can be attributed to an increase in average particle size due to agglomeration, which in turn leads to a reduced catalytic surface area. In a related study, Metin and colleagues²⁶⁷ have shown that Suzuki–Miyaru cross-coupling reactions can be catalyzed using a Ni/Pd core/shell nanoparticle system deposited on GO. These catalysts proved to be not only very stable and effective for the catalysis reactions probed, but they could easily be recycled with an efficiency of 98% conversion in the fifth reaction run. In another study, Putta and co-workers²⁶⁸ have shown that the Suzuki–Miyaura and Heck–Mizoroki C–C cross-coupling reactions can take place in water under atmospheric conditions, when Pd nanoparticle catalysts are attached to rGO using cyclodextrin. This result is remarkable as previous studies using G-based materials have required the use of Schlenk apparatus and/or elevated pressures for the coupling to proceed. Last, Heck reactions have been catalyzed using catalysts consisting of Pd nanoparticles deposited on G foams manufactured using a gas–liquid interfacial plasma technique.²⁶⁹ The use of G foam holds the benefit of an increased surface area as compared to Pd/rGO materials synthesized using the traditional solvothermal methods. Importantly, all of these C–C cross-coupling reactions utilizing G-based materials mentioned here do not require the use of phosphines, and as such are more environmentally benign.

The increased catalytic activity of G nanoparticle systems has been applied in sensors where an enhanced catalytic activity can lead to an improved limit of detection and/or sensitivity.²⁷⁰ Duy-Thach and Chung²¹⁰ have shown that Pd nanocubes deposited onto a GO support with subsequent reduction can be utilized as a fast, reproducible, and sensitive hydrogen sensor. The sensor exhibited negligible response to O_2 , NO_2 , CO , CO_2 , and N_2 , thereby showing a good selectivity for H_2 with a limit of detection of 6 ppm at a working temperature of 50 °C. This sensing mechanism is based on the well-known adsorption of H_2 molecules on Pd, where this hydrogen adsorption in turn leads to improved electron transfer between the nanoparticle and the G surface.²⁷¹ As more electrons flow from the nanocube, there is a change in the rGO charge carrier density, which improves the sensitivity for H_2 as the G material used in hydrogen detection is normally p-doped (see Figure S6). In another study, Li et al.²⁷² have shown that a highly dispersed PtPd nanoparticle rGO

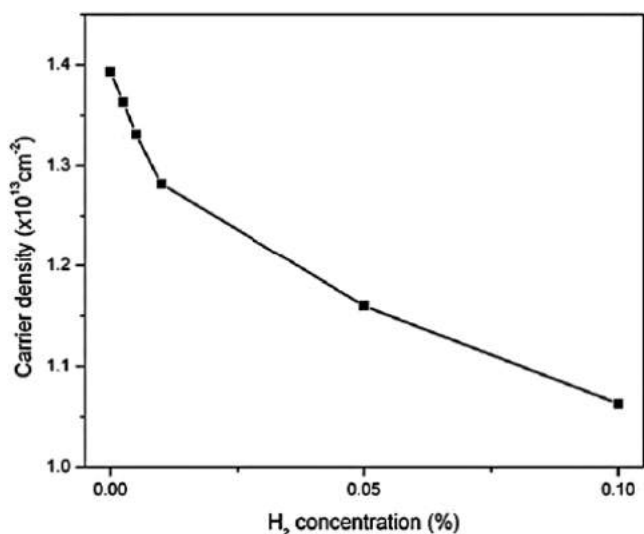


Figure 56. Charge carrier density in a graphene sensor versus hydrogen concentration. Reprinted with permission from ref 271. Copyright 2010 Elsevier B.V.

system synthesized using an ionic liquid functionalized GO can be used in the enzyme-less detection of glucose. The use of the ionic liquid functionalized GO is critical to the synthesis of the highly dispersed and small bimetallic nanoparticles, 3.4 nm for Pt(50)Pd(50)–IL(100)–rGO as compared to 6.3 nm for Pt(50)Pd(50)–rGO (see Figure S7).²⁷² At 0 V versus a Ag/

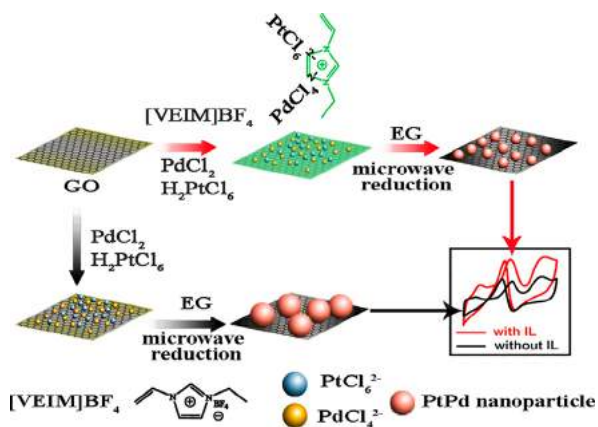


Figure 57. Synthesis of rGO/Pt–Pd supported catalysts. Reprinted with permission from ref 272. Copyright 2014 Elsevier B.V.

AgCl electrode, the Pt(50)Pd(50)–IL(100)–rGO material exhibited a limit of detection of 2 μ M for glucose, with negligible response toward the competing analytes ascorbic acid, uric acid, and dopamine.

The use of graphene materials in enhanced photoelectrochemical hydrogen evolution has been demonstrated by multiple groups.^{197,273,274} One method to improve the hydrogen evolution of p-type MoS₂ catalysts is to deposit the MoS₂ nanoparticles onto N-doped rGO, as Meng and colleagues²⁷⁵ have shown. The authors of this study showed that the MoS₂/N-doped rGO catalyst exhibited a 3-fold increase in activity as compared to the MoS₂/rGO catalyst. As the surface areas of the catalysts are comparable, the authors concluded that this increase in performance must be attributable to the N-doped G. Wang et al.²⁷⁶ have shown that the Au–P25–rGO complex can be

prepared using a simple one-pot microwave assisted hydrothermal synthesis. Interestingly, this material was then applied in visible light hydrogen production, with the Au nanoparticles shifting the visible light response of the TiO₂, which is normally only active in the UV region.²⁷⁷ In the Au–P25–rGO sample, the rGO leads to an impressive improvement in the quantum efficiency, that is, 4.1% as compared to 2.4% for the Au–P25 sample.

An interesting method to simultaneously deposit Pd nanoparticles and dope nitrogen into G has been developed by Vinayan and colleagues.²⁷⁸ In this synthesis procedure, the authors employed a simple solar exfoliation of a PdCl₂/GO–melamine composite material using an ordinary convex lens to obtain Pd/N-doped solar rGO. This produced material was then tested as a hydrogen storage material, governed by the hydrogen spillover mechanism, and exhibited a hydrogen storage capacity of 4.3 wt % at 25 °C and 4 MPa.

4.7.3. Decoration of Graphene and Graphene Oxide with Nanostructures for Application in Lithium-Ion Batteries. Recent reviews by Tuček et al.²⁷⁹ as well as others^{280,281} have highlighted the importance of G materials in LIBs. As such, this section should be considered as an update and highlight of these excellent reviews.

TiO₂ is a cheap and environmentally friendly material with a large cycling ability that can be applied as a cathode material in LIBs, and as such Li and co-workers²⁰⁸ have developed a sol–gel synthesis method to obtain highly dispersed and controllable 5 nm in size TiO₂ (anatase phase) nanoparticles deposited on rGO.²⁰⁸ This precise nanoparticle size control was obtained by adding tetrabutyl titanate to an ethanol dispersion of GO, which contained a small amount of ammonia as a reducing agent. The synthesized material was then applied in an LIB setup, as an anode, and exhibited a specific capacity of ~ 94 mA h g⁻¹ at 59 °C, which is in contrast to a mechanically mixed TiO₂/rGO material that exhibited a specific capacity of ~ 41 mA h g⁻¹. This improvement in performance as compared to the mechanically mixed sample was attributed to an increase in surface area, G conductivity, smaller nanoparticle size, as well as G layer thickness, which was ≤ 3 layers. In a similar way, ultrasmall ~ 5 nm MoO₂ nanoparticles have been deposited onto TrGO to improve the slow lithium insertion kinetics and volume expansion that MoO₂ anode materials usually suffer in LIBs.²⁸² In this study, the authors showed that not only decreasing the size of the MoO₂, but the presence of the G support, improves the reversible capacity of the MoO₂ material (765.3 mA h g⁻¹ for MoO₂/TrGO versus 533.9 mA h g⁻¹ for MoO₂). The one problem facing TiO₂ use in LIBs is its low capacity; for this reason, Pan et al. have shown that the capacity can be increased when the TiO₂ is coupled to a high capacity material such as Fe₃O₄ through codeposition of the nanoparticles onto exfoliated G sheets (EGS).²⁸³ This TiO₂–Fe₃O₄/EGS material was then applied as an anode in LIBs and delivered a reversible capacitance of 524 mA h g⁻¹ at 1000 mA g⁻¹, which is remarkably larger as compared to the value of 175 mA h g⁻¹ at 100 mA g⁻¹ reported by Li et al.²⁰⁸ This work showed that the introduction of a high capacitance material with TiO₂ is able to improve the overall capacitance while retaining a high cycling ability.

The use of Si in LIBs is of interest due to its high theoretical capacitance; however, this material expands rapidly on lithium ion adsorption, and as such its capacitance drops rapidly on cycling.²⁸⁴ To prevent this expansion, Zhu and colleagues²⁸⁵ have deposited 30 nm Si nanoparticles onto rGO using a magnesiothermic reduction reaction of a SiO₂/GO composite at

700 °C. The ratio of magnesium to SiO₂/GO composite material is critical to obtaining the desired product, with a 1:1 ratio providing the 30 nm Si nanoparticle/rGO material. This material was then applied as an anode in LIBs and showed a minimal decrease in capacitance of 1300 mA h g⁻¹ at 100 mA g⁻¹ after cycling at various current densities (see Figure 58).²⁸⁵ Another

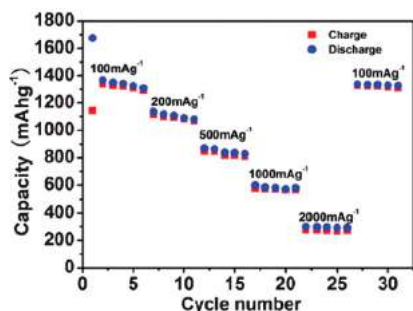


Figure 58. Capacity of the Si/rGO material at various current densities upon cycling. Reprinted with permission from ref 285. Copyright 2013 Royal Society of Chemistry.

method employed to improve the cycling capacity of Si has been demonstrated by Hassan and colleagues²⁸⁶ who showed that Si nanowires can be deposited onto a Ni nanoparticle–TrGO support using a novel high temperature thermal shock and deposition method. Importantly, the material was coated with a 2 nm layer of amorphous carbon. When this material was then applied as an anode in LIBs, the material exhibited an improved cycling stability (550 mA h g⁻¹ at 6.8 A g⁻¹ for the 100th cycle), which is attributed to the synergy between the Si nanowires and the Ni–TrGO support. It is interesting to note that in this study the general morphology of the >100 nm long Si nanowires was retained, although significant fragmentation and swelling occurred, with this shape retention being attributed to the amorphous carbon layer coating the surface. To improve the stability of Si nanoparticles on electrochemically exfoliated G, a polyaniline emeraldine base layer has been used as described by Wei et al.²³¹ This material exhibited a reversible capacity of 1710 mA h g⁻¹ at 0.42 A g⁻¹, and a capacity retention of 86% after 100 cycles. In a study by Zhou et al.,²⁸⁷ it has been shown that G sheets can be bridged and orientated using Si nanoparticles, which act as hinges between the sheets. In this synthesis, the Si nanoparticles coated with bovine serum albumin and GO are dispersed together, and then electrostatic self-assembly takes place during a vacuum filtration process. The benefit of using this material is that it can be applied directly as a self-supporting anode in LIBs with an excellent stability and impressive gravimetric capacity of 1390 mA h g⁻¹ at 2 A g⁻¹.

Similar to Si, Ge holds promise as an anode material in LIBs due to its large theoretical capacity, although it suffers cycling drawbacks due to expansion upon Li insertion. A study by Yuan and Tuan²⁸⁸ has shown that a carbon-coated Ge nanoparticles/rGO material can be applied as an anode material in LIBs with large capacitance retention close to the Ge theoretical capacitance value. The C/Ge/rGO material exhibited a discharge capacity of ~1100 mA h g⁻¹ at 0.2 C after 360 cycles with discharge rates ranging from 0.2 to 20 C. This material was additionally used to construct aluminum-pouch-type lithium-ion commercial type batteries, which offered a capacity of over 20 mA h; these batteries were then used to power an electric fan, a scrolling LED marquee, and LED arrays.

As the Si and Ge examples have demonstrated, the use of a carbon layer promotes recycling stability, and as such it would be expected that G can also act as a coating layer to improve recycling stability of materials in LIBs. In this vein, Shi and co-workers²³⁸ have shown that hollow Li₃VO₄ microboxes coated with rGO can be applied as an anode material in LIBs. This material exhibits improved capacitance at larger discharge rates (223 versus 87 mA h g⁻¹ at 20 C), as well as recycling stability (378 versus 345 mA h g⁻¹ after 50 cycles at a current density of 20 mA g⁻¹), as compared to uncoated Li₃VO₄ microboxes. In another study, Hu and colleagues²³⁹ applied a Kirkendall process to fabricate a γ -Fe₂O₃/G/amorphous carbon (hollow core–first shell–second shell) material by air oxidation of a Fe core/G/amorphous carbon material. The authors showed that the hollow core and G layer shell are important factors in the stability of the material upon recycling (833 mA h g⁻¹ at 1 C after 100 cycles) when compared to uncoated α -Fe₂O₃ nanoparticles as well as other reported α -Fe₂O₃/G and α -Fe₂O₃/carbon materials.^{289,290}

An alternative to LIBs are the sodium ion batteries (NIBs), which have a lower cost. However, these batteries are plagued with stability and performance issues, which are related to the limited choices of anode materials.²⁹¹ For this reason, Yu and colleagues²⁹² have proposed the use of Sb₂S₃ nanoparticles coating rGO as an anode material due to its large theoretical capacity of 946 mA h g⁻¹ as well as stability upon recycling. As compared to commercially available Sb₂S₃, the Sb₂S₃/rGO material shows negligible capacitance loss upon cycling, that is, 97.2% capacitance retention versus 50% after 50 cycles. From these results, we can see the critical role G can play in the future of NIBs, which can operate with large charge densities at a lower price.

G/nanoparticle materials have also been applied in lithium–sulfur batteries, where Xiao and colleagues²⁹³ have shown that the deposition of a TiO₂/G layer on top of the porous CNT/S cathode leads to improved stability. While the TiO₂/G layer does not contribute to the charge capacity, it does inhibit the dissolution of the S cathode, which results in very low capacity degradation rates upon cycling. For this reason, the battery made with the TiO₂/G is able to supply a specific capacity of 1040 mA h g⁻¹ over 300 cycles at 0.5 C, while the S cathode coated only with G supplied 750 mA h g⁻¹ and the uncoated S cathode supplied 430 mA h g⁻¹.

Lithium–oxygen and lithium–sulfur batteries have been proposed as alternatives to LIBs due to their large specific energy density; however, they suffer due to capacitance decrease on recycling. To improve the capacity fading that occurs in these proposed batteries, due to irreversible reactions, Ryu et al.²⁹⁴ have developed a Co₃O₄ nanofiber/G material, which they applied as the O₂ cathode in a Li–O₂ battery. The Co₃O₄ nanofibers were produced by an electrospinning process and then deposited onto pristine G (noncovalently functionalized using 1-pyrenebutyric acid) or rGO using sonication. The pristine G material proved to be important for cycling stability of the material with a discharge capacity of 10 500 mA h g⁻¹ after 80 cycles (see Figure 59).²⁹⁴ This report shows that the use of G materials still holds much promise for batteries, with applicability in next generation energy devices.

4.7.4. Decoration of Graphene and Graphene Oxide with Magnetic Nanostructures. A recent review by us has highlighted the importance of magnetic G materials in wastewater treatments, medical research, catalysis, etc., and as such this section should be considered as an update to this literature.²⁷⁹

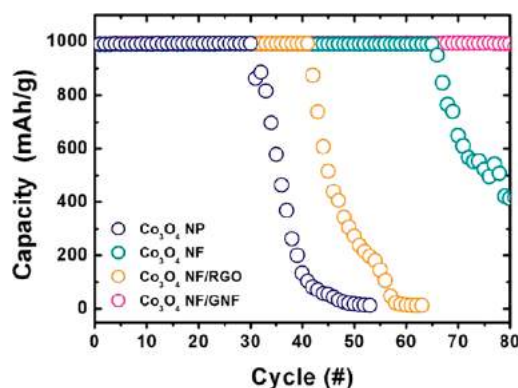


Figure 59. Cycling performance of Co_3O_4 NPs (nanoparticles), Co_3O_4 NFs (nanofibers), Co_3O_4 NF/rGO composite, and Co_3O_4 NFs/GNF (graphene) materials under a specific capacity limit of 1000 mA h g^{-1} in a voltage window between 4.35 and 2.0 V at a current density of 200 mA g^{-1} . Reprinted with permission from ref 294. Copyright 2013 American Chemical Society.

In an early study by Chandra et al.,²⁹⁵ superparamagnetic Fe_3O_4 -rGO hybrids were synthesized via the hydrazine reduction of a Fe_3O_4 -GO precursor. These hybrid materials were subsequently applied in the removal of As(III) and As(V) from contaminated water samples. As the material showed near complete (99.9%) arsenic removal and magnetic separation, these types of material should be applicable in water purification.

The simple autoclave pyrolytic fabrication of Fe_3C (iron carbide) nanoparticles encapsulated by G has been reported by Hu et al.²⁹⁶ An advantage of using G encapsulated nanoparticles is that they are separated from environments, which may decompose them. This was demonstrated for the Fe_3C nanoparticles, which exhibited stability in acid solution that

normally degrades it. This G Fe_3C encapsulated material was subsequently applied as an ORR catalyst in basic media, with an onset potential (1.05 V versus RHE) and half wave potential (0.83 V) comparable to those of a commercially available Pt/C ORR catalyst. Importantly, this material shows negligible response to methanol introduction into the system as compared to the commercial Pt/C catalyst. In another study, Moussa et al.²⁹⁷ have shown that the Fe-based nanoparticles (Fe_{15} -rGO, Fe_{15}K_5 -rGO, $\text{Fe}_{15}\text{Mn}_5$ -rGO, and $\text{Fe}_{15}\text{K}_5\text{Mn}_5$ -rGO) deposited onto a rGO can be used in the highly stable and recyclable Fischer-Tropsch synthesis of liquid hydrocarbons from C_2H_4 gas. The advantage of using the G-based systems is that most of the systems tested tend to give minor formation of CH_4 and CO_2 with a large activity toward higher hydrocarbons C_8^+ . Of the G-based catalysts tested, the Fe_{15} -rGO exhibited the lowest CH_4 production (1.5%), yet exhibited a large C_2 - C_7 hydrocarbon ratio of 32.0%; in contrast, the Fe_{15}K_5 -rGO sample exhibited a 2.6% formation of CH_4 and the largest formation of C_8^+ hydrocarbons (86.7%). These G-based materials exhibited an improved performance as compared to similar CNT-based materials, and the authors believe this is due to the accessibility of the iron carbide Fe_5C_2 active phase on the G support during catalysis.

An interesting study by Xu and co-workers²⁹⁸ has shown that a 3D conductive Fe_3O_4 /rGO aerogel can be fabricated through an rGO self-assembly and simultaneous Fe_3O_4 nanoparticle deposition. Interestingly, the as-synthesized lightweight material could be manipulated using an external magnetic field, while still maintaining its inherent conductivity (see Figure 60).²⁹⁸ As the material maintains its conductivity upon magnetic deformation, the degree of strain along the axial and radial directions can then be determined by measuring the change in conductivity. For these reasons, the authors believe that this material holds

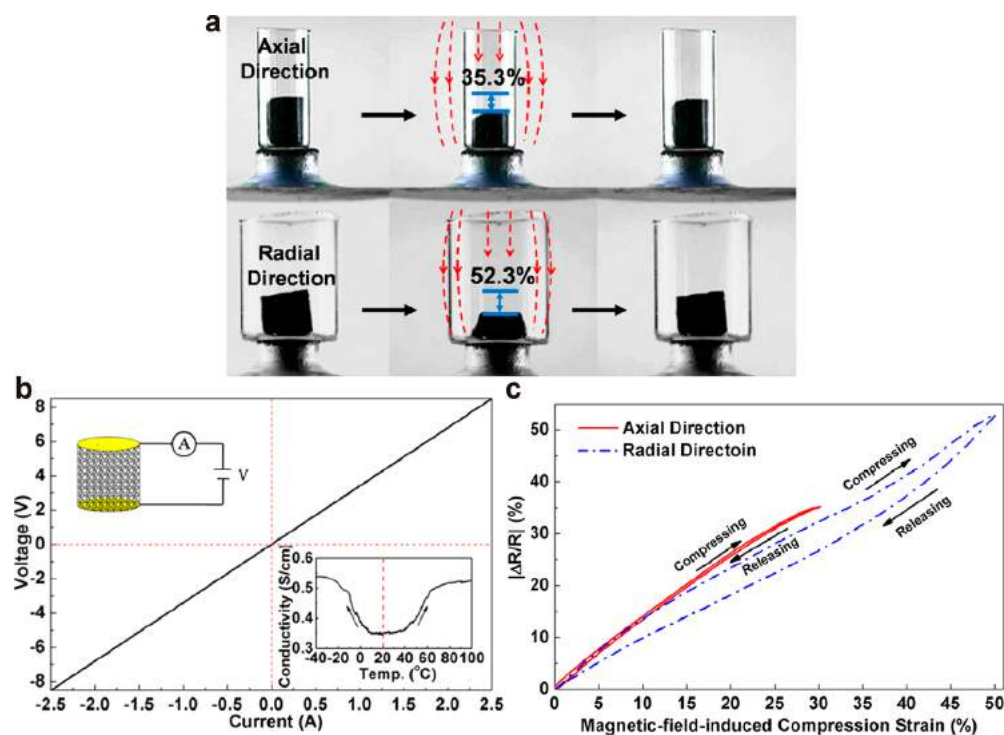


Figure 60. (a) Magnetic deformation of the magnetic Fe_3O_4 /rGO aerogel, (b) I - V curve and thermal conductivity stability of the aerogel, and (c) change in the electrical resistance of the aerogel as a function of the magnetic field-induced deformation. Reprinted with permission from ref 298. Copyright 2015 American Chemical Society.

promise in self-sensing soft actuators, microsensors, micro-switches, as well as oil absorption and recycling.

Fe₃O₄/rGO composite materials as electromagnetic shielding/interference materials have been reported by multiple research groups.^{299–301} The materials can be produced by either solution precipitation of Fe₃O₄ nanoparticles onto the rGO surface,²⁹⁹ or the deposition of already formed Fe₃O₄ nanoparticles onto the rGO surface.³⁰⁰ The mechanism of this interference is attributed to the radiation being reflected by the small G sheets compartments (which are kept separated by the Fe₃O₄ nanoparticles), and subsequently this radiation is then able to interact with the Fe₃O₄ nanoparticles, which dampens the radiation. As such, a composite material consisting of polystyrene/TrGO/Fe₃O₄ is able to shield electromagnetic radiation with an efficiency of more than 30 dB in the 9.8–12 GHz frequency range.²⁹⁹ In contrast, when the polymer support was changed to polyvinyl chloride (PVC), an efficiency of only 13 dB in the 8–12 GHz range was observed.³⁰⁰ It should be noted however that in the PVC example, the TrGO/Fe₃O₄ additive greatly decreased the flammability of the PVC as well as afforded the PVC more tensile strength (20.8% increase) and larger Young's modulus (73.7% increase).

Kumar et al.³⁰² have shown that glass beads coated with a Fe₃O₄/rGO material can be used as simple multifunctional micro robots (microbot). The authors showed that by varying the external magnetic field between 40 and 110 mT, the average velocity of the microbot can be varied linearly from 1.8×10^{-4} to 1×10^{-3} m s⁻¹. Interestingly, as these microbots' velocity can also be varied using chemical reactions and electric fields, the authors believe that the velocity can be increased or decreased even further. Demonstrating the practical applications of this microbot, the authors showed how it can be used to deliver cargo (~1000 times heavier and ~13 times larger in size than the microbot) inside a confined environment using a magnetically directed "drop-off" and "pick-up" mechanism.

Jiang et al. have shown that a Fe₂O₃-rGO composite can be produced using a supercritical CO₂ thermal reduction of a Fe(NO₃)₃·9H₂O and GO dispersion.³⁰³ The authors then showed that a vertically or horizontally aligned Fe₂O₃-rGO paper can be obtained by filtration of a composite dispersion under a controlled magnetic field. The as-formed papers were then applied in H₂S gas sensing, with the vertically aligned paper showing more sensitivity than the horizontally aligned material. This report demonstrates that the structural orientation of the graphene sheets in any synthesized material plays a crucial role in maximizing efficiency.

4.7.5. Decoration of Graphene Nanostructures with Quantum Dots. The deposition of various quantum dots (QDs) onto G proceeds (in most cases) via a facile solvothermal process, and the application of these QD-G materials varying from photocatalysis, supercapacitance, LIBs and NIBs, photodetectors, photosensitizers, water purification, etc., has been demonstrated by multiple research groups.^{304–311} It should be noted here that similar applications are being realized for materials containing GQDs (graphene quantum dots).^{312–317} Other methods toward QD-G materials have been developed by Zhang and colleagues³¹⁶ who fabricated a UV photodetector by the atomic layer deposition of ZnO QDs onto G. The authors note that the ZnO nucleates at defect sites in the G, which leads to the formation of QDs instead of thin film layers as is normally found with atomic layer deposition methods.

Perhaps one of the more novel methods that could be employed to deposit QDs onto a G surface was hinted at in a

study by Zeng and colleagues³⁰⁸ who showed that the carcinoembryonic antigen could be detected using a novel CdS QD-GO photoelectrochemical biosensor. The mechanism of detection relies on the horseradish peroxidase, which catalyzes the reduction of sodium thiosulfate with H₂O₂ to give H₂S, and this reacts with Cd²⁺ present in solution to form CdS QDs. As such, this study shows that enzymes could potentially be used in the deposition of QDs with a controllable size on a G substrate.

QD-G materials have been widely applied in the photoelectrochemical and dye-sensitized solar cell fields, with this largely being due to the transparency and conductivity of G materials, which make it a viable replacement for traditionally applied electrode materials.^{304,305,318} In these studies, the G component of the solar cell is crucial in the separation of charge carriers and as such preventing recombination, which leads to an improved efficiency. Jung and Chu³¹⁹ have shown that the binding mechanism between the quantum dot and graphene is critical toward improved charge transfer efficiency between the components. In this study, the authors deposited capped CdSe QDs onto an rGO substrate using either covalent (aryl bond) or noncovalent (π - π interactions) attachment. Thin films of these materials were fabricated electrophoretically, and it was shown that the covalently attached CdSe QDs lead to an improved quantum efficiency as well as photocurrent density. It should be noted, however, that noncovalent attachment is beneficial toward an enhanced phototransfer processes between the CdSe QD and the G surface, as has been demonstrated by Guo and colleagues.³²⁰ Interestingly, Hirose and co-workers³²¹ have shown that QD blinking can be suppressed in a CdTe QD-G system by spin coating a layer of polyvinylpyrrolidone or polyethylene glycol over the composite material. Photoluminescence blinking can lead to a decrease in efficiency, as it is essentially the random switching between ON and OFF states; as such this spin coating method holds promise toward the development of improved solar cell systems incorporating QD-G systems. Liu and colleagues³²² have demonstrated using fluorescence emission analysis that multiphoton emission in CdTe/ZnS QDs can be greatly enhanced when the QDs are deposited onto single layer CVD G. This enhanced multiphoton emission is believed to be due to a decrease in fluorescence lifetime, and hence fluorescence intensity, which results in a lower single-photon emission probability due to the presence of the G, which acts as a quencher.

The use of QD/G materials in energy materials that do not take advantage of the photocatalytic properties of the QDs has also generated interest. TiO₂-QD-rGO, Ge-QD-N-doped rGO, Co₃O₄-QD-rGO, and ZnO-QD-rGO are among the many materials that have been employed in LIBs.^{310,323–325} One of the major reasons to employ QDs in LIBs is that with a decrease in nanoparticle size, the volume expansion associated with lithium insertion and extraction is minimized, and as such the batteries are more stable than counterparts consisting of larger particles. In the synthesis of the Co₃O₄-QD-rGO material, Zhou et al.³²⁵ showed that a microwave synthetic method can dramatically decrease the reaction time normally required for solvothermal synthetic methods.

Carbon-coated Fe₃O₄ QDs deposited on rGO have the additional structural stabilization benefit, besides size reduction, of avoiding detachment of the Fe₃O₄ QDs through an enhanced strong adhesive force between QD and G.³²⁶ As such, a synthesized Fe₃O₄@C-rGO material exhibited a specific capacity of 940 mA h g⁻¹ at a current density of 150 mA g⁻¹, which is similar to results obtained for Fe₃O₄-G coated

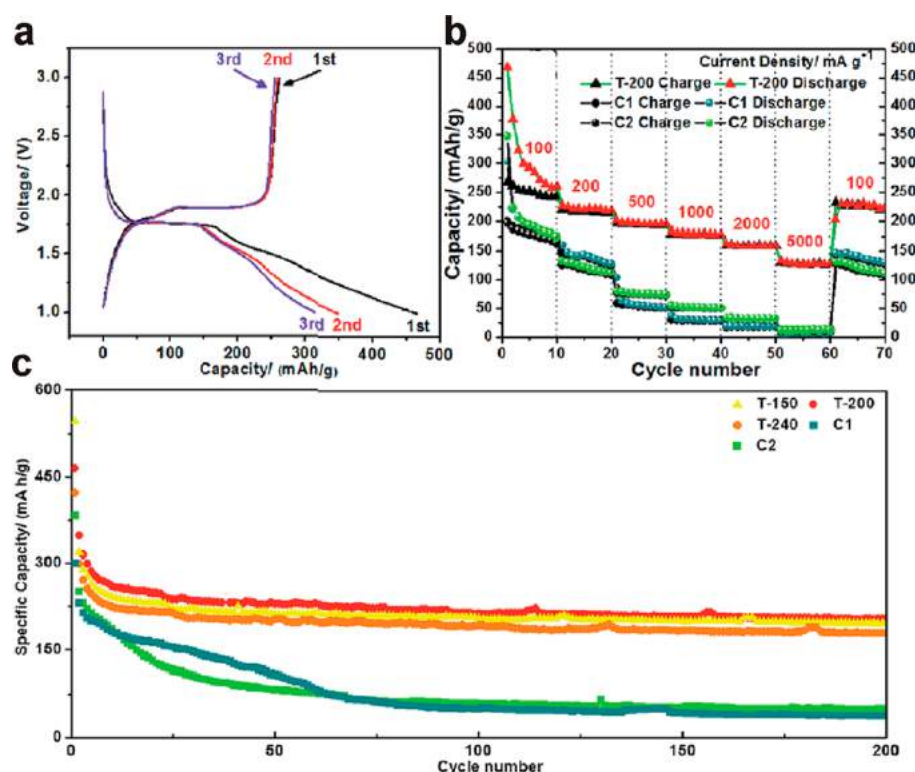


Figure 61. (a) Charge–discharge voltage profiles of the T-200 hybrid cycled at 1.0–3.0 V at a current density of 0.1 A g⁻¹, (b) rate performances of T-200, C1, and C2 at various current densities, and (c) cycling performance of T-150, T-200, T-240, C1, and C2 at a current density of 0.1 A g⁻¹. Reprinted with permission from ref 339. Copyright 2015 Royal Society of Chemistry.

nanoparticles cross-linked into 3D G foams.³²⁷ Xia and colleagues³¹⁰ have shown that an Fe₂O₃–QD–rGO material can be applied as an anode material in an asymmetric supercapacitor, with the cathode material being fabricated from a MnO₂ nanoparticle/rGO material. The Fe₂O₃–QD–rGO anode material exhibited a maximum specific capacitance of 347 F g⁻¹ when cycled between -1 and 0 V versus an Ag/AgCl reference electrode in a 1 M Na₂SO₄ aqueous solution. Additionally, the authors showed that the fabricated asymmetric supercapacitor can deliver an energy density of 50.7 Wh kg⁻¹ at a power density of 100 W kg⁻¹, with this supercapacitor exhibiting 95% retention of its initial capacitance after 5000 cycles.

A novel method for the deposition of PbS QDs onto GO has been presented by Tayyebi and co-workers³²⁸ who used supercritical ethanol, which acted as a solvent, reducing agent, and surfactant in the reaction. Interestingly, the authors showed that the PbS QDs bind to the G surface through residual oxygen functionalities on the TrGO surface through Pb–O–C bonds; this in turn results in a reduced band gap, which one would expect to translate into an increased recombination rate. This counterintuitive phenomenon is believed to be due to the electron transfer from the conduction band of the PbS QDs into the TrGO, thereby leading to a decrease in charge recombination.

TiO₂ QDs deposited onto exfoliated G have been shown to be an effective precursor toward the formation of ultrathin TiO₂ films deposited onto glass substrates.³²⁹ These G-containing TiO₂ QD materials exhibit improved photocatalytic efficiency when compared to G-containing TiO₂ nanoparticle materials, as well as G free TiO₂ QD. This is attributed to the larger contact area that occurs between the QD and the G surface as compared to the nanoparticle and G surface. In another study by Cao and

colleagues,³³⁰ it has been demonstrated that MnO_x QDs can be deposited onto a rGO substrate uniformly coated with TiO₂ nanoparticles using a UV and microwave synthesis method. The material synthesized in this method displays an enhanced dye degradation photocatalytic activity, as well as electrochemical and photochemical energy storage. Interestingly, this material can photochemically store energy, which can be utilized in antimicrobial activity in the dark with efficiency similar to penicillin, although UV irradiation leads to a far greater inhibition effect.

5. APPLICATIONS OF NONCOVALENTLY FUNCTIONALIZED GRAPHENE AND GRAPHENE OXIDE

Noncovalent functionalization through electrostatic, π -effects, van der Waals forces, and hydrophobic effects, etc., is an effective method for changing the physicochemical properties of nanofillers to improve their interfacial interactions in a material matrix.³³¹ Noncovalent functionalized nanomaterials containing G/GO exist in two forms: (i) nanospecies deposited onto the G surface and (ii) nanospecies encapsulated with G/GO. These materials have been applied in various advanced applications in the fields of energy materials, green chemistry, environmental science, nanodevices, catalysis, photocatalytic, biosensors, bioimaging, and biomedicine. In these subsections, we will give an overview of selected recent advanced applications wherein variously functionalized G/GO nanomaterials have been applied.

5.1. Energy Materials

Monolayer or few-layer G/GO structures are extremely efficient materials for adsorption of or encapsulation of nanoparticles. In fact, these nanoparticles exhibit a beneficial impact on G or GO-

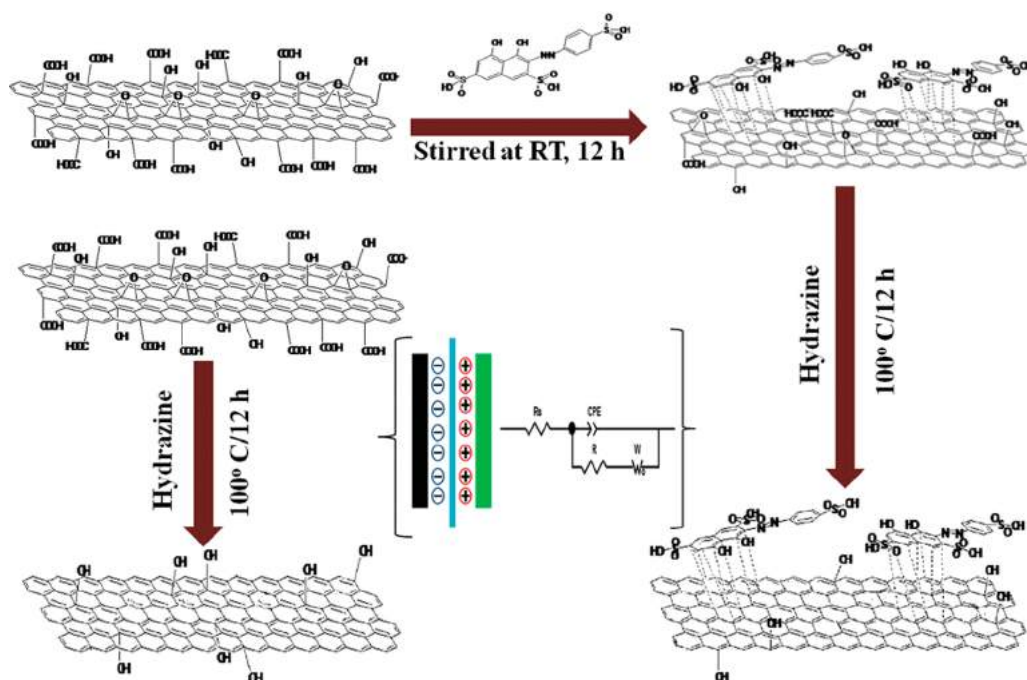


Figure 62. Synthetic methods used to produce SAC-rGO (right bottom) and rGO (left bottom). A schematic of the electrochemical device used to measure the supercapacitance of the material is also shown. Reprinted with permission from ref 345. Copyright 2015 Royal Society of Chemistry.

based electrochemical energy conversion and storage devices.^{332–336} Campbell et al.³³⁷ have evaluated the battery/supercapacitor performance of large surface area G modified with anthraquinone (AQ), where the AQ and G are bonded through π - π interactions. They reported that the gravimetric energy storage capacity of G macro-assemblies (GMAs) can be increased nearly 3 times ($\sim 23 \text{ Wh kg}^{-1}$) by AQ. They also demonstrated that the AQ provides a battery-like redox charge storage capacity (927 C g^{-1}), while the inherent conductivity and capacitance of the GMAs are maintained. Kong et al.³³⁸ have developed a MoS_2 @G nanocable web composite, which was applied as an advanced high performance electrode materials for LIBs. The binder-free MoS_2 @G hybrid electrode not only showed a large specific capacity ($\sim 1150 \text{ mA h g}^{-1}$) and remarkable recycling performance ($\sim 100\%$ stability after 160 cycles at 0.5 A g^{-1}), but also exhibited a high-rate capability of 700 mA h g^{-1} at the sweep rate of 10 A g^{-1} . It is believed that the improvement in the performance of the hybrid is due to the highly dispersed MoS_2 sheets, which accelerate the Li-ion transport, and shorten the Li^+ ion diffusion paths. The authors believe that this 2D/2D hybrid nanoarchitecture leads to more active sites for Li^+ insertion/extraction and as such could be applied as an electrode material in high performance batteries. TiO_2 materials are desired as anode materials in LIBs due to safety factors, low price, environmental benignity, and excellent cycle durability. Conversely, TiO_2 materials have a poor theoretical capacity and conductivity. To combat this, Yang et al.³³⁹ employed a sandwich-like porous TiO_2 /rGO hybrid (T-150, T-200, and T-240) as an anode electrode material for LIBs. These hybrid materials with porous structures and high electrical conductivity exhibited good stability (no decrease in capacity of 206 mA h g^{-1} at a current density of 0.1 A g^{-1} after 200 charge-discharge cycles) and a remarkably large reversible capacity of $\sim 128 \text{ mA h g}^{-1}$ at a current rate of 5 A g^{-1} (see Figure 61).³³⁹ The efficiency of these hybrids is attributed to (i) the porous TiO_2 nanocrystals whose small sizes reduced the diffusion length

for Li insertion-extraction, as well as (ii) affording good contact with the electrolyte and the RGO sheets, which enhanced the conductivity of the hybrid.

Ali et al.³⁴⁰ have developed an iron fluoride hydrate/rGO material as a promising cathode material for NIBs. These materials displayed an impressive discharge capacity of 266 mA h g^{-1} under a current density of 0.05 C , and a stable cycle performance ($\sim 86\%$ retain after 100 cycles). These properties suggest its applicability as a cathode material for NIBs. It should be noted that due to polarization effects and the large size of the Na^+ ion, the rate capability of this iron fluoride hydrate/rGO material was lackluster. As such, further developments in the preparation methods of G or GO nanostructures and nanomaterials are required for G materials to be applicable in NIBs. MoS_2 /rGO flake hybrids have been recently identified as a promising material for electrodes in NIBs.³⁴¹ The hybrids were synthesized in the form of layered free-standing papers, which were found to show a good cycling ability with stable charge capacity of 230 mA h g^{-1} . Moreover, these composite papers possessed a high average strain, thus considering them as ideal candidates for exploitation in the field of large-area free-standing binder-free flexible electrodes for rechargeable applications. Qu and co-workers³⁴² have shown that rGO can be assembled into 3D porous networks using a dual substrate-assisted reduction and assembly (DSARA) method, which the authors believe can be applied in energy-related applications such as LIBs, fuel cells, photoelectric conversion devices, etc. In this study, the authors showed that a 3D DSARA-produced rGO porous network coated with NiO/Ni complexes exhibits a remarkable capacity (1524 mA h g^{-1}) with a stable high charge-discharge rate (600 mA h g^{-1} after 1000 cycles). Additionally, a PdPt alloy deposited onto the 3D DSARA-produced rGO porous network displayed efficient catalytic performance for the ORR in fuel cells.³⁴² The formation of these 3D G structures can increase the specific capacity of a material through the introduction of porous channels, which facilitate ion transportation, and as such

optimized 3D G nanostructures are critically important not only in ORR, but supercapacitor applications.³⁴³ In this sense, Jung et al.³⁴⁴ have reported that controlled porous aerogel structures can be formed from suspensions of electrochemically exfoliated G, and that this material can be applied as a supercapacitor electrode. Because of the 3D G aerogels' large specific surface area, low density, and superior electrical conductivity, it showed a large specific capacitance (325 F g^{-1} at 1 A g^{-1}) and good energy density (45 Wh kg^{-1} in acid electrolyte) with high electrochemical durability. Jana and co-workers³⁴⁵ have shown that GO can be noncovalently modified using sulfanilic acid azocromotrop (SAC), which is then reduced in a subsequent step using hydrazine monohydrate to give SAC-rGO (see Figure 62). This synthesized material was then applied as a supercapacitor electrode material, which showed a large capacitance (366 F g^{-1} at 1.2 A g^{-1}), high energy density (25.86 Wh kg^{-1}), and excellent power density (980 W kg^{-1}) with good cycling stability ($\sim 72\%$ retain after 5000 charge–discharge cycles). These impressive electrochemical properties are attributed to the redox reactions between the SAC-rGO materials' $\text{SO}_3\text{H}/\text{OH}$ functionalities and the H^+ ions of H_2SO_4 .³⁴⁵

5.2. Solar Cells

Solar energy is considered a possible alternative to the traditional fossil fuel energy sources due to the fact that the sun is essentially a free and continuous energy supply. Additionally, the cost of solar cells can be dramatically reduced when the efficiency of solar cells is increased; for example, a solar module that exhibited a 1% enhancement in its efficiency led to a 5% reduction in price.³⁴⁶ G/GO exhibits potential as an optically conductive window as they allow a wide range of light wavelengths to pass through, that is, optical transmittance reaching $\sim 98\%$.^{346,347} Additionally, G/GO optical and electrical properties can be modulated through noncovalent interactions with metal complexes, which make it suitable for different types of solar cell applications.^{346–350} Wang et al.'s³⁵¹ group have developed a solution-based low-temperature deposition procedure to manufacture the electron collection layer using a G/TiO₂ nanoparticle material as the electron collection layers in meso-structured perovskite solar cells. They found that the solar cells manufactured using this low-temperature process exhibit a significant photovoltaic performance, that is, power conversion efficiency up to 15.6%, which suggests that solar cells no longer need a high-temperature sintering process when TiO₂ is employed in the electron collection layer (see Figure 63). This enhancement in efficiency was ascribed to the synergistic effects between G and TiO₂ nanoparticles, where (i) G might reduce the formation of energy barriers at the interface between TiO₂ and fluorine doped tin oxide (FTO) and (ii) the superior charge mobility of G may provide improved electrical conductivity in the electron collection layer.³⁵¹ Kim and colleagues³⁵² have studied the optoelectronic properties of G thin films (thickness between 2–30 nm) prepared using a Langmuir–Blodgett (LB) assembly method. In this method, the G thin films are assembled by dip coating a glass substrate in a *N*-methyl-2-pyrrolidone (NMP) and water G dispersion. The authors found that the conductivity of the as-formed films can be tuned by increasing the lateral size and the density of the packing of the G platelets in the LB assembly. Fukuzumi et al.³⁵³ reported a rapid photoinduced charge separation in ordered self-assembled layers of perylene-diimide and GO (PDI–GO), where this self-assembly is believed to proceed via π – π and electrostatic interactions between the components in water. The authors believe that the π – π stacking

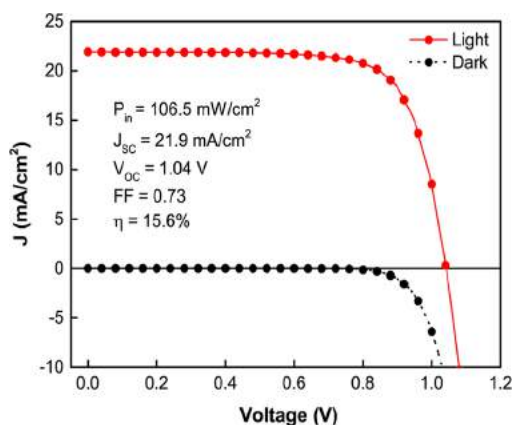


Figure 63. G–TiO₂ hybrid-based solar cell performance under simulated AM 1.5, 106.5 mW/cm² solar irradiation (red line), and that in the dark (black line). Reprinted with permission from ref 351. Copyright 2014 American Chemical Society.

between the components is necessary for efficient charge separation as it promotes a “pull effect”. This in turn leads to slow charge recombination due to holes being able to move easily on the G surface. In contrast, when this hybrid stack material is introduced into a polymer environment, the interlayer charge-hopping mechanism is interrupted due to loss of the self-assembly macrostructure, and this causes rapid back electron transfer from PDI^{•−} to oxidized GO, that is, faster recombination.³⁵³ In another study, Dehsari and co-workers³⁵⁴ developed a polymer solar cell (PSC) hole transport layer (HTL) by spin coating a thin layer of ultra large GO/poly(3,4-ethylenedioxythiophene):poly(styrenesulfonate) (PEDOT:PSS/GO) material onto an indium–tin–oxide (ITO) anode. They showed that the optimized PSC with a PEDOT:PSS/GO HTL layer exhibits a power conversion efficiency of 3.39%, an enhancement of $\sim 12\%$, with respect to a PSC, which contains only a PEDOT:PSS layer. The improved power conversion efficiency is attributed to improved hole mobility and reduced radiative exciton quenching at the interface of the PEDOT:PSS/GO HTLs and the poly(2-methoxy-5-(2-ethyl)hexoxy-phenylenevinylene) active layer.³⁵⁴ Kymakis and co-workers³⁵⁵ fabricated flexible organic photovoltaic devices (OPD) with in situ nonthermal photoreduction of spin-deposited GO electrodes. The GO films were reduced by the laser system and then were utilized as transparent electrodes in flexible, bulk heterojunction, OPDs, which open the possibility of replacing the traditional ITO substrate. The GO-based OPDs showed a power-conversion efficiency of 1.1% with 70% transparency.³⁵⁵ Many reports on the good optical transmittance and excellent electrical conductivity of G layers have been published,^{346–355} but studies are limited on the transparent conducting property by coating the G layers onto fabricated solar cells. Additionally, difficulties arise in the transfer of a uniform G/GO layer onto highly textured surfaces, and this may limit its possible large-scale production.

Dye-sensitized solar cells (DSSCs) are attractive as they are environmentally friendly, economical, and exhibit high energy conversion efficiency.^{356,357} In DSSCs, the electrons are injected from photo-oxidized dyes into TiO₂ nanoparticles, and the resulting oxidized dyes are regenerated by electrolytes. At a counter electrode (CE), I^- ions reduce the oxidized dyes, yielding I_3^- , and the resulting I_3^- ions are finally reduced to I^- . Thus, the CE plays an important role in enhancing DSSC

performance by catalyzing reduction of the electrolyte. The electron transport in disordered TiO_2 nanoparticles with a random transit path increased the charge recombination, thereby reducing the photocurrent and the efficiency of the DSSCs. Fabrication of photoanodes with a fast transport pathway is still a challenge for DSSCs. In this sense, Cheng et al.³⁵⁸ prepared hybrid materials of anatase TiO_2 nanoparticles on rGO sheets (TiO_2/rGO) for application in DSSCs. These hybrid photoanode materials exhibited a better efficiency (7.68%) in DSSCs than that of the pure TiO_2 (4.78%), suggesting that the introduction of G accelerates the electron transfer and decreases the charge recombination. Bi and co-workers³⁵⁹ developed a quasi core-shell structure of N-doped G/cobalt sulfide (NDG/CoS) as a CE for DSSCs, which exhibited a high short-circuit current density (20.38 mA cm^{-2}) and an energy conversion efficiency of 10.71% (see Figure 64). The remarkable perform-

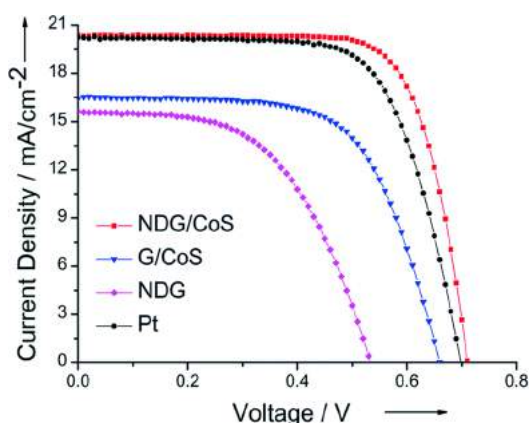


Figure 64. DSSCs performance with NDG/CoS, G/CoS, NDG, and Pt as CEs. Reprinted with permission from ref 359. Copyright 2014 Royal Society of Chemistry.

ance of these DSSCs is attributed to the core of CoS nanoparticles coated with a shell of ultrathin NDG layers that act as conductive paths to overcome the problem of low conductivity caused by grain boundaries and defects between the CoS nanoparticles.

Much effort is still required to either replace Pt in DSSCs with less expensive alternative materials or to develop easier low-temperature approaches, which employ reduced amounts of Pt; in this vein, easy, cheap, and room-temperature processes are of vital interest for DSSC commercialization. Additionally, the DSSC energy conversion efficiency with various types of hybrid materials is still lower than $\sim 11\%$, which is much smaller than commercial solar cells. Thus, further developments are required to obtain a much larger DSSC efficiency to be compatible with the recent developments of perovskite solar cells,^{360,361} which shows $\sim 20\%$ efficiency, although these perovskite-based devices are not yet stable enough for practical applications.

Noncovalent functionalization at the interface of G/GO by doping, chemical/physical modification, and nanoparticle coating could be one of the best approaches to greatly tune the nanostructure and chemophysical properties toward the development of high performance electrode materials in energy storage applications. Although several reports on noncovalent functionalization of G/GO with different morphologies as energy materials have been published, there is still a long way to go before its wide use in industrial applications.

5.3. Water Splitting

The production of hydrogen from H_2O would generate a new era of cheap, clean, and renewable energy such as hydrogen fuel cells and liquid fuels synthesized from syngas and CO_2 . The electrocatalytic hydrogen evolution reaction (HER) from water is a process that has attracted much attention due to its high energy conversion efficiency. More recently, molybdenum (Mo)-based materials as electrocatalysts have been shown as the most effective HER, while their commercialization is obstructed by durability. Recently, MoS_2 ,³⁶² MoSe_2 ,³⁶³

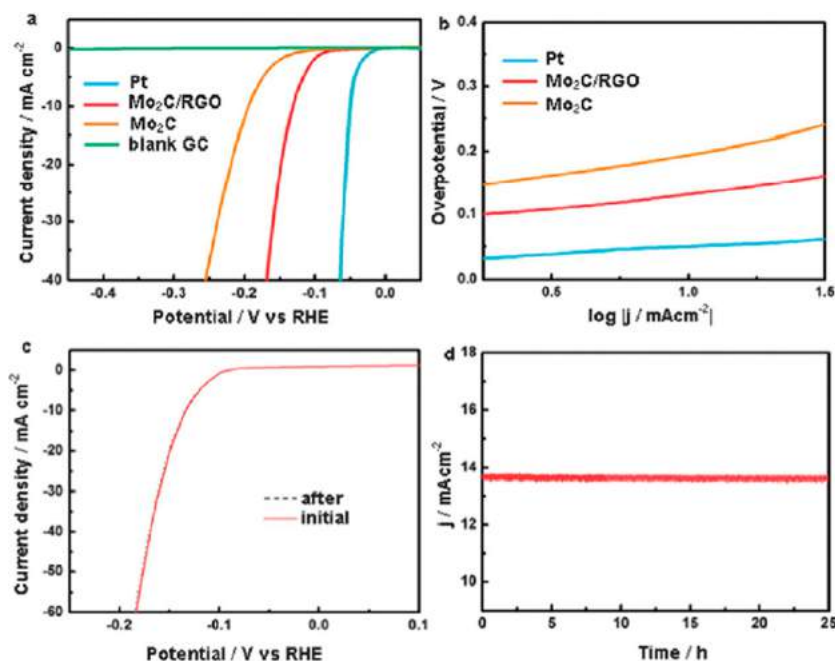


Figure 65. (a) HER polarization curves for catalysts, (b) Tafel plots, (c) stability test of Mo_2C -rGO hybrid, and (d) time dependence of current density of Mo_2C -rGO hybrid at an applied potential of 140 mV. Reprinted with permission from ref 373. Copyright 2014 Royal Society of Chemistry.

Mo₂C,³⁶⁴ MoB,³⁶⁵ MoS₂ analogues,³⁶⁶ NiMoN_x,³⁶⁷ Co_{0.6}Mo_{1.4}N₂,³⁶⁸ Mo₂N,³⁶⁹ and MoO₂³⁷⁰ have been employed as electrocatalysts for the HER in acidic/basic electrolytes; however, the durability of Mo-based catalysts is still not satisfactory in the presence of acidic or base electrolytes under the long-term or accelerated test. Chang et al.³⁷¹ employed the thermolysis of ammonium thiomolybdates in a CVD chamber to grow MoS_x on G-coated 3D Ni foams at various temperatures. Subsequently, the MoS_x/G/3D Ni foam electrode was used for electrocatalytic HER. According to their results, the G sheets on Ni foam gave the Ni protection against etching and increased the stability of working electrode in strong acid media. Additionally, these electrodes showed a large hydrogen production of ~302 mL g⁻¹ cm⁻² h⁻¹ (13.47 mmol g⁻¹ cm⁻² h⁻¹) at an overpotential of $V = 0.2$ V and an improved current density of ~45 mA cm⁻² at 0.2 V, due to the presence of bridging S₂²⁻ or apical S²⁻ in amorphous states.³⁷¹ Among the various types of Mo-based electrocatalysts, Mo₂C/G materials display remarkable HER activities and stability, including small overpotentials, large cathodic current densities, and high exchange current density under acidic and basic conditions. These properties are believed to be due to their unique d-band electronic structures (electronic structure like a noble metal).³⁷² Pan et al.³⁷³ developed Mo₂C nanoparticles on GO sheets, and they found that the Mo₂C nanoparticles were stabilized by a carbon layer. The Mo₂C-rGO hybrid showed an overpotential voltage of ~70 mV, and the cathodic current increased rapidly under more negative potentials. Notably, Mo₂C-rGO exhibited a large HER performance (mass activity ~77 mA mg⁻¹ at 150 mV), a low Tafel slope (57.3 mV decade⁻¹), and good stability (stable after 1000 cycles (see Figure 65)).³⁷³ The improved activity and stability were ascribed to the large surface area of the G support and the improved conductivity of the Mo₂C-rGO hybrid.

In a separate work, Xu et al.³⁷⁰ employed the MoO₂/rGO hybrid as a highly efficient HER. They reported that the presence of oxygen-containing groups limits the growth of MoO₂ nanoparticles to a tiny size due to the space confinement effect between GO layers. The MoO₂/rGO hybrid display good HER activity with a low onset overpotential of 190 mV, a high cathodic current density, and a low Tafel slope (49 mV decade⁻¹) due to a synergistic effect between metallic MoO₂ nanoparticles and G with electronic communication promoted by an interface interaction. More recently, Zhang and co-workers³⁷⁴ reported an amorphous MoS_xCl_y as a high-performance electrocatalyst for electrochemical hydrogen productions. These electrocatalysts showed large cathodic current densities and small Tafel slopes (~50 mV decade⁻¹), which are attributed to the synergistic effects of a remarkable intrinsic activity of the MoS_xCl_y catalyst and a large active surface area. The recent work by Zhou et al.³⁷⁵ on HER activity using N-doped carbon-wrapped Co nanoparticles with a size of ~15 nm supported on N-doped G nanosheets (Co@NC/NG) is very interesting. The Co@NC/NG electrode exhibited a small overpotential (-49 mV) and small Tafel slope (79.3 mV decade⁻¹) due to carbon atoms promoted by the entrapped cobalt nanoparticles. It was found that the strong synergetic interaction between the G/GO and nanoparticles enhanced the charge separation and affected the band structure of G/GO. However, the properties of G/GO nanoparticle hybrids are usually ignored when G/GO is used as the electron acceptor and transporter. Furthermore, the defects in G/GO nanoparticles hybrids are essential for their electronic properties, and play a key role in improvement of the HER stability and activity of the supported catalysts. Accordingly, the

structure defects of G/GO in G/GO-nanoparticle hybrids should be further researched, because they might be the active sites for hydrogen production. Moreover, the development of nonprecious catalysts with activities better than commercial Pt/C is still a big challenge for researchers who want to apply this technology in large-scale applications.

5.4. Green Chemistry and Environments

Noncovalently functionalized G/GO materials hold promise in the development of sustainable catalysts for green chemistry with low emissions and high selectivity. Therefore, the use of these materials in the growing field of “catalysis and environmental green chemistry” has become important due to their unique chemical properties, high mechanical resistance, and their favorable charge generation and transportation in catalysis and environmental processes. The G, GO, and its reduced oxide are necessary to disperse the materials in water for their application in the field of catalytic reaction and environmental pollution.³⁷⁶ Achari et al.³⁷⁷ developed highly aqueous dispersible aminoclay-rGO (AC-rGO) hybrids by the in situ condensation of aminoclay over GO followed by hydrazine reduction (see Figure 66). They found that these amphiphilic hybrid materials with

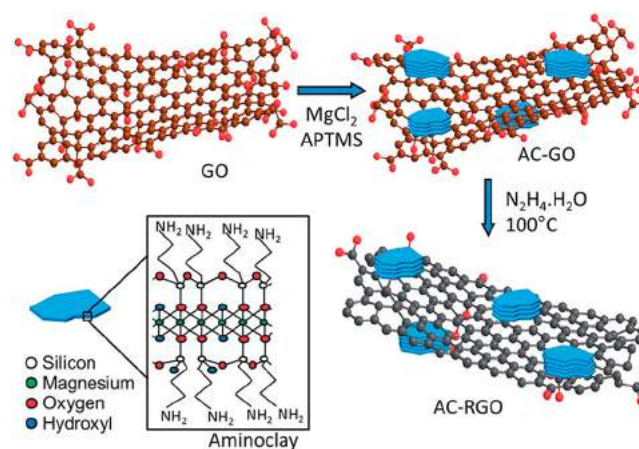


Figure 66. Synthesis of AC-GO and AC-rGO hybrids. The blue platelets represent aminoclay, while the brown and gray sheets show GO and rGO, respectively. Reprinted with permission from ref 377. Copyright 2013 Royal Society of Chemistry.

high concentrations of 7.5 mg rGO/mL are stable in water solution and display simultaneous adsorption of Cyt-C via hydrophobic interaction and DNA via electrostatic interaction. In a separate study, McCoy and co-workers³⁷⁸ employed noncovalent magnetic control to reversibly recover GO using iron oxide (Fe₂O₃) in the presence of magnetic surfactants. Because the GO is unchanged, there is no loss of its original properties; thus, the GO and magnetic material can be reused (see Figure 67a). Because of large differences in the isoelectric point of GO (pH ≈ 0) and Fe₂O₃ (pH ≈ 7), a wide gap is present in which the two materials show opposite surface charges (see Figure 67b), and thus the separation could be attributed to Coulombic attraction. The recyclable nature of this assembly and the large adsorption capacity of GO indicate the materials' potential use in applications for decontamination and water treatment.³⁷⁹ Zubir and co-workers³⁸⁰ achieved efficient Acid Orange 7 (AO7) degradation using a GO-Fe₃O₄ hybrid. These enhancements were attributed to the synergistic effects between both optimized GO amount and Fe₃O₄ nanoparticles. This can be explained by several factors: First, the large surface area of

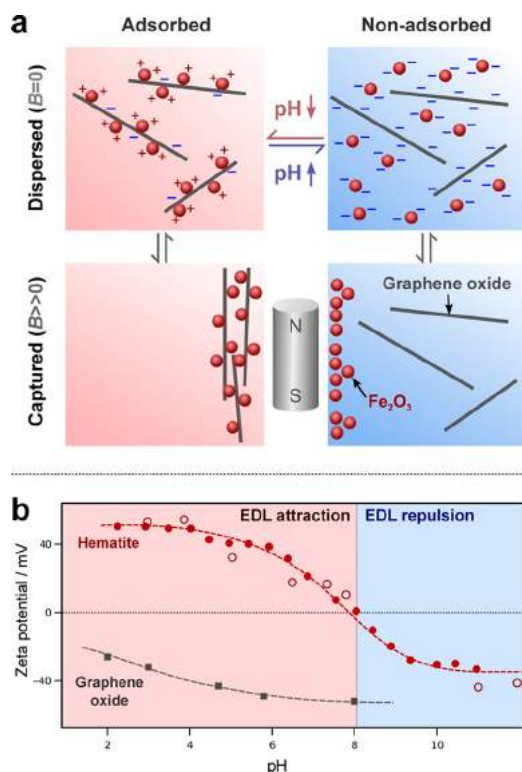


Figure 67. (a) Schematic diagram of the basic concept of the experiment: proper pH is used to affect charge attraction/repulsion between the GO sheets and Fe_3O_4 nanoparticles. Fe_3O_4 nanoparticles separated from solution or dispersion by applied magnetic field. (b) Zeta potentials of GO and Fe_3O_4 nanoparticles. Reprinted with permission from ref 378. Copyright 2015 American Chemical Society.

exfoliated GO provides a uniform dispersion of Fe_3O_4 nanoparticles onto the surface of GO sheets, which is good for increasing the mass transfer of reactants toward the active ($\equiv \text{Fe}^{2+}/\equiv \text{Fe}^{3+}$) sites during the decontamination.³⁸⁰ Second, GO has a large aromatic ring structure on its basal plane that supports AO7 adsorption via π – π interactions, which allows enhanced AO7 concentration within the active sites to be oxidized faster by the generated hydroxyl radicals (OH^\bullet).³⁸⁰ Third, the strong interaction between Fe_3O_4 NPs and GO through Fe–O–C bonds accelerates the electron transfer between the nanoparticles and GO sheets.³⁸⁰ Finally, the synergistic effect between GO and Fe_3O_4 nanoparticles promotes the regeneration of ferrous irons to quicken the redox cycle on active sites, consequently enhancing the AO7 degradation and mineralization.³⁸⁰ Liu et al.³⁸¹ synthesized halloysite nanotubes (HNTs) loaded on rGO sheets (abbreviated as HGC) via an electrostatic self-assembly process for removal of dyes from water. The electrostatic force occurred between the negative rGO sheets (van der Waals forces and hydrogen bonding) and HNTs positively charged by γ -aminopropyl triethoxysilane (APTES) functionalization. The rhodamine B (RhB) adsorption on HGC was $\sim 45.4 \text{ mg mg}^{-1}$ after seven cycles due to the big pore volumes, large surface area, the strong π – π stacking interactions, and its abundant functional groups on the surface. Le and co-workers³⁷⁹ also developed a 3D microhydrogel of nanoparticle/G platelets by reversible self-assembly and aqueous exfoliation. These 3D hydrogels showed excellent methylene blue dye removal (adsorption capacity = 685 mg g^{-1}) and photocatalytic dye degradation due to the presence of large surface area ($1677 \text{ m}^2 \text{ g}^{-1}$), low band gap (1.8 eV), and good charge separation and rapid electron transfer.³⁷⁹ Dong et

al.³⁸² developed bioinspired surface functionalization of GO for dye and heavy metal ion adsorption. The poly dopamine (PD) functionalized GO (PD/GO) had superior Eschenmoser-containing dyes' adsorption capacity up to 2.1 g g^{-1} .³⁸² Additionally, PD/GO also showed good adsorption capacity for heavy metal ions (53.6 mg g^{-1} for Pb^{2+} , 24.4 mg g^{-1} for Cu^{2+} , 33.3 mg g^{-1} for Cd^{2+} , and 15.2 mg g^{-1} for Hg^{2+}), suggesting it is a promising adsorbent for decontaminating wastewater.³⁸² Mondal and co-workers³⁸³ developed a bifunctionalized G and expanded graphite using *n*-butyl lithium, and this material was then applied in efficient dye adsorption from dye contaminated water by noncovalent interaction between the dye and the COOH groups of the graphenic plane. In a recent report, Liang and co-workers³⁸⁴ developed a facile and efficient electrostatic self-assembly strategy for improving the interfacial contact between rGO and MIL-53(Fe) (termed as M53–rGO). The M53–rGO hybrid displayed excellent photocatalytic activity (reduction of Cr(VI) rapidly increased to 100% under visible light illumination), which is attributed to a decrease in the recombination of photogenerated electron–hole pairs. It is believed that the good interfacial contact between MIL-53(Fe) and rGO facilitates the transfer of photogenerated electrons. These results open potential applications for the M53–rGO hybrid in industrial wastewater treatment.

G sheets have many advantages such as availability, solubility, high quality, environmentally friendly nature, and inexpensive, large-scale production; these benefits open an opportunity for exploring novel adsorption and degradation by synthesizing noncovalently functionalized G/GO hybrids. The existence of G/GO in the hybrid provides superior applications in different kinds of dyes adsorption/degradation from water due to the presence of large surface area, pore volume, and good active sites for chemical reactions.

5.5. Nano-Devices

Self-assembly and grafting of G/GO onto carbon fibers have been found to enhance the interfacial bonding with a shape memory polymer (SMP) matrix via van der Waals forces and covalent cross-link.³⁸⁵ This effective approach remarkably improved the electrical properties and recovery performance of SMPs that are used for Joule heating triggered shape recovery at a lower electrical voltage.^{386,387} The electrical conductivity was further upgraded when nanoparticles were introduced into SMP composites because they reduce the gap between G/GO. With these scenarios in mind, it is evident that G/GO holds great promise for application in nanodevices. Basically, two mechanisms are involved in self-assembly of stable monolayers of alkane chain molecules on graphene:³⁸⁸ (i) bonds between the G/GO and the molecular “anchor” group (many reports have been given on interactions of ammonia molecules with the surface of G/GO by monitoring charge transport in G field-effect devices as a function of gas exposure),^{1,389–392} and (ii) interchain interactions, for instance, van der Waals forces and hydrogen bonding.³⁹³ Recently, Wang and co-workers³⁹⁴ synthesized a polymer-functionalized rGO from a noncovalent functionalized pyrene-terminal polymer in benzoyl alcohol. They reported that these sheets exhibit organo-dispersibility, high grafting density, high electrical conductivity (see Figure 68), and good processability. Georgakilas et al.¹⁷⁰ prepared hydrophilic functionalized MWNTs and stabilized a large amount of pristine G sheets in water without the use of surfactants, ionic liquids, and hydrophilic polymers. The multidimensional (2D/1D) G/MWNTs composite exhibited a stable water dispersion at

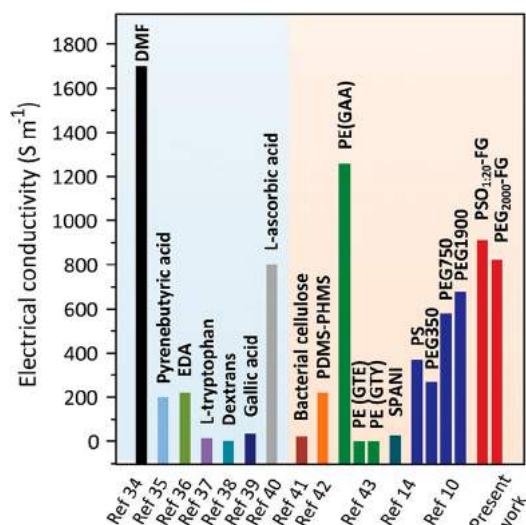


Figure 68. Conductivity of various hybrid materials of G/rGO. Reprinted with permission from ref 394. Copyright 2015 Royal Society of Chemistry.

concentrations up to 15 mg mL^{-1} and also was dispersible in other polar solvents.¹⁷⁰ Interestingly, these composites exhibited excellent conductivity (sheet resistance up to $R_s \approx 25 \Omega \square^{-1}$ for free hybrid material and $R_s \approx 1300 \Omega \square^{-1}$ for a polyvinylalcohol/hybrid composite film) after coating on paper by drop casting a dispersion of the water-soluble polymers.¹⁷⁰

In a separate study, Song et al.⁹⁴ developed epoxy–G hybrids with good thermal conductivity by using nonoxidized G flakes (GFs) through noncovalent functionalization. The noncovalently functionalized GFs, with 1-pyrenebutyric acid, stimulate dispersion of GFs in organic or aqueous solvents with high solubility and stability. The interfacial bonding between GFs and the polymer matrix was found to be responsible for the superior thermal conductivity enhancement.⁹⁴ Kozhemyakina and co-workers³⁹⁵ achieved electronic communication between G and perylene bisimide via titration experiments, when both materials are either coated on a surface or dispersed in a homogeneous solution. This interaction is facilitated by the noncovalent binding of their conjugated π -systems.³⁹⁵ The electronic properties of G can be tuned by modification with organic molecules; for example, dye molecules containing a conjugated

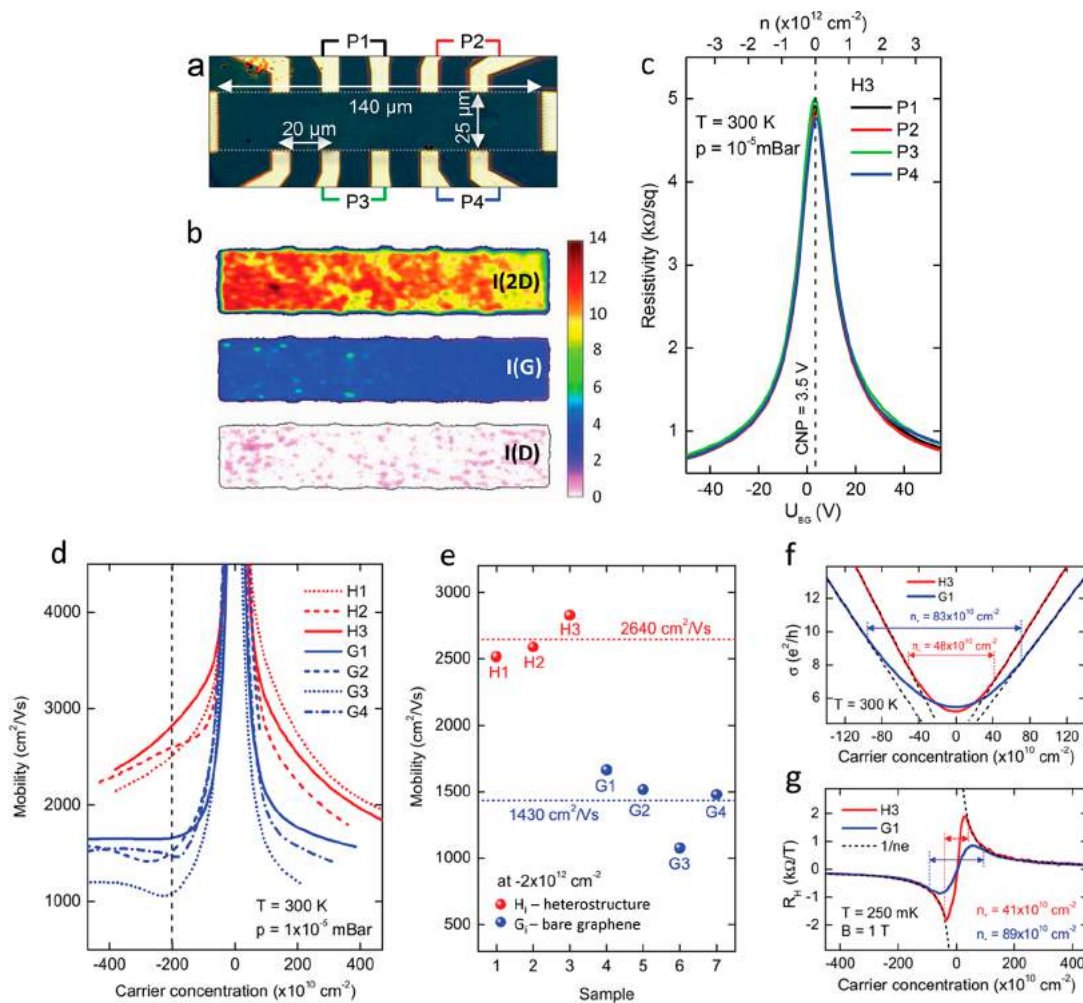


Figure 69. Electric transport calibrations of G and heterostructure (H) electric field devices. (a) Optical microscope image of the H-device. (b) Raman mapping of 2D, G, and D peaks. (c) G resistivity at various position contacts (P1–P4) versus back-gate voltage (U_{BG}) at room temperature. (d) Electric charge mobility of G in H- and G-devices versus carrier concentration (n) at room temperature. (e) The electric charge mobility in H- and G-devices at $n = -2 \times 10^{12} \text{ cm}^{-2}$. (f) Conductivity of G in H3 and G1 in the vicinity of their charge neutrality points at room temperature. (g) Electrons and holes coexistence represented by Hall coefficient calibrations for devices H3 and G1 at a magnetic field of 1 T and a temperature of 250 mK. Dashed lines showed the single-particle model for holes and electrons. Reprinted with permission from ref 397. Copyright 2014 Wiley-VCH.

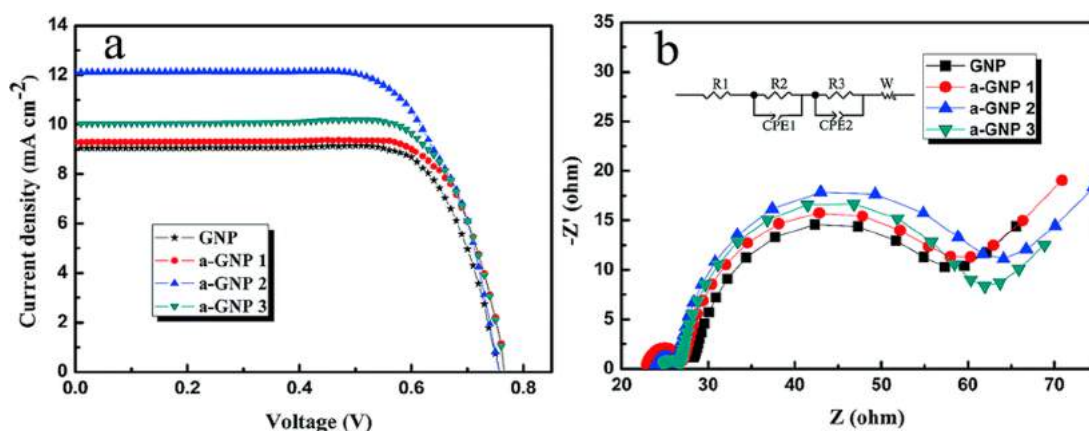


Figure 70. Photovoltaic and impedance performances of the DSSCs with different G/TiO₂ photoanodes. Reprinted with permission from ref 408. Copyright 2015 Royal Society of Chemistry.

π -system can be utilized to change the electronic structure of G. In this vein, Parvez and co-workers³⁹⁶ have fabricated organic field-effect transistors on G sheets. The highly conductive (sheet resistance $\sim 4.8 \text{ k}\Omega \square^{-1}$) G sheets were achieved in high quality and high yield ($>80\%$) by electrochemical exfoliation of graphite. They also reported that the G had a large sheet size, low oxygen content, and/or high C/O ratio as well as good electronic properties.³⁹⁶ Noncovalent functionalization of G by van der Waals forces provides another method for fabrication of electronic devices as it does not induce severe changes into G. For example, Woszczyzna et al.³⁹⁷ and Nottbohm et al.³⁹⁸ developed a simple approach to such functionalization by using mechanical stacking of an amino-terminated carbon nanomembrane (NH₂-CNM) and single-layer G (SLG) sheets. The electric transport performances of these bare G and heterostructure (H) electric field devices are displayed in Figure 69. Raman mapping of D, G, and 2D peaks (see Figure 69b) exhibits the materials' excellent structural quality and homogeneity on a large scale, which is further confirmed by electric transport measurements (see Figure 69c–g). They found that the intrinsic electronic quality of pristine SLG sheets is preserved in the heterostructures, thereby opening many possibilities for the use of G-based electronic in nanodevices. Halik et al.³⁹⁹ reported a simple approach to fabricate oxo-functionalized graphene/polymer composite for low-voltage operating memory devices. These devices can be operated at 3 V. They also found that the thin film coating ($\sim 5 \text{ nm}$) is mandatory to make the memory device function at low voltage. Additionally, a self-assembled monolayer of an imidazolium derivative further improves the function of the memory device.

Various types of molecules have been connected to G/GO through π - π stacking, and interfacial interactions between molecules and epoxy groups have been increased; this, in turn, has led to improvements in electrical and thermal conductivity.^{1,94,170,385–395} However, this approach requires a further investigation and progress because of some serious limitations in industrial level application such as the high costs of organic/inorganic derivatives and time-consuming, tedious synthesis.

5.6. Catalysis and Photocatalysis

Noncovalent functionalization of G/GO with nanoparticles may lead to light harvesting and charge transfer features. In these materials, the lattice structure of G/GO remains intact and exhibits most of its intrinsic electronic properties. Thus, the hybrid materials of G/GO with nanoparticles bear great potential

for catalysis and large-scale energy storage conversion applications, particularly when photo- and redox active chromophores, such as porphyrins or phthalocyanines, are involved in the graphite exfoliation and G stabilization. Recent studies on zinc(II) alkylsulfonylphthalocyanine–pyrene conjugate (ZPC) with highly exfoliated graphite and their photo-physical properties reported by Roth et al.⁴⁰⁰ are intriguing. In their report, the authors showed that ZPC stabilizes single layer G during the ultrasonication of graphite by virtue of strong electronic interactions of the hybrid in both the ground and the excited states. The presence of the pyrene functional group in the conjugate is crucial in respect of noncovalently immobilizing the electron accepting phthalocyanines onto the basal plane of graphite.⁴⁰⁰ Wang et al.⁴⁰¹ developed a 3D mesoporous Fe₃O₄@Cu₂O–GO framework as an efficient and recyclable catalyst for the synthesis of quinoxalines by using different substituents, that is, electron-rich and electron-withdrawing groups *o*-phenylenediamine and terminal alkyne, respectively. This 3D mesoporous framework exhibited good catalytic activity, selectivity ($>99\%$), and recyclability after nine cycles, and this is believed to be due to its large surface area, large pore volume, unique structure, impressive mass transport, and application of an external magnetic field.⁴⁰¹ Further catalytic activity can be enhanced by increasing the active surface area of hybrid catalysts, that is, reducing the nanoparticle size ($<2 \text{ nm}$). However, reducing the size of particles to less than 2 nm is limited by the conventional methods that utilize templates such as surfactants or dendrimers, which unfortunately can form barriers that confine the catalytic activity. Ren and co-workers⁴⁰² created a new catalyst containing 1–2 nm Au nanoparticles (NPs) anchored to thiophenol functionalized G sheets (Au/TGS). The Au/TGS catalysts exhibited better catalytic activity for the reduction of 4-nitrophenol because of the synergistic effects between the TGS and Au NPs and the high utilization of the metal catalyst. Besides catalytic reactions, many efforts have been made to enhance the photocatalytic activity of G/GO and nanoparticle hybrid materials.^{403–406} Joseph and co-workers⁴⁰⁷ fabricated a π - π stacked anchored by squaraine dye (VJ-S) sensitized r-NGOT (hybridized r-NGO and TiO₂ in a self-assembled core/shell structure (VJ-S/r-NGOT)) material and evaluated its photocatalytic activity and H₂ evolution performance. The direct charge transfer and π - π interaction between VJ-S and r-NGOT occurred due to the presence of an electron-deficient center in the VJ-S. The VJ-S/r-NGOT displayed better photocatalytic production of hydrogen (apparent photonic efficiency = 0.91%)

under visible light because VJ-S dye absorbs visible and near IR (NIR) wavelengths and gives a direct energy transfer to r-NGOT.⁴⁰⁷ Ma and co-workers⁴⁰⁸ enhanced the short circuit current and energy conversion of an DSSC by 35.8% and 26.8%, by incorporating activated G nanoplatelets (a-GNPs, 0.02 wt %) into a TiO₂ film photoanode (see Figure 70). They also reported that an appropriate a-GNPs amount and a 3D nanostructure act as an efficient pathway for electrolyte ions and electrons, facilitating the rapid electron transfer and charge separation and suppressing the electron recombination and back transport reaction in DSSCs.⁴⁰⁸

Xu et al.⁴⁰⁹ reported in a theoretical study the effect of O atoms on photocatalytic hydrogen evolution in g-C₃N₄ and rGO sheets hybrid materials. Interestingly, they showed that the O concentration changes the direct-gap hybrid to an indirect-gap one. Moreover, they showed that the interfaces in g-C₃N₄/rGO-3 and g-C₃N₄/rGO-4 hybrids are type-II heterojunction, and negatively charged O atoms in the rGO are active sites, which lead to high-efficiency photocatalytic generation of hydrogen (see Figure 71).⁴⁰⁹ Another experiment reported that rGO does

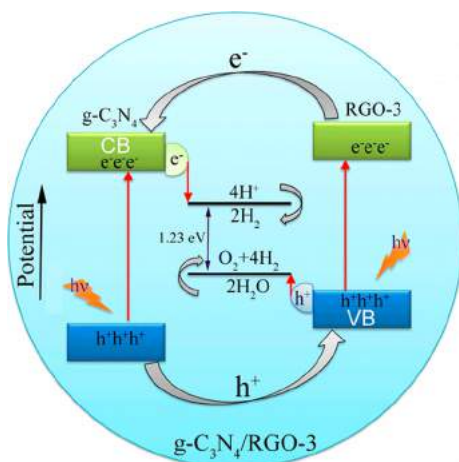


Figure 71. General mechanism for H₂ evolution from photocatalytic water splitting by the g-C₃N₄/rGO-3 hybrid, in which g-C₃N₄ acts as an electron sink providing the separation of electron–hole pairs and collects the electrons injected from the photoexcited rGO-3 for subsequent H₂ production from reduction of H₂O. Reprinted with permission from ref 409. Copyright 2015 American Chemical Society.

not affect the charge separation process but drastically increases the lifetime of photogenerated charge carriers.⁴¹⁰ In a recent study, Feifel and co-workers⁴¹¹ developed a very simple way to generate a high photocurrent by using the photosystem I (PSI) on artificial interfaces of π -system-modified G electrodes. They concluded that the improved photocatalytic activity of the π -system-modified G electrodes could be attributed to the surface property adaptation and the excellent conductivity of G. The main benefit of coupling PSI to the modified G by covalent binding is reflected by the light-power dependency study, which shows a distinctly good current conversion under the light.⁴¹¹ Moon et al.⁴¹² systematically explored the interaction of rGO and TiO₂ for efficient solar production of H₂O₂. They reported not only an organic-electron-donor-free, but also a noble-metal-free TiO₂-based photocatalytic system for the production of H₂O₂ up to a millimolar level, and interestingly in situ formation of cobalt phosphate was achieved on the rGO/TiO₂ hybrid. Lee et al.⁴¹³ developed a 3D monolayer G and TiO₂ assembly for high-efficiency electrochemical photovoltaic cells. A 3D nanostructure

with high carrier mobility gives a direct pathway for electrons to the current collector electrode for a photoanode in DSSCs. The energy conversion efficiency of DSSC was increased by ~10% under the optimized 3D hybrid structure, and this is due to improved light harvesting and reduced electron recombination at the photoanode.⁴¹³ Despite the excellent progress in higher catalytic and photocatalytic activity, these materials usually exhibit low selectivity to desired products or a high deactivation rate due to the gradual migration and agglomeration of the active phase during the reaction. In addition, most catalysts and/or photocatalysts reported so far are recovered by tedious filtration or centrifugation. Thus, methods toward the design and synthesis of more efficient catalytic or photocatalytic systems remain a challenge.

5.7. Biosensors and Bioimaging

Several studies have utilized noncovalently functionalized G/GO in biological applications, ranging from biosensing (human telomerase detection, disease-related diagnostics) to cell-imaging.^{414–418} Gu and co-workers⁴¹⁹ developed a superparamagnetic functionalized G/Fe₃O₄@Au hybrid for a magnetically controlled solid-state electrochemiluminescence biosensing. They found that the hybrid exhibited high sensitivity for HeLa cells with a linear range of 1–20 × 10⁴ cells/mL, long-term stability, high emission intensity, high reproducibility, excellent electron transfer, and superparamagnetic behavior. To directly sense atropine in complex matrixes, Bagheri and co-workers⁴²⁰ advanced the field by developing Co₃O₄–G-modified carbon paste electrodes for selective detection of atropine in biological fluids, that is, urine and human serum. They reported that the recovery of spiked atropine in biological samples displayed standard values in the range from 97.6% to 103.2%, indicating the successive applicability of the proposed strategy for real clinical applications. In a recent report, Yoon and co-workers⁴²¹ utilized a noncovalently functionalized GO sheet on a patterned Au surface to isolate circulating tumor cells (CTCs) from blood samples of pancreatic, breast, and lung cancer patients. The noncovalently functionalized GO/Au showed excellent sensitivity toward capture of CTC, even at very low concentrations of target cells (see Figure 72); the principle of capture was explained in terms of morphological features of Au surfaces.⁴²¹

In another study, a novel, all-electronic biosensor for the identification and quantification of opioids was developed by Lerner and co-workers.⁴²² It consists of an engineered μ -opioid receptor protein, with high binding affinity for opioids, which is chemically bonded to a G field-effect transistor to read out ligand binding. These G-based field-effect transistors are able to sense the opioid receptor antagonist naltrexone at ultralow concentrations (10 pg mL^{−1}). Recently, Singh et al.⁴²³ developed a noncovalently functionalized single layer G for sensitivity enhancement of surface plasmon resonance (SPR) immunosensors. There are two main goals for this approach: (i) amplification of the SPR signal through G, and (ii) control of the immobilization of biotinylated cholera toxin antigen on the copper coordinated nitrilotriacetic acid (NTA) functionalized G as a single layer (the NTA was attached on G via pyrene derivatives through π – π interactions).⁴²³ With this experimental setup, they reported the very low detection limit of 4 pg mL^{−1} for the anticholera toxin specific antibody.⁴²³ Because of the many advantages (i.e., label-free, real-time, and high-throughput) of SPR imaging (SPRi) techniques for immunoassays, it is frequently used in sensors, but this method suffers from unfavorable detection limits. In this regard, Hu et al.⁴²⁴

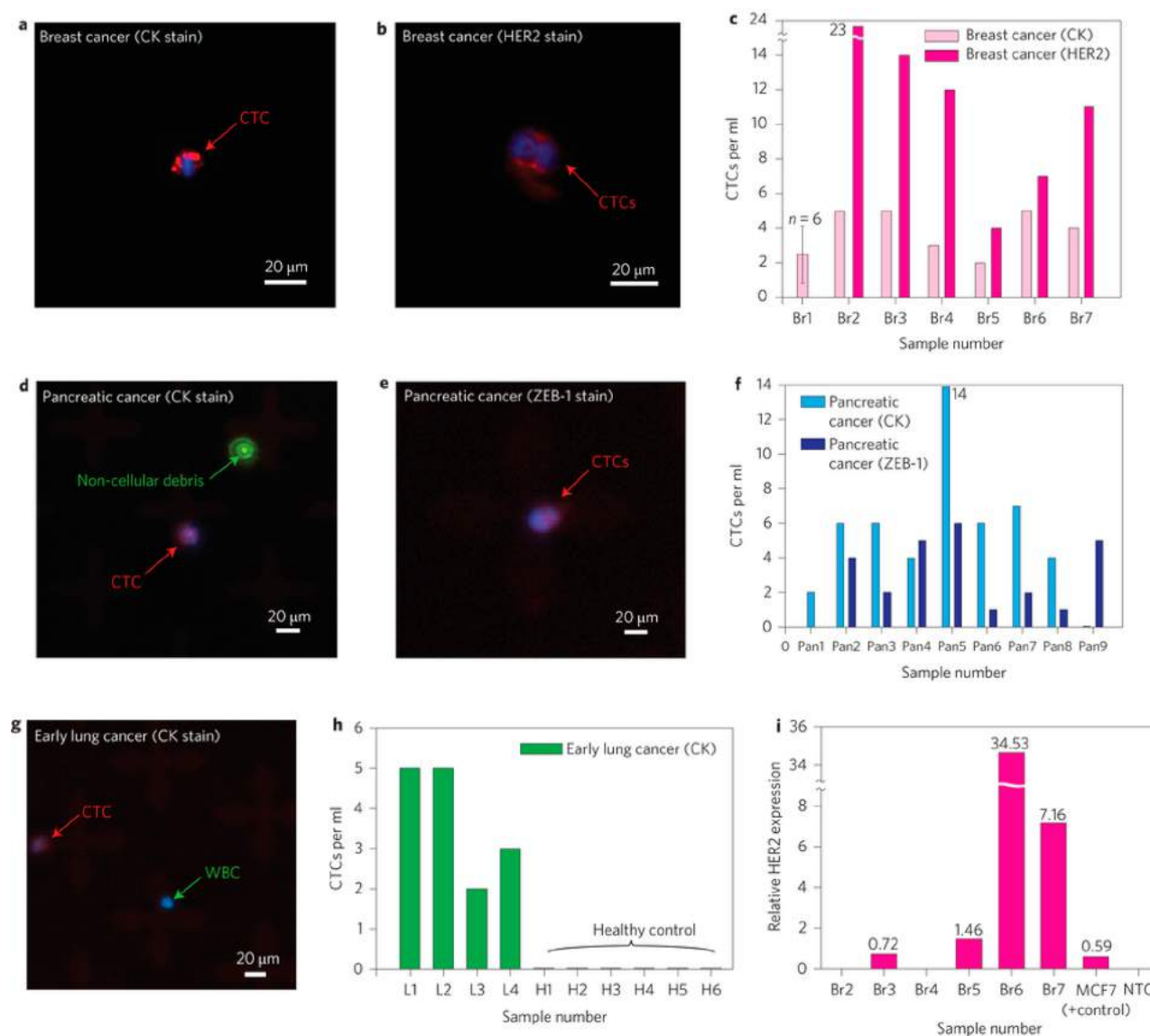


Figure 72. Capture of circulating tumor cells (CTCs) from breast cancer: (a) patient no. 6 (Br6); (b) patient no. 2 (Br2); and (c) quantification of CTCs. Capture of CTC from pancreatic cancer: (d) patient no. 2 (Pan2); (e) patient no. 9 (Pan9); and (f) quantification of CTCs. Capture of CTC from lung cancer: (g) patient no. 3 (L3); (h) quantification of CTCs; and (i) gene expression of captured CTCs via qRT-PCR. Reprinted with permission from ref 421. Copyright 2013 Nature Publishing Group.

developed a dual signal amplification strategy utilizing polydopamine (PDA) functionalization of rGO (PDA-rGO) sheets for detection of biomarkers. The PDA-rGO-based devices exhibited detection limits for model biomarker of 500 pg mL^{-1} on an ultralow fouling SPRi chip over a wide range of conditions (see Figure 73).⁴²⁴ Moreover, if HAuCl_4 solution was allowed to flow through the chip surface for the second signal amplification, the SPRi signals on sensing spots drastically increased due to the growth of gold nanostructures on the captured PDA-rGO sheets, while on the control spots where no PDA-rGO was captured, the SPRi signal changes remained negligible (see Figure 73e,f). This implies that flowing HAuCl_4 solution on the polymer brush-modified SPRi gold chip without precaptured PDA-rGO sheets does not lead to significant SPRi response; it is hypothesized that the densely packed polymer chains are able to efficiently prevent the HAuCl_4 from accessing the gold chip and, hence, the deposit does not interfere with the signal amplification. The observed behavior was explained in terms of

a high mass-density and dielectric constant of the gold nanostructures and the electromagnetic coupling between the gold nanostructures and the underlying gold thin film. Thus, as the deposition of gold exclusively takes place on PDA-rGO sheets, the SPRi signals stemming from the immunoassay were further efficiently and specifically enhanced by the second signal amplification, and the signal-to-noise ratio for the immunoassay was remarkably increased, securing improved performance.⁴²⁴

In a separate study, Yi and co-workers⁴²⁵ employed the advanced aptamer-two-photon dye (TPDye)/GO TPE (two-photon excitation) fluorescent nanosensing conjugate for in vitro or in vivo molecular probing in biological fluids, living cells, and zebrafish. They reported that the GO/aptamer-TPDye approach was a robust, sensitive, and selective sensor for quantitative detection of adenosine triphosphate (ATP) under the complex biological system with fast delivery into live cells or tissues and succeeded as a “signal-on” in vivo sensor for specific detection of target biomolecules.⁴²⁵ Castrignano and co-workers⁴²⁶ devel-

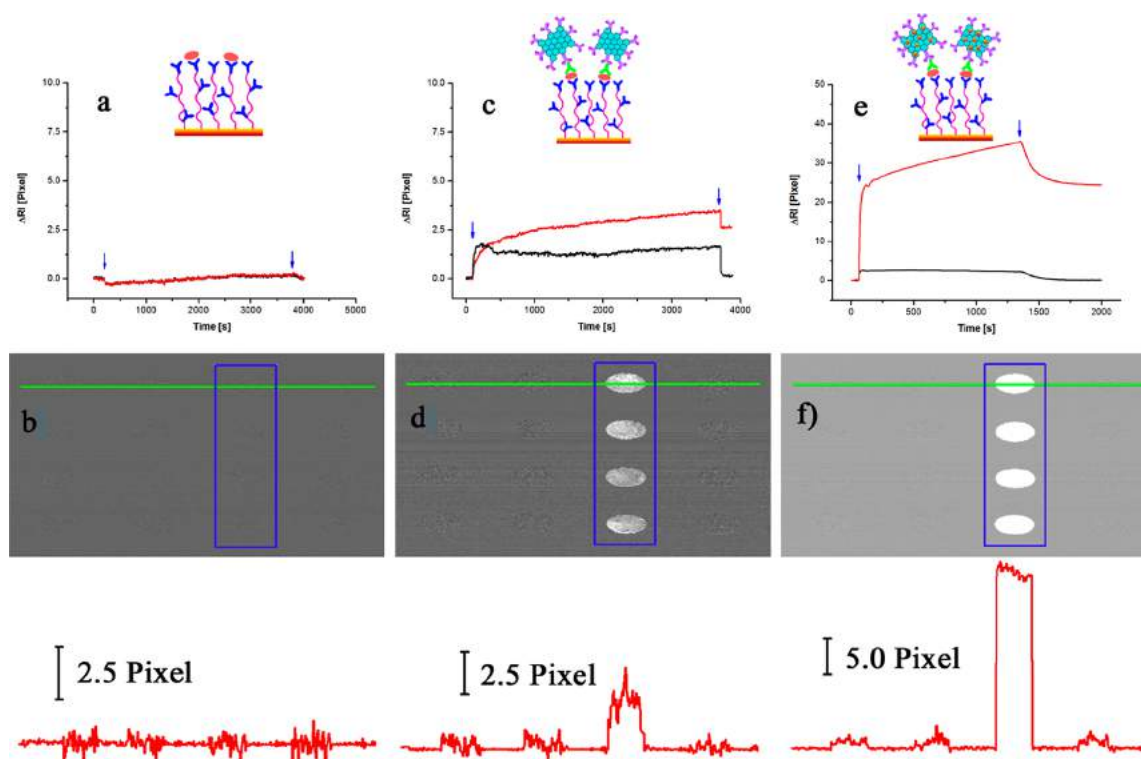


Figure 73. SPRi sensing profiles, differential images, and line profiles for detection in human serum: (a,b) Direct detection, (c,d) antibody-conjugated PDA-rGO for signal amplification, and (e,f) sequential Au coated. The red color line in panels (a), (c), and (e) displayed the results on the sensing point, and the black lines are collected from the control point. The blue boundaries in (b), (d), and (f) showed the four sensing points on the SPRi chip. Reprinted with permission from ref 424. Copyright 2014 American Chemical Society.

oped a drug screening based on human flavin-containing monooxygenase 3 (hFMO3 is the isoform present in the adult liver) immobilized on GO. The electrochemical property of hFMO3 was improved by GO in terms of electron transfer rate, current signal-to-noise ratio, and apparent surface coverage. Thus, this electrode showed good drug screening by N-oxidation of two therapeutic drugs, such as benzydamine and tamoxifen.⁴²⁷ Koninti et al.¹⁶² developed a GO-based molecular switching of ellipticine (E) to monitor the loading of anticancer drug onto GO and its release to DNA/RNA through direct optical detection. Formations of 3D assemblies involving GO and biomolecules by noncovalent interactions are responsible for biomolecule(s)-assisted fluorescence-switching of E. In another study, Xu and co-workers⁴²⁷ synthesized G/Cu nanoparticle hybrids (G/CuNPs) as a surface-enhanced Raman scattering (SERS) substrate for adenosine detection by means of chemical vapor deposition in the presence of methane and hydrogen. This hybrid exhibited a remarkable SERS improvement activity for adenosine (detected concentration in serum ~ 5 nM). On the basis of the above discussion, they found that the noncovalently functionalized G/GO can be used in the detection and imaging of biomolecules. These results open these materials to future applications in medicine and biotechnology. Another example of sensing application is the use of GO/CDs hybrid for the selective labeling of cell cytoplasm.⁴²⁸ Here, GO would act as a substrate for immobilization of quaternary ammonium modified carbon dots, thus enabling the preferential labeling of the cell cytoplasm while pristine carbon dots penetrate as fluorescent markers to the cell nucleus (see Figure 74).⁴²⁸

5.8. Biotherapeutics

There have been more concerns in medicine about fundamental approaches to deliver small molecule drugs/nucleotides/peptides to specific tissues.⁴²⁹ In this context, several studies have utilized G/GO in the delivery of chemotherapeutics for the treatment of cancer for a host of medical conditions, NIR phototherapy, and even for the stem cells proliferation and differentiation on G/GO surface.^{159,430–433} In this way, small-size GO (small-GO) sheets show high NIR light absorbance and biocompatibility for potential photothermal therapy.⁴³⁴ Moreover, GO displays excellent photothermal agent properties due to its nanosize, high photothermal efficiency, and low price as compared to other NIR photothermal agents such as gold particles and carbon nanotubes, etc. Figure 75 shows the effect of transdermal nano GO-hyaluronic acid (NGO-HA) conjugates for photothermal ablation therapy of melanoma skin cancer using a NIR laser.⁴³⁵ In this hybrid, HA works as a transdermal delivery carrier of chemical drugs and biopharmaceuticals. Jung et al.⁴³⁵ reported the photothermal ablation therapy of skin cancer by using the NGO and NGO-HA in SKH-1 mice inoculated with B16F1 cells on both dorsal flanks. The treatment NGO-HA showed that tumor tissues were completely ablated by the photothermal therapy with NIR irradiation (see Figure 76c). They also noticed that there was no recurrence of tumorigenesis in comparison to gradual tumor regrowth after photoablation applied to tumor tissues. On the other hand, PBS and NGO displayed no significant tumor ablation effect regardless of NIR irradiation (see Figure 76a,b).⁴³⁵ The better transdermal delivery was observed for NGO-HA hybrid to tumor tissues in the skin of mice. This may be due to highly expressed HA receptors and relatively leaky structures around

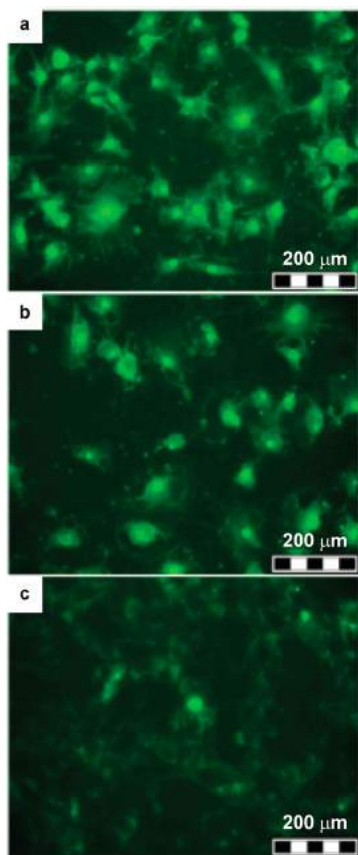


Figure 74. Fluorescence images of mouse fibroblast NIH/3T3 cells containing (a) CDs and (b,c) GO/CDs hybrids, demonstrating selective labeling of nuclei and cytoplasm. For pure carbon dots, a fast endocytosis occurred, and carbon dots readily entered cell nuclei (panel (a)). However, if GO/CDs hybrids were employed, penetration into cells was gradually inhibited upon increasing GO concentration (panels (b) and (c)). Reprinted with permission from ref 428. Copyright 2014 Royal Society of Chemistry.

tumor tissues, enabling the increased permeation and retention of nanoparticles.

For gene delivery, many reduction-sensitive biodegradable cationic polymers, which contain disulfide linkages, have been designed.⁴³⁶ These materials degrade inside cells due to high concentrations of glutathione in the cytosol, which may reduce cytotoxicity and enhance transfection efficiency by avoiding accumulation of high-molecular-weight polycations and facilitat-

ing rapid release of DNA into cells.^{436,437} Recently, Yang et al.⁴³⁸ introduced atom transfer radical polymerization (ATRP) initiation sites containing disulfide bonds onto surfaces of GO. They then modified the GO by ATRP with (2-dimethyl amino) ethyl methacrylate (DMAEMA) and synthesized a series of organic–inorganic composites (abbreviated as SS–GPDs) for efficient gene delivery (see Figure 77). They also showed that the SS–GPD materials can attach and absorb aromatic, water-insoluble drugs, such as CPT, for effective killing of cancer cells due to the conjugated structure of the GO basal plane.⁴³⁸ In summary, they were able to design a new class of gene/drug delivery systems by tuning the attached polycation side chains on GO surfaces in the presence of ATRP.

Noncovalently functionalized G/GO nanomaterials hold potential applications in the field of drug delivery due to their six-membered carbon ring structure, which can allow π – π interactions and hydrophobic interactions with aromatic rings of drugs.^{159,439} Additionally, glutathione (GSH) can also induce drug release caused by the disruption of noncovalent hydrophobic interactions and π – π stacking of GO aromatic rings.⁴⁴⁰ In the case of nucleus drug delivery, a drug-loaded GO should be able to escape from the endosome after endocytosis-mediated cellular uptake followed by the discharge of the drug from the carrier during the formation of the drug–proteasome hybrid.⁴⁴¹ The endosomal escape due to photothermally induced heat is possible, and the drug can also be released by GSH in the presence of NIR irradiation.⁴⁴² Kim and co-workers⁴⁴³ developed a nanosized PEG–BPEI–rGO composite consisting of rGO sheets covalently conjugated with branched polyethylenimine (BPEI) and polyethylene glycol (PEG). The water-stable PEG–BPEI–rGO could deposit a larger amount of doxorubicin (DOX) than unreduced PEG–BPEI–GO through π – π and hydrophobic interactions.⁴⁴³ Subsequently, the PEG–BPEI–rGO/DOX complex was tested for the photothermal effect by NIR irradiation in both test tubes and cells. Interestingly, they found that this hybrid could escape from endosomes after cellular uptake by photothermally induced endosomal disruption and the proton sponge effect, followed by GSH-induced DOX release into the cytosol.⁴⁴³ Yan et al.⁴⁴⁴ developed a smart G hybrid with singlet oxygen for the photodynamic treatment of cancer cells. They reported that GO can act as a singlet oxygen generation (SOG) controller, which can reversibly quench and recover SOG again after introducing a target molecule. This recovery relies on the interaction intensity between GO and a photosensitizer. They also found that this complex worked as a carrier for larger loading and delivery of the photosensitizers to cancer cells.⁴⁴⁴

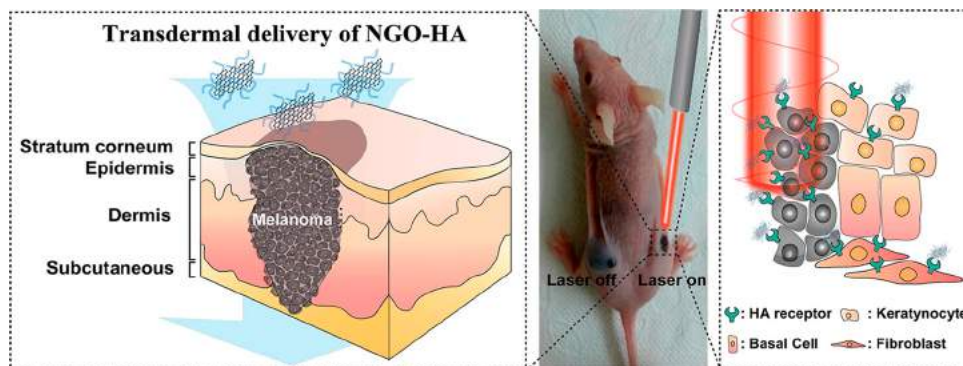


Figure 75. Schematic diagram for the transdermal delivery of nano GO–hyaluronic acid conjugates into melanoma skin cancer cells under a NIR laser. Reprinted with permission from ref 435. Copyright 2014 American Chemical Society.

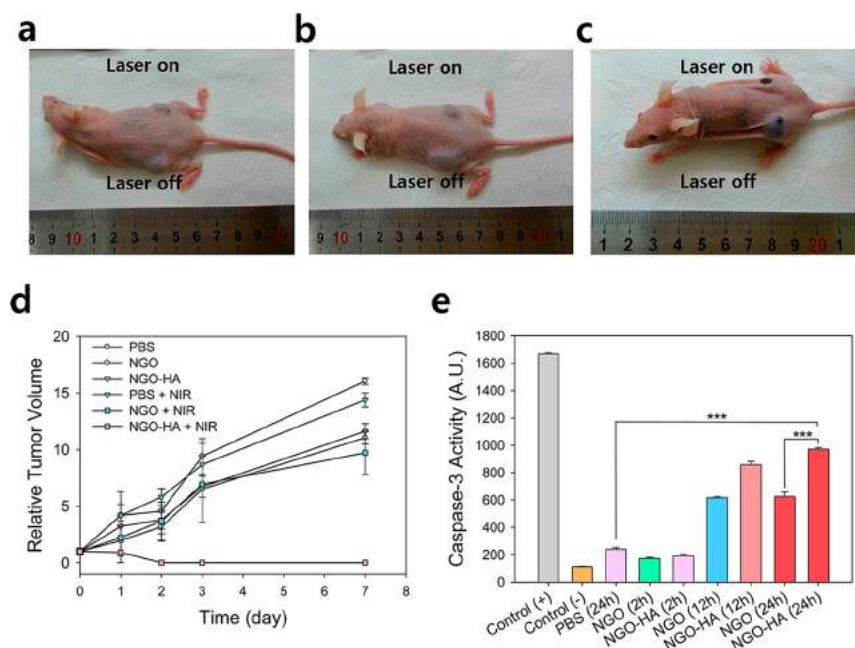


Figure 76. Pictures showing the effect of photothermal ablation therapy using NIR irradiation on the tumor growth in mice inoculated with B16F1 cells on both dorsal flanks after topical administration of (a) PBS, (b) NGO, and (c) NGO–HA. (d) Day-dependent relative tumor volume. (e) Time-dependent caspase-3 activity in tumor tissues to evaluate the heat-induced apoptosis (*** $P < 0.0001$). Reprinted with permission from ref 435. Copyright 2014 American Chemical Society.

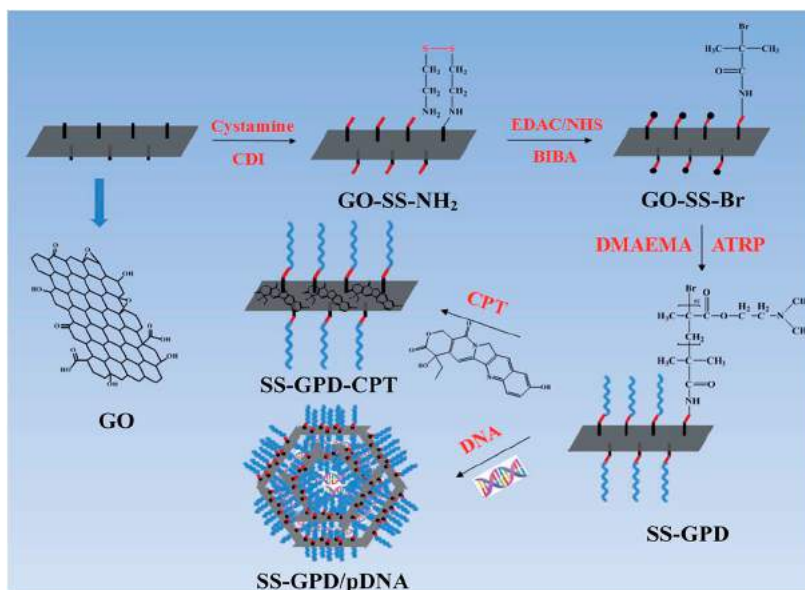


Figure 77. Schematic diagram for fabrication of biocleavable PDMAEMA–GO sheets by ATRP for gene/drug delivery. Reprinted with permission from ref 438. Copyright 2014 Royal Society of Chemistry.

More recently, Dong and co-workers⁴⁴⁵ conducted a specific-gene-targeting agent delivery for improved therapeutics by utilizing a multifunctional hybrid of poly(L-lactide) (PLA) and polyethylene glycol (PEG)-grafted GQDs (f-GQDs). PEG and PLA in noncovalent functionalization of GQDs can enhance the super physiological stability and durable photoluminescence over a wide range of pH values, which is utilized for cell imaging.⁴⁴⁵ These hybrids also showed improved biocompatibility and lower cytotoxicity. The targeting miRNA-21 agents were adsorbed on the high surface area of GQDs. Combined conjugation of miRNA-21-targeting and surviving-targeting agents displayed excellent inhibition of cancer cell growth and

more apoptosis of cancer cells; this suggests that noncovalent functionalization of GQDs can be utilized in biomedical application of intracellular molecular analysis and clinical gene therapeutics. Although noncovalently functionalized G/GO offers many possible applications in the biomedical field, it demonstrated high toxicity, which is one of the biggest drawbacks that limits its applications in humans.⁴⁴⁶ For this reason, further research is required to overcome this limitation.

6. CONCLUSIONS AND CHALLENGES

Noncovalent functionalization involving mainly π – π interactions, van der Waals forces, hydrogen bonding, ionic interactions,

or electron donor–acceptor complexes represents the strategic way to control the properties and improve the performance of G and GO in various advanced applications. In recent years, huge progress was registered in terms of theoretical description and experimental observation of interaction modes and morphological arrangements of various species onto G/GO surface also due to the unique contributions of ultrahigh vacuum scanning tunneling microscopy (STM). The STM description of the molecule assembly onto the G/GO substrate is still limited by the planarity and size of the studied molecules. From this point of view, the possibility to observe the interactions, conformations, and transformations of various larger molecules and biomolecules onto G/GO is still a big challenge with the possible principal impact in many sensing and biomedical applications. Another challenge is to increase the yield and quality of single-layer G produced by the chemical exfoliation of graphite in various organic solvents where π – π interactions constitute the main driving force.

A challenging issue is also to create Janus-like G composed of two different π – π stacked molecules on either side of the sheet (e.g., electron-donating and -withdrawing molecules) to tailor its electronic properties. Still, the noncovalent approaches possess limited success in the band gap control of G as compared to covalent routes starting from G, GO, or fluorographene and resulting in many new derivatives with variously opened band gaps. Similarly, neither G nor its derivatives exhibit self-sustainable magnetism despite many reported attempts to induce sp-based magnetism at room temperature. With this respect, the noncovalent functionalization of G/GO with magnetic nanoparticles (mainly iron oxides) provides an easy way to create a magnetically controllable system for delivery and separations in biomedicine or environmental applications. The use of suitable molecular species (molecular magnets) would be, in our opinion, another alternative with an advantage of the preservation of a 2D character of the magnetic hybrid.

Among tens of possible functionalization species, polymers play an important role mainly in noncovalent modification of G enhancing its hydrophilicity and biocompatibility. In the case of GO being hydrophilic due to the oxygen-bearing functional groups, the polymer functionalization brings an enhanced colloidal stability and suitable functional groups for further advanced nanoarchitecture for applications, for example, in targeted drug and gene delivery. Another interesting example of noncovalent functionalization is the creation of hybrids combining G/GO with other carbon nanoallotropes or G analogues. For example, the modification of G with OH-functionalized MWCTs resulted in a highly conductive and hydrophilic hybrid with a huge potential in the fields of conductive inks for inkjet printing or highly conductive polymers. The hybrids of G with other 2D analogues (e.g., MoS₂ or WS₂) create unique nanodevices acting as advanced biosensors, photoinduced memory device, Li-ion batteries, or field-effect transistors.

In the field of energy materials, the hybrids of G/GO with TiO₂ also have a strong position with many reported applications in LIBs and mainly in dye-sensitized solar cells. Such hybrid photoanode materials would exhibit higher efficiency as compared to pristine TiO₂ as G accelerates the electron transfer and decreases the charge recombination. However, the energy conversion improvement based on these hybrid materials is still a challenge mainly in terms of recent developments of perovskite-based solar cells.

Quantum dots (QD) are another important group of the nanomaterials discussed in this Review and commonly used for noncovalent modification of G/GO. These hybrids exhibit an excellent efficiency in many fields involving photocatalysis, supercapacitance, LIBs and NIBs, photoelectrochemical splitting of water, photosensitizers, water purification, biosensing, cell labeling, and catalysis. For example, QD/G hybrids have been extensively applied in photoelectrochemical solar cells with the added values based on transparency and conductivity of G materials as compared to traditionally applied electrodes. Importantly, noncovalent attachment is beneficial to ensure enhanced phototransfer processes between QD and G surface. Despite many applications of QD/G(GO) hybrids in various fields, there are still just a few reported applications in biomedicine. Here, the hybrids of biocompatible carbon dots with GO would play the principal role in the future as proved by recent application of such a hybrid for selective labeling of cell cytoplasm. Finally, metals and metal oxides noncovalently attached onto G/GO surface are today very promising mainly in the field of catalysis, separable catalysts, and electrochemical applications. In these applications, the G/GO substrate helps to control the homogeneous distribution and size of nanoparticles with improved reaction yields, selectivity, or recyclability of the catalyst. However, the aspects of the nanocatalyst release and leaching into the environments should be carefully addressed.

AUTHOR INFORMATION

Corresponding Authors

*Tel.: +82-52-217-5410. Fax: +82-52-217-5419. E-mail: kimks@unist.ac.kr.

*Tel.: +420-58-563-4337. Fax: +420-58-563-4761. E-mail: radek.zboril@upol.cz.

Present Address

[†]Department of Environmental Engineering, Pohang University of Science and Technology (POSTECH), Pohang 37673, Korea.

Notes

The authors declare no competing financial interest.

Biographies

Vasilios Georgakilas received his B.Sc. and Ph.D. degrees in Chemistry and Organic Chemistry from the University of Ioannina (Greece) in 1989 and 1998, respectively. He then worked in the Institute of Material Science of N.C.S.R. “Demokritos”, Greece, and at the University of Trieste, Italy, as a Postdoctoral Fellow and Research Associate. He currently holds the position of Assistant Professor at the Material Science Department, University of Patras, Greece. His research interests lie in the synthesis and organic functionalization of nanostructured materials, with a particular emphasis on carbon nanomaterials and their applications.

Jitendra N. Tiwari received his Ph.D. degree in Electrochemistry from the Department of Materials Science and Engineering, National Chiao Tung University, Taiwan, in 2009, working on the synthesis of highly durable catalysts for electrochemical energy devices. He worked as postdoctoral research fellows at the Institute of Nanotechnology, National Chiao Tung University, Taiwan, and also at the Department of Chemistry, Pohang University of Science and Technology. Currently, he is a senior research scientist at the Department of Chemistry, Ulsan National Institute of Science and Technology (UNIST), and his work focuses on the development of graphene-based hybrid materials, and their applications in energy storage and conversion.

K. Christian Kemp received his Ph.D. in Chemistry at the Department of Chemistry, Pohang University of Science and Technology, under the guidance of Professor Kwang S. Kim. He is currently pursuing postdoctoral research at the Center for Ordered Nanoporous Materials Synthesis at Pohang University of Science and Technology. His interests include nanomaterials, catalysis, and organometallics for environmental applications.

In 2013, Jason A. Perman joined the Research Centre of Advanced Technologies and Materials at the Palacky University in Olomouc, Czech Republic, as a Junior Researcher. He was born in Tampa, FL, in 1983 and received his B.Sc. (2006) and Ph.D. (2011) degrees from the University of South Florida under the supervision of Professor Michael J. Zaworotko in the field of supramolecular chemistry. He was a postdoctoral associate with Professor Josef Michl from 2011–2013 at the Institute of Organic and Biochemistry, Academy of Science of the Czech Republic. His current research interests include supramolecular chemistry, green chemistry, Langmuir films, metal–organic materials, and materials based on graphene and graphene oxide.

Athanasios B. Bourlinos holds B.Sc. (1991–1995), M.Sc. (1997–1999), and Ph.D. (1999–2002) degrees in Chemistry from Athens University, Greece. He spent 2 years (2002–2004) as a postdoctoral fellow at the Materials Science & Engineering Department, Cornell University (Ithaca, NY), 6 years (2005–2011) as a research associate at the Institute of Materials Science, NCSR “Demokritos” (Athens, Greece), and 1 year (2011–2012) as a research associate at the Physics Department, University of Ioannina (Ioannina, Greece). He currently holds a position as Assistant Professor at the Physics Department, University of Ioannina. His research area focuses on the synthesis or surface modification, characterization, and properties of nanoscale materials with emphasis on carbon nanostructures.

Kwang S. Kim received his Ph.D. degree from University of California, Berkeley. He was a postdoctoral fellow at IBM and a visiting professor or scientist at Rutgers University, MIT, and Columbia University. He was a professor in the Department of Chemistry, Pohang University of Science and Technology. Currently, he is a distinguished professor in the Department of Chemistry and the director of the Center for Superfunctional Materials at Ulsan National Institute of Science and Technology (UNIST). His research interest includes molecular sensing, nanomaterials, and molecular devices.

Radek Zboril received his Ph.D. degree at the Palacky University in Olomouc, Czech Republic. After his doctoral studies, he spent a lot of time at universities around the world in locations such as Tokyo, Delaware, and Johannesburg. Currently, he is a professor at the Department of Physical Chemistry and a General Director of the Regional Centre of Advanced Technologies and Materials at the Palacky University in Olomouc, Czech Republic. His research interests focus on nanomaterial research including iron- and iron oxide-based nanoparticles, silver nanoparticles, carbon nanostructures, and magnetic nanoparticles, their synthesis, physicochemical characterization, and applications in catalysis, water treatment, antimicrobial treatment, medicine, and biotechnology.

ACKNOWLEDGMENTS

We acknowledge support from the Ministry of Education, Youth and Sports of the Czech Republic (LO1305). K.S.K. acknowledges the support from Korean NRF (National Honor Scientist Program: 2010-0020414).

REFERENCES

- (1) Novoselov, K. S.; Geim, A. K.; Morozov, S. V.; Jiang, D.; Zhang, Y.; Dubonos, S. V.; Grigorieva, I. V.; Firsov, A. A. Electric Field Effect in Atomically Thin Carbon Films. *Science* **2004**, *306*, 666–669.
- (2) Balandin, A. A.; Ghosh, S.; Bao, W.; Calizo, I.; Teweldebrhan, D.; Miao, F.; Lau, C. N. Superior Thermal Conductivity of Single-Layer Graphene. *Nano Lett.* **2008**, *8*, 902–907.
- (3) Lee, C.; Wei, X.; Kysar, J. W.; Hone, J. Measurement of the Elastic Properties and Intrinsic Strength of Monolayer Graphene. *Science* **2008**, *321*, 385–388.
- (4) Schafhaeutil, C. Ueber die Verbindungen des Kohlenstoffes mit Silicium, Eisen und anderen Metallen, welche die verschiedenen Gallungen von Roheisen, Stahl und Schmiedeeisen bilden. *J. Prakt. Chem.* **1840**, *21*, 129–157.
- (5) Bernal, J. D. The Structure of Graphite. *Proc. R. Soc. London, Ser. A* **1924**, *106*, 749–773.
- (6) Wallace, P. R. The Band Theory of Graphite. *Phys. Rev.* **1947**, *71*, 622–634.
- (7) Boehm, H. P.; Clauss, A.; Fisher, G. O.; Hofmann, U. Das Adsorptionsverhalten Sehr Dunner Kohlenstoff-Folien. *Z. Anorg. Allg. Chem.* **1962**, *316*, 119–127.
- (8) Boehm, H. P.; Clauss, A.; Hofmann, U.; Fisher, G. O. Dunnste Kohlenstoff-Folien. *Z. Naturforsch., B: J. Chem. Sci.* **1962**, *17*, 150.
- (9) Hofmann, U.; Frenzel, A. Die Reduktion von Graphitoxyd mit Schwefelwasserstoff. *Colloid Polym. Sci.* **1934**, *68*, 149–151.
- (10) Van Bommel, A. J.; Crombeen, J. E.; Vantooren, A. LEED and Auger-Electron Observation of SiC (0001) Surface. *Surf. Sci.* **1975**, *48*, 463–472.
- (11) Foster, L. M.; Long, G.; Stumpf, H. C. Production of Graphite Single Crystals by the Thermal Decomposition of Aluminium Carbide. *Am. Mineral.* **1958**, *43*, 285–296.
- (12) Land, T. A.; Michely, T.; Behm, R. J.; Hemminger, J. C.; Comsa, G. STM Investigation of Single Layer Graphite Structures Produced on Pt(111) by Hydrocarbon Decomposition. *Surf. Sci.* **1992**, *264*, 261–270.
- (13) Forbeaux, I.; Themlin, J. M.; Debever, J. M. Heteroepitaxial Graphite on 6H-SiC(0001): Interface Formation Through Conduction-Band Electronic Structure. *Phys. Rev. B: Condens. Matter Mater. Phys.* **1998**, *58*, 16396–16406.
- (14) Grima, J. N.; Winczewski, S.; Mizzi, L.; Grech, M. C.; Cauchi, R.; Gatt, R.; Attard, D.; Wojciechowski, K. W.; Rybicki, J. Tailoring Graphene to Achieve Negative Poisson's Ratio Properties. *Adv. Mater.* **2015**, *27*, 1455–1459.
- (15) Kroto, H. W.; Heath, J. R.; O'Brien, S. C.; Curl, R. F.; Smalley, R. E. C₆₀ – Buckminsterfullerene. *Nature* **1985**, *318*, 162–163.
- (16) Iijima, S.; Yudasaka, M.; Yamada, R.; Bandow, S.; Suenaga, K.; Kokai, F.; Takahashi, K. Nano-Aggregates of Single-Walled Graphitic Carbon Nano-Horns. *Chem. Phys. Lett.* **1999**, *309*, 165–170.
- (17) Iijima, S. Helical Microtubules of Graphitic Carbon. *Nature* **1991**, *354*, 56–58.
- (18) Iijima, S.; Ichihashi, T. Single-Shell Carbon Nanotubes of 1-nm Diameter. *Nature* **1993**, *363*, 603–605.
- (19) Bethune, D. S.; Kiang, C. H.; de Vries, M. S.; Gorman, G.; Savoy, R.; Vazquez, J.; Beyers, R. Cobalt-Catalyzed Growth of Carbon Nanotubes with Single-Atomic-Layerwalls. *Nature* **1993**, *363*, 605–607.
- (20) Geim, A. K.; Novoselov, K. S. The Rise of Graphene. *Nat. Mater.* **2007**, *6*, 183–191.
- (21) Bolotin, K. I.; Sikes, K. J.; Jiang, Z.; Klima, M.; Fudenberg, G.; Hone, J.; Kim, P.; Stormer, H. L. Ultrahigh Electron Mobility in Suspended Graphene. *Solid State Commun.* **2008**, *146*, 351–355.
- (22) Abergel, D. S. L.; Apalkov, V.; Berashevich, J.; Ziegler, K.; Chakraborty, T. Properties of Graphene: a Theoretical Perspective. *Adv. Phys.* **2010**, *59*, 261–482.
- (23) Zhang, Z. Z.; Chang, K. Tuning of Energy Levels and Optical Properties of Graphene Quantum Dots. *Phys. Rev. B: Condens. Matter Mater. Phys.* **2008**, *77*, 235411.
- (24) Nakada, K.; Fujita, M.; Dresselhaus, G.; Dresselhaus, M. S. Edge State in Graphene Ribbons: Nanometer Size Effect and Edge Shape Dependence. *Phys. Rev. B: Condens. Matter Mater. Phys.* **1996**, *54*, 17954–17961.

- (25) Kim, W. Y.; Kim, K. S. Prediction of Very Large Values of Magnetoresistance in a Graphene Nanoribbon Device. *Nat. Nanotechnol.* **2008**, *3*, 408–412.
- (26) Nair, R. R.; Blake, P.; Grigorenko, A. N.; Novoselov, K. S.; Booth, T. J.; Stauber, T.; Peres, N. M. R.; Geim, A. K. Fine Structure Constant Defines Visual Transparency of Graphene. *Science* **2008**, *320*, 1308.
- (27) Staudenmaier, L. Verfahren zur Darstellung der Graphitsäure. *Ber. Dtsch. Chem. Ges.* **1898**, *31*, 1481–1487.
- (28) Hummers, W. S.; Offeman, R. E. Preparation of Graphitic Oxide. *J. Am. Chem. Soc.* **1958**, *80*, 1339.
- (29) Marcano, D. C.; Kosynkin, D. V.; Berlin, J. M.; Sinitskii, A.; Sun, Z. Z.; Slesarev, A.; Alemany, L. B.; Lu, W.; Tour, J. M. Improved Synthesis of Graphene Oxide. *ACS Nano* **2010**, *4*, 4806–4814.
- (30) Dryer, D. R.; Park, S.; Bielawski, C. W.; Ruoff, R. S. The Chemistry of Graphene Oxide. *Chem. Soc. Rev.* **2010**, *39*, 229–240.
- (31) Hofmann, U.; König, E. Untersuchungen über Graphitoxyd. *Z. Anorg. Allg. Chem.* **1937**, *234*, 311–336.
- (32) Fisher, E. Einfluss der Configuration auf die Wirkung der Enzyme. *Ber. Dtsch. Chem. Ges.* **1894**, *27*, 2985–2993.
- (33) Lehn, J. M. *Supramolecular Chemistry: Concepts and Perspectives*; Wiley: New York, 1995.
- (34) McMurry, J.; Fayl McCarty, R. C. *Chemistry*; Pearson Education: New York, 2004.
- (35) Lide, D. R. *CRC Handbook of Chemistry and Physics*, 85th ed.; Taylor & Francis: New York, 2004.
- (36) Atkins, P.; de Paula, J. *Physical Chemistry*, 7th ed.; W. H. Freeman: New York, 2002.
- (37) Steed, J. W.; Atwood, J. L. *Supramolecular Chemistry*, 2nd ed.; Wiley: New York, 2013.
- (38) Skinner, H. A.; Connor, J. A. Metal-Ligand Bond-Energies in Organometallic Compounds. *Pure Appl. Chem.* **1985**, *57*, 79–88.
- (39) Smithrud, D. B.; Sanford, E. M.; Chao, I.; Ferguson, S. B.; Carcanague, D. R.; Evansek, J. D.; Houk, K. N.; Diederich, F. Solvent Effects in Molecular Recognition. *Pure Appl. Chem.* **1990**, *62*, 2227–2236.
- (40) Southall, N. T.; Dill, K. A.; Haymet, A. D. J. A View of the Hydrophobic Effect. *J. Phys. Chem. B* **2002**, *106*, 521–533.
- (41) Hunter, C. A.; Lawson, K. R.; Perkins, C.; Urch, C. J. Aromatic Interactions. *J. Chem. Soc. Perkin. T.* **2001**, *2*, 651–669.
- (42) Zhang, Z. X.; Huang, H. L.; Yang, X. M.; Zang, L. Tailoring Electronic Properties of Graphene by pi-pi Stacking with Aromatic Molecules. *J. Phys. Chem. Lett.* **2011**, *2*, 2897–2905.
- (43) Kozlov, S. M.; Vines, F.; Gorling, A. On the Interaction of Polycyclic Aromatic Compounds with Graphene. *Carbon* **2012**, *50*, 2482–2492.
- (44) De Feyter, S.; De Schryver, F. C. Two-Dimensional Supramolecular Self-Assembly Probed by Scanning Tunneling Microscopy. *Chem. Soc. Rev.* **2003**, *32*, 139–150.
- (45) Foster, J. S.; Frommer, J. E. Imaging of Liquid-Crystals Using a Tunnelling Microscope. *Nature* **1988**, *333*, 542–545.
- (46) Griessl, S.; Lackinger, M.; Edelwirth, M.; Hietschold, M.; Heckl, W. M. Self-Assembled Two-Dimensional Molecular Host-Guest Architectures from Trimesic Acid. *Single Mol.* **2002**, *3*, 25–31.
- (47) Lackinger, M.; Griessl, S.; Heckl, W. M.; Hietschold, M. STM and STS of Coronene on HOPG(0001) in UHV – Adsorption of the Smallest Possible Graphite Flakes on Graphite. *Anal. Bioanal. Chem.* **2002**, *374*, 685–687.
- (48) Shayeganfar, F.; Rochefort, A. Electronic Properties of Self-Assembled Trimesic Acid Monolayer on Graphene. *Langmuir* **2014**, *30*, 9707–9716.
- (49) Zhou, Q.; Li, Y.; Li, Q.; Wang, Y.; Yang, Y.; Fang, Y.; Wang, C. Switchable Supramolecular Assemblies on Graphene. *Nanoscale* **2014**, *6*, 8387–8391.
- (50) MacLeod, J. M.; Lipton-Duffin, J. A.; Cui, D.; De Feyter, S.; Rosei, F. Substrate Effects in the Supramolecular Assembly of 1,3,5-Benzene Tricarboxylic Acid on Graphite and Graphene. *Langmuir* **2015**, *31*, 7016–7024.
- (51) Chen, W.; Chen, S.; Qi, D. C.; Gao, X. Y.; Wee, A. T. S. Surface Transfer p-Type Doping of Epitaxial Graphene. *J. Am. Chem. Soc.* **2007**, *129*, 10418–10422.
- (52) Coletti, C.; Riedl, C.; Lee, D. S.; Krauss, B.; Patthey, L.; von Klitzing, K.; Smet, J. H.; Starke, U. Charge Neutrality and Band-Gap Tuning of Epitaxial Graphene on SiC by Molecular Doping. *Phys. Rev. B: Condens. Matter Mater. Phys.* **2010**, *81*, 235401.
- (53) Stradi, D.; Garnica, M.; Diaz, C.; Calleja, F.; Barja, S.; Martin, N.; Alcamí, M.; de Parga, A. L. V.; Miranda, R.; Martin, F. Controlling the Spatial Arrangement of Organic Magnetic Anions Adsorbed on Epitaxial Graphene on Ru(0001). *Nanoscale* **2014**, *6*, 15271–15279.
- (54) Huang, H.; Chen, S.; Gao, X.; Chen, W.; Wee, A. T. S. Structural and Electronic Properties of PTCDA Thin Films on Epitaxial Graphene. *ACS Nano* **2009**, *3*, 3431–3436.
- (55) Lauffer, P.; Emtsev, K. V.; Graupner, R.; Seyller, T.; Ley, L. Molecular and Electronic Structure of PTCDA on Bilayer Graphene on SiC(0001) Studied with Scanning Tunneling Microscopy. *Phys. Status Solidi B* **2008**, *245*, 2064–2067.
- (56) Wang, Q. H.; Hersam, M. C. Room-Temperature Molecular-Resolution Characterization of Self-Assembled Organic Monolayers on Epitaxial Graphene. *Nat. Chem.* **2009**, *1*, 206–211.
- (57) Emery, J. D.; Wang, Q. H.; Zarrouati, M.; Fenter, P.; Hersam, M. C.; Bedzyk, M. J. Structural Analysis of PTCDA Monolayers on Epitaxial Graphene with Ultra-High Vacuum Scanning Tunneling Microscopy and High-Resolution X-ray Reflectivity. *Surf. Sci.* **2011**, *605*, 1685–1693.
- (58) Pollard, A. J.; Perkins, E. W.; Smith, N. A.; Saywell, A.; Goretzki, G.; Phillips, A. G.; Argent, S. P.; Sachdev, H.; Mueller, F.; Huefner, S.; et al. Supramolecular Assemblies Formed on an Epitaxial Graphene Superstructure. *Angew. Chem., Int. Ed.* **2010**, *49*, 1794–1799.
- (59) Karmel, H. J.; Garramone, J. J.; Emery, J. D.; Kewalramani, S.; Bedzyk, M. J.; Hersam, M. C. Self-Assembled Organic Monolayers on Epitaxial Graphene with Enhanced Structural and Thermal Stability. *Chem. Commun.* **2014**, *50*, 8852–8855.
- (60) Kozlov, S. M.; Vines, F.; Gorling, A. Bandgap Engineering of Graphene by Physisorbed Adsorbates. *Adv. Mater.* **2011**, *23*, 2638–2643.
- (61) Zhang, L. M.; Yu, J. W.; Yang, M. M.; Xie, Q.; Peng, H. L.; Liu, Z. F. Janus Graphene from Asymmetric Two-Dimensional Chemistry. *Nat. Commun.* **2013**, *4*, 1443.
- (62) Hernandez, Y.; Nicolosi, V.; Lotya, M.; Blighe, F. M.; Sun, Z.; De, S.; McGovern, I. T.; Holland, B.; Byrne, M.; Gun'Ko, Y. K.; et al. High-Yield Production of Graphene by Liquid-Phase Exfoliation of Graphite. *Nat. Nanotechnol.* **2008**, *3*, 563–568.
- (63) Pykal, M.; Safarova, K.; Siskova, K. M.; Jurecka, P.; Bourlinos, A. B.; Zboril, R.; Otyepka, M. Lipid Enhanced Exfoliation for Production of Graphene Nanosheets. *J. Phys. Chem. C* **2013**, *117*, 11800–11803.
- (64) Hernandez, Y.; Lotya, M.; Rickard, D.; Bergin, S. D.; Coleman, J. N. Measurement of Multicomponent Solubility Parameters for Graphene Facilitates Solvent Discovery. *Langmuir* **2010**, *26*, 3208–3213.
- (65) Khan, U.; O'Neill, A.; Lotya, M.; De, S.; Coleman, J. N. High-Concentration Solvent Exfoliation of Graphene. *Small* **2010**, *6*, 864–871.
- (66) O'Neill, A.; Khan, U.; Nirmalraj, P. N.; Boland, J.; Coleman, J. N. Graphene Dispersion and Exfoliation in Low Boiling Point Solvents. *J. Phys. Chem. C* **2011**, *115*, 5422–5428.
- (67) Coleman, J. N. Liquid Exfoliation of Defect-Free Graphene. *Acc. Chem. Res.* **2013**, *46*, 14–22.
- (68) Hughes, J. M.; Ahrene, D.; Coleman, J. N. Generalizing Solubility Parameter Theory to Apply to One- and Two-Dimensional Solutes and to Incorporate Dipolar Interactions. *J. Appl. Polym. Sci.* **2013**, *127*, 4483–4491.
- (69) Nicolosi, V.; Chhowalla, M.; Kanatzidis, M. G.; Strano, M. S.; Coleman, J. N. Liquid Exfoliation of Layered Materials. *Science* **2013**, *340*, 1226419.
- (70) Wang, S.; Zhang, Y.; Abidi, N.; Cabrales, L. Wettability and Surface Free Energy of Graphene Films. *Langmuir* **2009**, *25*, 11078–11081.

- (71) Hansen, C. M. *Hansen Solubility Parameters: A User's Handbook*, 2nd ed.; CRC Press: New York, 2007.
- (72) Hansen, C. M. *The Three Dimensional Solubility Parameter and Solvent Diffusion Coefficient: Their Importance in Surface Coating Formulation*; Danish Technical Press, 1967.
- (73) Hildebrand, J. H.; Prausnitz, J. M.; Scott, R. L. *Regular and Related Solutions: the Solubility of Gases, Liquids, and Solids*; van Nostrand Reinhold Co.: New York, 1970.
- (74) Zhang, Y. H.; Liu, C. J.; Shi, W. Q.; Wang, Z. Q.; Dai, L. M.; Zhang, X. Direct Measurements of the Interaction between Pyrene and Graphite in Aqueous Media by Single Molecule Force Spectroscopy: Understanding the π - π Interactions. *Langmuir* **2007**, *23*, 7911–7915.
- (75) Manohar, S.; Mantz, A. R.; Bancroft, K. E.; Hui, C. Y.; Jagota, A.; Vezhenov, D. V. Peeling Single-Stranded DNA from Graphite Surface to Determine Oligonucleotide Binding Energy by Force Spectroscopy. *Nano Lett.* **2008**, *8*, 4365–4372.
- (76) Georgakilas, V.; Otyepka, M.; Bourlinos, A. B.; Chandra, V.; Kim, N.; Kemp, K. C.; Hobza, P.; Zboril, R.; Kim, K. S. Functionalization of Graphene: Covalent and Non-Covalent Approaches, Derivatives and Applications. *Chem. Rev.* **2012**, *112*, 6156–6214.
- (77) Lee, E. C.; Kim, D.; Jurečka, P.; Tarakeshwar, P.; Hobza, P.; Kim, K. S. Understanding of Assembly Phenomena by Aromatic-Aromatic Interactions: Benzene Dimer and the Substituted Systems. *J. Phys. Chem. A* **2007**, *111*, 3446–3457.
- (78) Su, Q.; Pang, S.; Alijani, V.; Li, C.; Feng, X.; Muellen, K. Composites of Graphene with Large Aromatic Molecules. *Adv. Mater.* **2009**, *21*, 3191–3195.
- (79) Zhang, X. F.; Liu, S. P.; Shao, X. N. Noncovalent Binding of Xanthene and Phthalocyanine Dyes with Graphene Sheets: The Effect of the Molecular Structure Revealed by a Photophysical Study. *Spectrochim. Acta, Part A* **2013**, *113*, 92–99.
- (80) Yang, X.; Li, J.; Wen, T.; Ren, X.; Huang, Y.; Wang, X. Adsorption of Naphthalene and Its Derivatives on Magnetic Graphene Composites and the Mechanism Investigation. *Colloids Surf., A* **2013**, *422*, 118–125.
- (81) Zhang, X. F.; Shao, X. Binding Ability of Different Carbon Nano-Materials with Aromatic Phthalocyanine Molecules: Comparison between Graphene and Graphene Oxide. *J. Photochem. Photobiol., A* **2014**, *278*, 69–74.
- (82) Wang, J.; Chen, Z.; Chen, B. Adsorption of Polycyclic Aromatic Hydrocarbons by Graphene and Graphene Oxide Nanosheets. *Environ. Sci. Technol.* **2014**, *48*, 4817–4825.
- (83) Chen, I. W. P.; Huang, C. Y.; Jhou, S. H. S.; Zhang, Y. W. Exfoliation and Performance Properties of Non-Oxidized Graphene in Water. *Sci. Rep.* **2014**, *4*, 3928.
- (84) Bourlinos, A. B.; Georgakilas, V.; Zboril, R.; Steriotis, T. A.; Stubos, A. K. Liquid-Phase Exfoliation of Graphite towards Solubilized Graphenes. *Small* **2009**, *5*, 1841–1845.
- (85) Kim, J.; Song, S. H.; Im, H. G.; Yoon, G.; Lee, D.; Choi, C.; Kim, J.; Bae, B. S.; Kang, K.; Jeon, S. Moisture Barrier Composites Made of Non-Oxidized Graphene Flakes. *Small* **2015**, *11*, 3124–3129.
- (86) Lee, D. W.; Kim, T.; Lee, M. An Amphiphilic Pyrene Sheet for Selective Functionalization of Graphene. *Chem. Commun.* **2011**, *47*, 8259–8261.
- (87) Yang, H.; Hernandez, Y.; Schlierf, A.; Felten, A.; Eckmann, A.; Johal, S.; Louette, P.; Pireaux, J. J.; Feng, X.; Muellen, K.; et al. A Simple Method for Graphene Production Based on Exfoliation of Graphite in Water Using 1-Pyrenesulfonic Acid Sodium Salt. *Carbon* **2013**, *53*, 357–365.
- (88) Jang, J. H.; Rangappa, D.; Kwon, Y. U.; Honma, I. Direct Preparation of 1-PSA Modified Graphene Nanosheets by Supercritical Fluidic Exfoliation and Its Electrochemical Properties. *J. Mater. Chem.* **2011**, *21*, 3462–3466.
- (89) An, X. H.; Simmons, T. J.; Shah, R.; Wolfe, C.; Lewis, K. M.; Washington, M.; Nayak, S. K.; Talapatra, S.; Kar, S. Stable Aqueous Dispersions of Noncovalently Functionalized Graphene from Graphite and their Multifunctional High-Performance Applications. *Nano Lett.* **2010**, *10*, 4295–4301.
- (90) Dong, X. C.; Shi, Y. M.; Zhao, Y.; Chen, D. M.; Ye, J.; Yao, Y. G.; Gao, F.; Ni, Z. H.; Yu, T.; Shen, Z. X.; et al. Symmetry Breaking of Graphene Monolayers by Molecular Decoration. *Phys. Rev. Lett.* **2009**, *102*, 135501.
- (91) Zhang, M.; Parajuli, R. R.; Mastrogiovanni, D.; Dai, B.; Lo, P.; Cheung, W.; Brukh, R.; Chiu, P. L.; Zhou, T.; Liu, Z. F.; et al. Production of Graphene Sheets by Direct Dispersion with Aromatic Healing Agents. *Small* **2010**, *6*, 1100–1107.
- (92) Schlierf, A.; Yang, H.; Gebremedhn, E.; Treossi, E.; Ortolani, L.; Chen, L.; Minoia, A.; Morandi, V.; Samori, P.; Casiraghi, C.; et al. Nanoscale Insight into the Exfoliation Mechanism of Graphene with Organic Dyes: Effect of Charge, Dipole and Molecular Structure. *Nanoscale* **2013**, *5*, 4205–4216.
- (93) Song, S. H.; Park, K. H.; Kim, B. H.; Choi, Y. W.; Jun, G. H.; Lee, D. J.; Kong, B. S.; Paik, K. W.; Jeon, S. Enhanced Thermal Conductivity of Epoxy–Graphene Composites by Using Non-Oxidized Graphene Flakes with Non-Covalent Functionalization. *Adv. Mater.* **2013**, *25*, 732–737.
- (94) Khanra, P.; Uddin, M. E.; Kim, N. H.; Kuila, T.; Lee, S. H.; Lee, J. H. Electrochemical Performance of Reduced Graphene Oxide Surface-Modified with 9-Anthracene Carboxylic Acid. *RSC Adv.* **2015**, *5*, 6443–6451.
- (95) Bose, S.; Kuila, T.; Mishra, A. K.; Kim, N. H.; Lee, J. H. Preparation of Non-Covalently Functionalized Graphene Using 9-Anthracene Carboxylic Acid. *Nanotechnology* **2011**, *22*, 405603.
- (96) Das, S.; Irin, F.; Ahmed, H. S. T.; Cortinas, A. B.; Wajid, A. S.; Parviz, D.; Jankowski, A. F.; Kato, M.; Green, M. J. Non-Covalent Functionalization of Pristine Few-Layer Graphene Using Triphenylene Derivatives for Conductive Poly (Vinyl Alcohol) Composites. *Polymer* **2012**, *53*, 2485–2494.
- (97) Ghosh, A.; Rao, K. V.; George, S. J.; Rao, C. N. R. Noncovalent Functionalization, Exfoliation, and Solubilization of Graphene in Water by Employing a Fluorescent Coronene Carboxylate. *Chem. - Eur. J.* **2010**, *16*, 2700–2704.
- (98) Ma, W. S.; Wu, L.; Yang, F.; Wang, S. F. Non-Covalently Modified Reduced Graphene Oxide/Polyurethane Nanocomposites with Good Mechanical and Thermal Properties. *J. Mater. Sci.* **2014**, *49*, S62–S71.
- (99) Lonkar, S. P.; Bobenrieth, A.; De Winter, J.; Gerbaux, P.; Raquez, J. M.; Dubois, P. A Supramolecular Approach toward Organo-Dispersible Graphene and Its Straightforward Polymer Nanocomposites. *J. Mater. Chem.* **2012**, *22*, 18124–18126.
- (100) Yang, Y. K.; He, C. E.; Peng, R. G.; Baji, A.; Du, X. S.; Huang, Y. L.; Xie, X. L.; Mai, Y. W. Non-Covalently Modified Graphene Sheets by Imidazolium Ionic Liquids for Multifunctional Polymer Nanocomposites. *J. Mater. Chem.* **2012**, *22*, S666–S675.
- (101) Bari, R.; Tamas, G.; Irin, F.; Aquino, A. J. A.; Green, M. J.; Quitevis, E. L. Direct Exfoliation of Graphene in Ionic Liquids with Aromatic Groups. *Colloids Surf., A* **2014**, *463*, 63–69.
- (102) Zhang, B.; Ning, W.; Zhang, J.; Qiao, X.; Zhang, J.; He, J.; Liu, C. Y. Stable Dispersions of Reduced Graphene Oxide in Ionic Liquids. *J. Mater. Chem.* **2010**, *20*, S401–S403.
- (103) Kim, T. Y.; Lee, H. W.; Kim, J. E.; Suh, K. S. Synthesis of Phase Transferable Graphene Sheets Using Ionic Liquid Polymers. *ACS Nano* **2010**, *4*, 1612–1618.
- (104) Geng, J.; Jung, H. T. Porphyrin Functionalized Graphene Sheets in Aqueous Suspensions: From the Preparation of Graphene Sheets to Highly Conductive Graphene Films. *J. Phys. Chem. C* **2010**, *114*, 8227–8234.
- (105) Xu, Y.; Zhao, L.; Bai, H.; Hong, W.; Li, C.; Shi, G. Chemically Converted Graphene Induced Molecular Flattening of 5,10,15,20-Tetrakis(1-methyl-4-pyridinio)porphyrin and Its Application for Optical Detection of Cadmium(II) Ions. *J. Am. Chem. Soc.* **2009**, *131*, 13490–13497.
- (106) Arramel, A.; Castellanos-Gomez, B.; van Wees, J. Band Gap Opening of Graphene by Noncovalent π - π Interaction with Porphyrins. *Graphene* **2013**, *2*, 102–108.
- (107) Bozkurt, E.; Acar, M.; Onganer, Y.; Meral, K. Rhodamine 101-Graphene Oxide Composites in Aqueous Solution: the Fluorescence Quenching Process of Rhodamine 101. *Phys. Chem. Chem. Phys.* **2014**, *16*, 18276–18281.

- (108) Jiang, B. P.; Hu, L. F.; Wang, D. J.; Ji, S. C.; Shen, X. C.; Liang, H. Graphene Loading Water-Soluble Phthalocyanine for Dual-Modality Photothermal/Photodynamic Therapy via a One-Step Method. *J. Mater. Chem. B* **2014**, *2*, 7141–7148.
- (109) Chien, C. T.; Li, S. S.; Lai, W. J.; Yeh, Y. C.; Chen, H. A.; Chen, I. S.; Chen, L. C.; Chen, K. H.; Nemoto, T.; Isoda, S.; et al. Tunable Photoluminescence from Graphene Oxide. *Angew. Chem., Int. Ed.* **2012**, *51*, 6662–6666.
- (110) Zhang, X. F.; Shao, X.; Liu, S. Dual Fluorescence of Graphene Oxide: A Time-Resolved Study. *J. Phys. Chem. A* **2012**, *116*, 7308–7313.
- (111) Loh, K. P.; Bao, Q. L.; Eda, G.; Chhowalla, M. Graphene Oxide as a Chemically Tunable Platform for Optical Applications. *Nat. Chem.* **2010**, *2*, 1015–1024.
- (112) Iliut, M.; Gabudean, A. M.; Leordean, C.; Simon, T.; Teodorescu, C. M.; Astilean, S. Riboflavin Enhanced Fluorescence of Highly Reduced Graphene Oxide. *Chem. Phys. Lett.* **2013**, *586*, 127–131.
- (113) Fernandez-Merino, M. J.; Paredes, J. I.; Villar-Rodil, S.; Guardia, L.; Solis-Fernandez, P.; Salinas-Torres, D.; Cazorla-Amoros, D.; Morallon, E.; Martinez-Alonso, A.; Tascon, J. M. D. Investigating the Influence of Surfactants on the Stabilization of Aqueous Reduced Graphene Oxide Dispersions and the Characteristics of Their Composite Films. *Carbon* **2012**, *50*, 3184–3194.
- (114) Bourlino, A. B.; Georgakilas, V.; Zboril, R.; Steriotis, T. A.; Stubos, A. K.; Trapalis, C. Aqueous-Phase Exfoliation of Graphite in the Presence of Polyvinylpyrrolidone for the Production of Water-Soluble Graphenes. *Solid State Commun.* **2009**, *149*, 2172–2176.
- (115) Liang, Y.; Wu, D.; Feng, X.; Mullen, K. Dispersion of Graphene Sheets in Organic Solvent Supported by Ionic Interactions. *Adv. Mater.* **2009**, *21*, 1–5.
- (116) Carrasco, P. M.; Montes, S.; Garcia, I.; Borghei, M.; Jiang, H.; Odriozola, L.; Cabanero, G.; Ruiz, V. High-Concentration Aqueous Dispersions of Graphene Produced by Exfoliation of Graphite Using Cellulose Nanocrystals. *Carbon* **2014**, *70*, 157–163.
- (117) Lotya, M.; King, P. J.; Khan, U.; De, S.; Coleman, J. N. High-Concentration, Surfactant-Stabilized Graphene Dispersions. *ACS Nano* **2010**, *4*, 3155–3162.
- (118) Lotya, M.; Hernandez, Y.; King, P. J.; Smith, R. J.; Nicolosi, V.; Karlsson, L. S.; Blighe, F. M.; De, S.; Wang, Z.; McGovern, I. T. Liquid Phase Production of Graphene by Exfoliation of Graphite in Surfactant/Water Solutions. *J. Am. Chem. Soc.* **2009**, *131*, 3611–3620.
- (119) Cai, M.; Thorpe, D.; Adamson, D. H.; Schniepp, H. C. Methods of Graphite Exfoliation. *J. Mater. Chem.* **2012**, *22*, 24992–25002.
- (120) Yang, Q.; Pan, X.; Huang, F.; Li, K. Fabrication of High-Concentration and Stable Aqueous Suspensions of Graphene Nanosheets by Noncovalent Functionalization with Lignin and Cellulose Derivatives. *J. Phys. Chem. C* **2010**, *114*, 3811–3816.
- (121) Choi, E. Y.; Han, T. H.; Hong, J.; Kim, J. E.; Lee, S. H.; Kim, H. W.; Kim, S. O. Noncovalent Functionalization of Graphene with End-Functional Polymers. *J. Mater. Chem.* **2010**, *20*, 1907–1912.
- (122) Lian, M.; Fan, J.; Shi, Z.; Li, H.; Yin, J. Kevlar-Functionalized Graphene Nanoribbon for Polymer Reinforcement. *Polymer* **2014**, *55*, 2578–2587.
- (123) Zhang, J.; Xu, Y.; Cui, L.; Fu, A.; Yang, W.; Barrow, C.; Liu, J. Mechanical Properties of Graphene Films Enhanced by Homo-Telechelic Functionalized Polymer Fillers via π - π Stacking Interactions. *Composites, Part A* **2015**, *71*, 1–8.
- (124) Chandra, V.; Kim, K. S. Highly Selective Adsorption of Hg^{2+} by Polypyrrole-Reduced Graphene Oxide Composite. *Chem. Commun.* **2011**, *47*, 3942–3944.
- (125) Stankovich, S.; Piner, R. D.; Chen, X.; Wu, N.; Nguyen, S. T.; Ruoff, R. S. Stable Aqueous Dispersions of Graphitic Nanoplatelets via the Reduction of Exfoliated Graphite Oxide in the Presence of Poly(sodium 4-styrenesulfonate). *J. Mater. Chem.* **2006**, *16*, 155–158.
- (126) Bai, H.; Xu, Y.; Zhao, L.; Li, C.; Shi, G. Non-Covalent Functionalization of Graphene Sheets by Sulfonated Polyaniline. *Chem. Commun.* **2009**, 1667–1669.
- (127) Matos, C. F.; Galembeck, F.; Zarbin, A. J. G. Multifunctional and Environmentally Friendly Nanocomposites between Natural Rubber and Graphene or Graphene Oxide. *Carbon* **2014**, *78*, 469–479.
- (128) Hsiao, S. T.; Ma, C. C. M.; Tien, H. W.; Liao, W. H.; Wang, Y. S.; Li, S. M.; Huang, Y. C. Using a Non-Covalent Modification to Prepare a High Electromagnetic Interference Shielding Performance Graphene Nanosheet/Water-Borne Polyurethane Composite. *Carbon* **2013**, *60*, 57–66.
- (129) Lee, D. Y.; Khatun, Z.; Lee, J. H.; Lee, Y.; In, I. Blood Compatible Graphene/Heparin Conjugate through Noncovalent Chemistry. *Biomacromolecules* **2011**, *12*, 336–341.
- (130) Zhang, Y.; Zhang, J.; Huang, X.; Zhou, X.; Wu, H.; Guo, S. Assembly of Graphene Oxide–Enzyme Conjugates through Hydrophobic Interaction. *Small* **2012**, *8*, 154–159.
- (131) Zhang, J.; Zhang, F.; Yang, H.; Huang, X.; Liu, H.; Zhang, J.; Guo, S. Graphene Oxide as a Matrix for Enzyme Immobilization. *Langmuir* **2010**, *26*, 6083–6085.
- (132) Alwarappan, S.; Boyapalle, S.; Kumar, A.; Li, C. Z.; Mohapatra, S. Comparative Study of Single-, Few-, and Multilayered Graphene toward Enzyme Conjugation and Electrochemical Response. *J. Phys. Chem. C* **2012**, *116*, 6556–6559.
- (133) Heien, M. L. A. V.; Khan, A. S.; Ariansen, J. L.; Cheer, J. F.; Phillips, P. E. M.; Wassum, K. M.; Wightman, R. M. *Proc. Natl. Acad. Sci. U. S. A.* **2005**, *102*, 10023–10028.
- (134) Wang, Y.; Li, Y.; Tang, L.; Lu, J.; Li, J. Application of Graphene-Modified Electrode for Selective Detection of Dopamine. *Electrochem. Commun.* **2009**, *11*, 889–892.
- (135) Kim, Y. R.; Bong, S.; Kang, Y. J.; Yang, Y.; Mahajan, R. K.; Kim, J. S.; Kim, H. Electrochemical Detection of Dopamine in the Presence of Ascorbic Acid Using Graphene Modified Electrodes. *Biosens. Bioelectron.* **2010**, *25*, 2366–2369.
- (136) Lian, Q.; He, Z.; He, Q.; Luo, A.; Yan, K.; Zhang, D.; Lu, X.; Zhou, X. Simultaneous Determination of Ascorbic Acid, Dopamine and Uric Acid Based on Tryptophan Functionalized Graphene. *Anal. Chim. Acta* **2014**, *823*, 32–39.
- (137) Zhang, W.; Chai, Y.; Yuan, R.; Chen, S.; Han, J.; Yuan, D. Facile Synthesis of Graphene Hybrid Tube-Like Structure for Simultaneous Detection of Ascorbic Acid, Dopamine, Uric Acid and Tryptophan. *Anal. Chim. Acta* **2012**, *756*, 7–12.
- (138) Lv, M.; Mei, T.; Zhang, C.; Wang, X. Selective and Sensitive Electrochemical Detection of Dopamine Based on Water-Soluble Porphyrin Functionalized Graphene Nanocomposites. *RSC Adv.* **2014**, *4*, 9261–9270.
- (139) Zhang, Y.; Xia, Z.; Liu, H.; Yang, M.; Lin, L.; Li, Q. Hemin Graphene Oxide-Pristine Carbon Nanotubes Complexes with Intrinsic Peroxidase-Like Activity for the Detection of H_2O_2 and Simultaneous Determination for Trp, AA, DA, and UA. *Sens. Actuators, B* **2013**, *188*, 496–501.
- (140) Pandikumar, A.; Thien Soon How, G.; See, T. P.; Omar, F. S.; Jayabal, S.; Zangeneh Kamali, K.; Yusoff, N.; Jamil, A.; Ramaraj, R.; Abraham John, S.; et al. Graphene and Its Nanocomposite Material Based Electrochemical Sensor Platform for Dopamine. *RSC Adv.* **2014**, *4*, 63296–63323.
- (141) Min, S. K.; Kim, W. Y.; Cho, Y.; Kim, K. S. Fast DNA Sequencing with a Graphene-Based Nanochannel Device. *Nat. Nanotechnol.* **2011**, *6*, 162–165.
- (142) Zhu, C.; Du, D.; Lin, Y. Graphene and Graphene-Like 2D Materials for Optical Biosensing and Bioimaging: A Review. *2D Mater.* **2015**, *2*, 032004.
- (143) Liu, Y.; Dong, X.; Chen, P. Biological and Chemical Sensors Based on Graphene Materials. *Chem. Soc. Rev.* **2012**, *41*, 2283–2307.
- (144) Green, N. S.; Norton, M. L. Interactions of DNA with graphene and sensing applications of graphene field-effect transistor devices: A review. *Anal. Chim. Acta* **2015**, *853*, 127–142.
- (145) Lu, C. H.; Yang, H. H.; Zhu, C. L.; Chen, X.; Chen, G. N. A Graphene Platform for Sensing Biomolecules. *Angew. Chem., Int. Ed.* **2009**, *48*, 4785–4787.
- (146) Bonanni, A.; Pumera, M. Graphene Platform for Hairpin-DNA Based Impedimetric Genosensing. *ACS Nano* **2011**, *5*, 2356–2361.

- (147) Loo, A. H.; Bonanni, A.; Pumera, M. An Insight into the Hybridization Mechanism of Hairpin DNA Physically Immobilized on Chemically Modified Graphenes. *Analyst* **2013**, *138*, 467–471.
- (148) Giovanni, M.; Bonanni, A.; Pumera, M. Detection of DNA Hybridization on Chemically Modified Graphene Platforms. *Analyst* **2012**, *137*, 580–583.
- (149) Loo, A. H.; Bonanni, A.; Ambrosi, A.; Poh, H. L.; Pumera, M. Impedimetric Immunoglobulin G Immunosensor Based on Chemically Modified Graphenes. *Nanoscale* **2012**, *4*, 921–925.
- (150) Bonanni, A.; Chua, C. K.; Zhao, G.; Sofer, Z.; Pumera, M. Inherently Electroactive Graphene Oxide Nanoplatelets As Labels for Single Nucleotide Polymorphism Detection. *ACS Nano* **2012**, *6*, 8546–8551.
- (151) Goedert, M.; Spillantini, M. G. A Century of Alzheimer's Disease. *Science* **2006**, *314*, 777–781.
- (152) Li, Q.; Liu, L.; Zhang, S.; Xu, M.; Wang, X.; Wang, C.; Besenbacher, F.; Dong, M. Modulating $A\beta_{33-42}$ Peptide Assembly by Graphene Oxide. *Chem. - Eur. J.* **2014**, *20*, 7236–7240.
- (153) Mahmoudi, M.; Akhavan, O.; Ghavami, M.; Rezaee, F.; Ghiasi, S. M. A. Graphene Oxide Strongly Inhibits Amyloid Beta Fibrillation. *Nanoscale* **2012**, *4*, 7322–7325.
- (154) Wang, J.; Cao, Y.; Li, Q.; Liu, L.; Dong, M. Size Effect of Graphene Oxide on Modulating Amyloid Peptide Assembly. *Chem. - Eur. J.* **2015**, *21*, 9632–9637.
- (155) Wahid, M. H.; Stroeher, U. H.; Eroglu, E.; Chen, X.; Vimalanathan, K.; Raston, C. L.; Boulos, R. A. Aqueous Based Synthesis of Antimicrobial-Decorated Graphene. *J. Colloid Interface Sci.* **2015**, *443*, 88–96.
- (156) Zhou, L.; Jiang, H.; Wei, S.; Ge, X.; Zhou, J.; Shen, J. High-Efficiency Loading of Hypocrellin B on Graphene Oxide for Photodynamic Therapy. *Carbon* **2012**, *50*, 5594–5604.
- (157) Chowdhury, S. M.; Surhland, C.; Sanchez, Z.; Chaudhary, P.; Kumar, M. A. S.; Lee, S.; Peña, L. A.; Waring, M.; Sitharaman, B.; Naidu, M. Graphene Nanoribbons as a Drug Delivery Agent for Lucanthone Mediated Therapy of Glioblastoma Multiforme. *Nanomedicine* **2015**, *11*, 109–118.
- (158) Rahmanian, N.; Hamishehkar, H.; Dolatabadi, J. E. N.; Arsalani, N. Nano Graphene Oxide: A Novel Carrier for Oral Delivery of Flavonoids. *Colloids Surf., B* **2014**, *123*, 331–338.
- (159) Liu, Z.; Robinson, J. T.; Sun, X.; Dai, H. PEGylated Nanographene Oxide for Delivery of Water-Insoluble Cancer Drugs. *J. Am. Chem. Soc.* **2008**, *130*, 10876–10877.
- (160) Georgakilas, V.; Kouloumpis, A.; Gournis, D.; Bourlinos, A.; Trapalis, C.; Zboril, R. Tuning the Dispersibility of Carbon Nanostructures from Organophilic to Hydrophilic: Towards the Preparation of New Multipurpose Carbon-Based Hybrids. *Chem. - Eur. J.* **2013**, *19*, 12884–12891.
- (161) Balcioglu, M.; Rana, M.; Yigit, M. V. Doxorubicin Loading on Graphene Oxide, Iron Oxide and Gold Nanoparticle Hybrid. *J. Mater. Chem. B* **2013**, *1*, 6187–6193.
- (162) Koninti, R. K.; Sengupta, A.; Gavvala, K.; Ballav, N.; Hazra, P. Loading of an Anti-Cancer Drug onto Graphene Oxide and Subsequent Release to DNA/RNA: A Direct Optical Detection. *Nanoscale* **2014**, *6*, 2937–2944.
- (163) Chia, J. S. Y.; Tan, M. T. T.; Khiew, P. S.; Chin, J. K.; Siong, C. W. A Bio-Electrochemical Sensing Platform for Glucose Based on Irreversible, Non-Covalent π - π Functionalization of Graphene Produced via a Novel, Green Synthesis Method. *Sens. Actuators, B* **2015**, *210*, 558–565.
- (164) Kong, N.; Liua, J.; Kong, Q.; Wang, R.; Barrow, C. J.; Yang, W. Graphene Modified Gold Electrode via Stacking Interaction for Analysis of Cu^{2+} and Pb^{2+} . *Sens. Actuators, B* **2013**, *178*, 426–433.
- (165) Shen, X.; Liu, Y.; Pang, Y.; Yao, W. Conjugation of Graphene on Au Surface by π - π Interaction and Click Chemistry. *Electrochem. Commun.* **2013**, *30*, 13–16.
- (166) Zhang, S.; Tang, S.; Lei, J.; Dong, H.; Ju, H. Functionalization of Graphene Nanoribbons with Porphyrin for Electrocatalysis and Amperometric Biosensing. *J. Electroanal. Chem.* **2011**, *656*, 285–288.
- (167) Srinivasan, S.; Je, S. H.; Back, S.; Barin, G.; Buyukcakil, O.; Guliyev, R.; Jung, Y.; Coskun, A. Ordered Supramolecular Gels Based on Graphene Oxide and Tetracationic Cyclophanes. *Adv. Mater.* **2014**, *26*, 2725–2729.
- (168) Georgakilas, V.; Perman, J. A.; Tucek, J.; Zboril, R. Broad Family of Carbon Nanoallotropes – Classification, Chemistry and Advanced Architecture of Fullerene, Nanotube, Graphene and their Relatives. *Chem. Rev.* **2015**, *115*, 4744–4822.
- (169) Shao, Q.; Tang, J.; Lin, Y.; Li, J.; Qin, F.; Yuan, J.; Qin, L. C. Carbon Nanotube Spaced Graphene Aerogels with Enhanced Capacitance in Aqueous and Ionic Liquid Electrolytes. *J. Power Sources* **2015**, *278*, 751–759.
- (170) Georgakilas, V.; Demeslis, A.; Ntararas, E.; Kouloumpis, A.; Dimos, K.; Gournis, D.; Kocman, M.; Otyepka, M.; Zboril, R. Hydrophilic Nanotube Supported Graphene-Water Dispersible Carbon Superstructure with Excellent Conductivity. *Adv. Funct. Mater.* **2015**, *25*, 1481–1487.
- (171) Tang, C.; Long, G.; Hu, X.; Wong, K.; Lau, W. M.; Fan, M.; Mei, J.; Xu, T.; Wang, B.; Huid, D. Conductive Polymer Nanocomposites with Hierarchical Multi-Scale Structures via Self-Assembly of Carbon-Nanotubes on Graphene on Polymer-microspheres. *Nanoscale* **2014**, *6*, 7877–7888.
- (172) Li, G.; Shrotriya, V.; Huang, J. S.; Yao, Y.; Moriarty, T.; Emery, K.; Yang, Y. High-Efficiency Solution Processable Polymer Photovoltaic Cells by Self-Organization of Polymer Blends. *Nat. Mater.* **2005**, *4*, 864–868.
- (173) Kim, J. Y.; Lee, K.; Coates, N. E.; Moses, D.; Nguyen, T. Q.; Dante, M.; Heeger, A. J. Efficient Tandem Polymer Solar Cells Fabricated by All-Solution Processing. *Science* **2007**, *317*, 222–225.
- (174) Guenes, S.; Neugebauer, H.; Sariciftci, N. S. Conjugated Polymer-Based Organic Solar Cells. *Chem. Rev.* **2007**, *107*, 1324–1338.
- (175) Kim, Y.; Cook, S.; Tuladhar, S. M.; Choulis, S. A.; Nelson, J.; Durrant, R. J.; Bradley, D. D. C.; Giles, M.; McCulloch, I.; Ha, C. S.; et al. A Strong Regioregularity Effect in Self-Organizing Conjugated Polymer Films and High-Efficiency Polythiophene: Fullerene Solar Cells. *Nat. Mater.* **2006**, *5*, 197–203.
- (176) Qu, S.; Li, M.; Xie, L.; Huang, X.; Yang, J.; Wang, N.; Yang, S. Noncovalent Functionalization of Graphene Attaching [6,6]-Phenyl- C_{61} -butyric Acid Methyl Ester (PCBM) and Application as Electron Extraction Layer of Polymer Solar Cells. *ACS Nano* **2013**, *7*, 4070–4081.
- (177) Gan, T.; Hu, C.; Sun, Z.; Hu, S. Facile Synthesis of Water-Soluble Fullerene–Graphene Oxide Composites for Electrodeposition of Phosphotungstic Acid-Based Electrocatalysts. *Electrochim. Acta* **2013**, *111*, 738–745.
- (178) Ba, H.; Podila, S.; Liu, Y.; Mua, X.; Nhuta, J. M.; Papaefthimiou, V.; Zafeirotas, S.; Granger, P.; Huu, C. P. Nanodiamond Decorated Few-Layer Graphene Composite as An efficient Metal-Free Dehydrogenation Catalyst for Styrene Production. *Catal. Today* **2015**, *249*, 167–175.
- (179) Pastor, I. R.; Fernandez, G. R.; Rizo, H. V.; Terrones, M.; Gullon, I. M. Towards the Understanding of the Graphene Oxide Structure: How to Control the Formation of Humic- and Fulvic-Like Oxidized Debris. *Carbon* **2015**, *84*, 299–309.
- (180) Rourke, J. P.; Pandey, P. A.; Moore, J. J.; Bates, M.; Kinloch, I. A.; Young, R. J.; Wilson, N. R. The Real Graphene Oxide Revealed: Stripping the Oxidative Debris from the Graphene Like Sheets. *Angew. Chem., Int. Ed.* **2011**, *50*, 3173–3177.
- (181) Thomas, H. R.; Valles, C.; Young, R. J.; Kinloch, I. A.; Wilson, N. R.; Rourke, J. P. Identifying the Fluorescence of Graphene Oxide. *J. Mater. Chem. C* **2013**, *1*, 338–342.
- (182) Bonanni, A.; Ambrosi, A.; Chua, C. K.; Pumera, M. Oxidation Debris in Graphene Oxide Is Responsible for Its Inherent Electroactivity. *ACS Nano* **2014**, *8*, 4197–4204.
- (183) Coluci, V. R.; Martinez, D. S. T.; Honório, J. G.; de Faria, A. F.; Morales, D. A.; Skaf, M. S.; Alves, O. L.; Umbuzeiro, G. A. Noncovalent Interaction with Graphene Oxide: The Crucial Role of Oxidative Debris. *J. Phys. Chem. C* **2014**, *118*, 2187–2193.
- (184) Gupta, A.; Sakthivel, T.; Seal, S. Recent Development in 2D Materials beyond Graphene. *Prog. Mater. Sci.* **2015**, *73*, 44–126.

- (185) Wang, Q. H.; Kalantar-Zadeh, K.; Kis, A.; Coleman, J. N.; Strano, M. S. Electronics and Optoelectronics of Two Dimensional Transition Metal Dichalcogenides. *Nat. Nanotechnol.* **2012**, *7*, 699–712.
- (186) Splendiani, A.; Sun, L.; Zhang, Y.; Li, T.; Kim, J.; Chim, C. Y.; Galli, G.; Wang, F. Emerging Photoluminescence in Monolayer MoS₂. *Nano Lett.* **2010**, *10*, 1271–1275.
- (187) Thirupuranthaka, M.; Late, D. J. Temperature Dependent Phonon Shifts in Single-Layer WS₂. *ACS Appl. Mater. Interfaces* **2014**, *6*, 1158–1163.
- (188) Miremadi, B. K.; Morrison, S. R. High Activity Catalyst from Exfoliated MoS₂. *J. Catal.* **1987**, *103*, 334–345.
- (189) Novoselov, K. S.; Jiang, D.; Schedin, F.; Booth, T. J.; Khotkevich, V. V.; Morozov, S. V.; Geim, A. K. Two-Dimensional Atomic Crystals. *Proc. Natl. Acad. Sci. U. S. A.* **2005**, *102*, 10451–10453.
- (190) Coleman, J. N.; Lotya, M.; O'Neill, A.; Bergin, S. D.; King, P. J.; Khan, U.; Young, K.; Gaucher, A.; De, S.; Smith, R. J.; et al. Two-Dimensional Nanosheets Produced by Liquid Exfoliation of Layered Materials. *Science* **2011**, *331*, 568–571.
- (191) Song, S. H.; Kim, B. H.; Choe, D. H.; Kim, J.; Kim, D. C.; Lee, D. J.; Kim, J. M.; Chang, K. J.; Jeon, S. Bandgap Widening of Phase Quilted, 2D MoS₂ by Oxidative Intercalation. *Adv. Mater.* **2015**, *27*, 3152–3158.
- (192) Zhan, Y.; Liu, Z.; Najmaei, S.; Ajayan, P. M.; Lou, J. Large-Area Vapor-Phase Growth and Characterization of MoS₂ Atomic Layers on a SiO₂ Substrate. *Small* **2012**, *8*, 966–971.
- (193) Lee, Y. H.; Zhang, X. Q.; Zhang, W. J.; Chang, M. T.; Lin, C. T.; Chang, K. D.; Yu, Y. C.; Wang, J. T. W.; Chang, C. S.; Li, L. J.; et al. Synthesis of Large-Area MoS₂ Atomic Layers with Chemical Vapor Deposition. *Adv. Mater.* **2012**, *24*, 2320–2325.
- (194) Zhang, Y.; Chang, T. R.; Zhou, B.; Cui, Y. T.; Yan, H.; Liu, Z.; Schmitt, F.; Lee, J.; Moore, R.; Chen, Y.; et al. Direct Observation of the Transition from Indirect to Direct Bandgap in Atomically Thin Epitaxial MoSe₂. *Nat. Nanotechnol.* **2013**, *9*, 111–115.
- (195) Liu, Z.; Song, L.; Zhao, S.; Huang, J.; Ma, L.; Zhang, J.; Lou, J.; Ajayan, P. M. Direct Growth of Graphene/Hexagonal Boron Nitride Stacked Layers. *Nano Lett.* **2011**, *11*, 2032–2037.
- (196) Yu, L.; Lee, Y. H.; Ling, X.; Santos, E. J. G.; Shin, Y. C.; Lin, Y.; Dubey, M.; Kaxiras, E.; Kong, J.; Wang, H.; et al. Graphene/MoS₂ Hybrid Technology for Large-Scale Two-Dimensional Electronics. *Nano Lett.* **2014**, *14*, 3055–3063.
- (197) Li, Y.; Wang, H.; Xie, L.; Liang, Y.; Hong, G.; Dai, H. MoS₂ Nanoparticles Grown on Graphene: An Advanced Catalyst for the Hydrogen Evolution Reaction. *J. Am. Chem. Soc.* **2011**, *133*, 7296–7299.
- (198) Roy, K.; Padmanabhan, M.; Goswami, S.; Sai, T. P.; Kaushal, S.; Ghosh, A. Optically Active Heterostructures of Graphene and Ultrathin MoS₂. *Solid State Commun.* **2013**, *175*, 35–42.
- (199) Roy, K.; Padmanabhan, M.; Goswami, S.; Sai, T. P.; Ramalingam, G.; Raghavan, S.; Ghosh, A. Graphene–MoS₂ Hybrid Structures for Multifunctional Photoresponsive Memory Devices. *Nat. Nanotechnol.* **2013**, *8*, 826–830.
- (200) Loan, P. T. K.; Zhang, W.; Lin, C. T.; Wei, K. H.; Li, L. J.; Chen, C. H. Graphene/MoS₂ Heterostructures for Ultrasensitive Detection of DNA Hybridisation. *Adv. Mater.* **2014**, *26*, 4838–4844.
- (201) Zeng, S.; Hu, S.; Xia, J.; Anderson, T.; Dinh, X. Q.; Meng, X. M.; Coquet, P.; Yong, K. T. Graphene–MoS₂ Hybrid Nanostructures Enhanced Surface Plasmon Resonance Biosensors. *Sens. Actuators, B* **2015**, *207*, 801–810.
- (202) Meng, J.; Song, H. D.; Li, C. Z.; Jin, Y.; Tang, L.; Liu, D.; Liao, Z. M.; Xiu, F.; Yu, D. P. Lateral Graphene p-n Junctions Formed by Graphene/MoS₂ Hybrid Interface. *Nanoscale* **2015**, *7*, 11611–11619.
- (203) Shiva, K.; Matte, H. S. S. R.; Rajendra, H. B.; Bhattacharyya, A. J.; Rao, C. N. R. Employing Synergistic Interactions Between Few-Layer WS₂ and Reduced Graphene Oxide to Improve Lithium Storage, Cyclability and Rate Capability of Li-Ion Batteries. *Nano Energy* **2013**, *2*, 787–793.
- (204) Roy, T.; Tosun, M.; Kang, J. S.; Sachid, A. B.; Desai, S. B.; Hettick, M.; Hu, C. C.; Javey, A. Field-Effect Transistors Built from All Two-Dimensional Material Components. *ACS Nano* **2014**, *8*, 6259–6264.
- (205) Zhang, S.; Zhang, X.; Jiang, G.; Zhu, H.; Guo, S.; Su, D.; Lu, G.; Sun, S. Tuning Nanoparticle Structure and Surface Strain for Catalysis Optimization. *J. Am. Chem. Soc.* **2014**, *136*, 7734–7739.
- (206) Liu, X.; Sui, Y. H.; Meng, C. G.; Han, Y. Tuning the Reactivity of Ru Nanoparticles by Defect Engineering of the Reduced Graphene Oxide Support. *RSC Adv.* **2014**, *4*, 22230–22240.
- (207) Duan, J.; Chen, S.; Dai, S.; Qiao, S. Z. Shape Control of Mn₃O₄ Nanoparticles on Nitrogen-Doped Graphene for Enhanced Oxygen Reduction Activity. *Adv. Funct. Mater.* **2014**, *24*, 2072–2078.
- (208) Li, W.; Wang, F.; Feng, S.; Wang, J.; Sun, Z.; Li, B.; Li, Y.; Yang, J.; Elzatahry, A. A.; Xia, Y.; et al. Sol-Gel Design Strategy for Ultradispersed TiO₂ Nanoparticles on Graphene for High-Performance Lithium Ion Batteries. *J. Am. Chem. Soc.* **2013**, *135*, 18300–18303.
- (209) Guo, S.; Zhang, S.; Wu, L.; Sun, S. Co/CoO Nanoparticles Assembled on Graphene for Electrochemical Reduction of Oxygen. *Angew. Chem., Int. Ed.* **2012**, *51*, 11770–11773.
- (210) Duy-Thach, P.; Chung, G. S. A Novel Pd Nanocube-Graphene Hybrid for Hydrogen Detection. *Sens. Actuators, B* **2014**, *199*, 354–360.
- (211) Jabeen, H.; Kemp, K. C.; Chandra, V. Synthesis of Nano Zerovalent Iron Nanoparticles - Graphene Composite for the Treatment of Lead Contaminated Water. *J. Environ. Manage.* **2013**, *130*, 429–435.
- (212) Seema, H.; Kemp, K. C.; Chandra, V.; Kim, K. S. Graphene-SnO₂ Composites for Highly Efficient Photocatalytic Degradation of Methylene Blue under Sunlight. *Nanotechnology* **2012**, *23*, 355705.
- (213) Jin, S.; Chen, M.; Dong, H.; He, B.; Lu, H.; Su, L.; Dai, W.; Zhang, Q.; Zhang, X. Stable Silver Nanoclusters Electrochemically Deposited on Nitrogen-Doped Graphene as Efficient Electrocatalyst for Oxygen Reduction Reaction. *J. Power Sources* **2015**, *274*, 1173–1179.
- (214) Hui, K. S.; Hui, K. N.; Dinh, D. A.; Tsang, C. H.; Cho, Y. R.; Zhou, W.; Hong, X.; Chun, H. H. Green Synthesis of Dimension-Controlled Silver Nanoparticle-Graphene Oxide with in Situ Ultrasonication. *Acta Mater.* **2014**, *64*, 326–332.
- (215) Moussa, S.; Siamaki, A. R.; Gupton, B. F.; El-Shall, M. S. Pd-Partially Reduced Graphene Oxide Catalysts (Pd/PRGO): Laser Synthesis of Pd Nanoparticles Supported on PRGO Nanosheets for Carbon-Carbon Cross Coupling Reactions. *ACS Catal.* **2012**, *2*, 145–154.
- (216) Liu, G.; Wang, Y.; Pu, X.; Jiang, Y.; Cheng, L.; Jiao, Z. One-Step Synthesis of High Conductivity Silver Nanoparticle-Reduced Graphene Oxide Composite Films by Electron Beam Irradiation. *Appl. Surf. Sci.* **2015**, *349*, 570–575.
- (217) Haider, M. S.; Badejo, A. C.; Shao, G. N.; Imran, S. M.; Abbas, N.; Chai, Y. G.; Hussain, M.; Kim, H. T. Sequential Repetitive Chemical Reduction Technique to Study Size-Property Relationships of Graphene Attached Ag Nanoparticle. *Solid State Sci.* **2015**, *44*, 1–9.
- (218) Shi, J.; Zhou, X.; Liu, Y.; Su, Q.; Zhang, J.; Du, G. Sonochemical Synthesis of CuS/Reduced Graphene Oxide Nanocomposites with Enhanced Absorption and Photocatalytic Performance. *Mater. Lett.* **2014**, *126*, 220–223.
- (219) Thangaraju, D.; Karthikeyan, R.; Prakash, N.; Babuc, S. M.; Hayakawa, Y. Growth and Optical Properties of Cu₂ZnSnS₄ Decorated Reduced Graphene Oxide Nanocomposites. *Dalton Trans.* **2015**, *44*, 15031–15041.
- (220) Bera, R.; Kundu, S.; Patra, A. 2D Hybrid Nanostructure of Reduced Graphene Oxide-CdS Nanosheet for Enhanced Photocatalysis. *ACS Appl. Mater. Interfaces* **2015**, *7*, 13251–13259.
- (221) Wang, Z.; Shi, G.; Zhang, F.; Xia, J.; Gui, R.; Yang, M.; Bi, S.; Xia, L.; Li, Y.; Xia, L.; et al. Amphoteric Surfactant Promoted Three-Dimensional Assembly of Graphene Micro/Nanoclusters to Accommodate Pt Nanoparticles for Methanol Oxidation. *Electrochim. Acta* **2015**, *160*, 288–295.
- (222) Atar, N.; Eren, T.; Yola, M. L.; Gerengi, H.; Wang, S. Fe@Ag Nanoparticles Decorated Reduced Graphene Oxide as Ultrahigh Capacity Anode Material for Lithium-Ion Battery. *Ionics* **2015**, *21*, 3185–3192.
- (223) Fonsaca, J. E. S.; Elias, A. L.; Domingues, S. H.; Oliveira, M. M.; Endo, M.; Orth, E. S.; Terrones, M.; Zabin, A. J. G. Graphene

Nanoribbons Inducing Cube-Shaped Ag Nanoparticle Assemblies. *Carbon* **2015**, 93, 800–811.

(224) Toth, P. S.; Velický, M.; Ramasse, Q. M.; Kepaptsoglou, D. M.; Dryfe, R. A. W. Symmetric and Asymmetric Decoration of Graphene: Bimetal-Graphene Sandwiches. *Adv. Funct. Mater.* **2015**, 25, 2899–2909.

(225) Xiao, F.-X.; Miao, J.; Liu, B. Layer-by-Layer Self-Assembly of CdS Quantum Dots/Graphene Nanosheets Hybrid Films for Photoelectrochemical and Photocatalytic Applications. *J. Am. Chem. Soc.* **2014**, 136, 1559–1569.

(226) Zhou, R.; Qiao, S. Z. Silver/Nitrogen-Doped Graphene Interaction and Its Effect on Electrocatalytic Oxygen Reduction. *Chem. Mater.* **2014**, 26, 5868–5873.

(227) Kemp, K. C.; Vimlesh, C.; Muhammad, S.; Kim, K. S. Reversible CO₂ Adsorption by an Activated Nitrogen Doped Graphene/Polyaniline Material. *Nanotechnology* **2013**, 24, 235703.

(228) Park, S.; Hu, Y.; Hwang, J. O.; Lee, E.-S.; Casabianca, L. B.; Cai, W.; Potts, J. R.; Ha, H.-W.; Chen, S.; Oh, J.; et al. Chemical Structures of Hydrazine-Treated Graphene Oxide and Generation of Aromatic Nitrogen Doping. *Nat. Commun.* **2012**, 3, 638.

(229) Marquardt, D.; Beckert, F.; Pennetreau, F.; Tölle, F.; Mühlaupt, R.; Riant, O.; Hermans, S.; Barthel, J.; Janiak, C. Hybrid Materials of Platinum Nanoparticles and Thiol-Functionalized Graphene Derivatives. *Carbon* **2014**, 66, 285–294.

(230) Cui, L.; Wu, J.; Ju, H. Synthesis of Bismuth-Nanoparticle-Enriched Nanoporous Carbon on Graphene for Efficient Electrochemical Analysis of Heavy-Metal Ions. *Chem. - Eur. J.* **2015**, 21, 11525–11530.

(231) Wei, W.; Wang, G.; Yang, S.; Feng, X. L.; Mullen, K. Efficient Coupling of Nanoparticles to Electrochemically Exfoliated Graphene. *J. Am. Chem. Soc.* **2015**, 137, 5576–5581.

(232) Lee, W. C.; Kim, K.; Park, J.; Koo, J.; Jeong, H. Y.; Lee, H.; Weitz, D. A.; Zettl, A.; Takeuchi, S. Graphene-Templated Directional Growth of an Inorganic Nanowire. *Nat. Nanotechnol.* **2015**, 10, 423–428.

(233) Yu, S. U.; Park, B.; Cho, Y.; Hyun, S.; Kim, J. K.; Kim, K. S. Simultaneous Visualization of Graphene Grain Boundaries and Wrinkles with Structural Information by Gold Deposition. *ACS Nano* **2014**, 8, 8662–8668.

(234) Duong, D. L.; Han, G. H.; Lee, S. M.; Gunes, F.; Kim, E. S.; Kim, S. T.; Kim, H.; Ta, Q. H.; So, K. P.; Yoon, S. J.; et al. Probing Graphene Grain Boundaries with Optical Microscopy. *Nature* **2012**, 490, 235–240.

(235) Yu, S. U.; Cho, Y.; Park, B.; Kim, N.; Youn, I. S.; Son, M.; Kim, J. K.; Choi, H. C.; Kim, K. S. Fast benchtop visualization of graphene grain boundaries using adhesive properties of defects. *Chem. Commun.* **2013**, 49, 5474–5476.

(236) Kim, D. W.; Kim, Y. H.; Jeong, H. S.; Jung, H. T. Direct Visualization of Large-Area Graphene Domains and Boundaries by Optical Birefringency. *Nat. Nanotechnol.* **2011**, 7, 29–34.

(237) Zhang, H. M.; Yu, X. Z.; Guo, D.; Qu, B. H.; Zhang, M.; Li, Q. H.; Wang, T. H. Synthesis of Bacteria Promoted Reduced Graphene Oxide-Nickel Sulfide Networks for Advanced Supercapacitors. *ACS Appl. Mater. Interfaces* **2013**, 5, 7335–7340.

(238) Shi, Y.; Wang, J. Z.; Chou, S. L.; Wexler, D.; Li, H. J.; Ozawa, K.; Liu, H. K.; Wu, Y. P. Hollow Structured Li₃VO₄ Wrapped with Graphene Nanosheets in Situ Prepared by a One-Pot Template-Free Method as an Anode for Lithium-Ion Batteries. *Nano Lett.* **2013**, 13, 4715–4720.

(239) Hu, J. T.; Zheng, J. X.; Tian, L. L.; Duan, Y. D.; Lin, L. P.; Cui, S. H.; Peng, H.; Liu, T. C.; Guo, H.; Wang, X. W.; et al. A Core-Shell Nanohollow- γ -Fe₂O₃@Graphene Hybrid Prepared through the Kirkendall Process as a High Performance Anode Material for Lithium Ion Batteries. *Chem. Commun.* **2015**, 51, 7855–7858.

(240) Sengar, S. K.; Mehta, B. R.; Kumar, R.; Singh, V. In-Flight Gas Phase Growth of Metal/Multilayer Graphene Core Shell Nanoparticles with Controllable Sizes. *Sci. Rep.* **2013**, 3, 2814.

(241) Moon, H.; Kumar, D.; Kim, H.; Sim, C.; Chang, J. H.; Kim, J. M.; Kim, H.; Lim, D. K. Amplified Photoacoustic Performance and Enhanced Photothermal Stability of Reduced Graphene Oxide Coated

Gold Nanorods for Sensitive Photo acoustic Imaging. *ACS Nano* **2015**, 9, 2711–2719.

(242) Si, Y.; Samulski, E. T. Exfoliated Graphene Separated by Platinum Nanoparticles. *Chem. Mater.* **2008**, 20, 6792–6797.

(243) Buglione, L.; Bonanni, A.; Ambrosi, A.; Pumera, M. Gold Nanospacers Greatly Enhance the Capacitance of Electrochemically Reduced Graphene. *ChemPlusChem* **2012**, 77, 71–73.

(244) Wu, Z.-S.; Ren, W.; Wen, L.; Gao, L.; Zhao, J.; Chen, Z.; Zhou, G.; Li, F.; Cheng, H.-M. Graphene Anchored with Co₃O₄ Nanoparticles as Anode of Lithium Ion Batteries with Enhanced Reversible Capacity and Cyclic Performance. *ACS Nano* **2010**, 4, 3187–3194.

(245) Liu, Y.; Wang, R.; Yan, X. Synergistic Effect between Ultra-Small Nickel Hydroxide Nanoparticles and Reduced Graphene Oxide Sheets for the Application in High-Performance Asymmetric Supercapacitor. *Sci. Rep.* **2015**, 5, 11095.

(246) Tiwari, J. N.; Kemp, K. C.; Nath, K.; Tiwari, R. N.; Nam, H.-G.; Kim, K. S. Interconnected Pt-Nanodendrite/DNA/Reduced-Graphene-Oxide Hybrid Showing Remarkable Oxygen Reduction Activity and Stability. *ACS Nano* **2013**, 7, 9223–9231.

(247) Tiwari, J. N.; Nath, K.; Kumar, S.; Tiwari, R. N.; Kemp, K. C.; Le, N. H.; Youn, D. H.; Lee, J. S.; Kim, K. S. Stable Platinum Nanoclusters on Genomic DNA-Graphene Oxide with a High Oxygen Reduction Reaction Activity. *Nat. Commun.* **2013**, 4, 2221.

(248) Huang, Y. X.; Xie, J. F.; Zhang, X.; Xiong, L.; Yu, H. Q. Reduced Graphene Oxide Supported Palladium Nanoparticles via Photoassisted Citrate Reduction for Enhanced Electrocatalytic Activities. *ACS Appl. Mater. Interfaces* **2014**, 6, 15795–15801.

(249) Yin, H. J.; Tang, H. J.; Wang, D.; Gao, Y.; Tang, Z. Y. Facile Synthesis of Surfactant-Free Au Cluster/Graphene Hybrids for High-Performance Oxygen Reduction Reaction. *ACS Nano* **2012**, 6, 8288–8297.

(250) Li, Y.; Yu, Y.; Wang, J.-G.; Song, J.; Li, Q.; Dong, M.; Liu, C.-J. CO Oxidation over Graphene Supported Palladium Catalyst. *Appl. Catal., B* **2012**, 125, 189–196.

(251) Grayfer, E. D.; Kibis, L. S.; Stadnichenko, A. I.; Vilkov, O. Y.; Boronin, A. I.; Slavinskaya, E. M.; Stonkus, O. A.; Fedorov, V. E. Ultradisperse Pt Nanoparticles Anchored on Defect Sites in Oxygen-Free Few-Layer Graphene and Their Catalytic Properties in CO Oxidation. *Carbon* **2015**, 89, 290–299.

(252) Zhang, C.; Lv, W.; Yang, Q.; Liu, Y. Graphene Supported Nanoparticles of Pt–Ni for CO Oxidation. *Appl. Surf. Sci.* **2012**, 258, 7795–7800.

(253) Qu, L. T.; Liu, Y.; Baek, J. B.; Dai, L. M. Nitrogen-Doped Graphene as Efficient Metal-Free Electrocatalyst for Oxygen Reduction in Fuel Cells. *ACS Nano* **2010**, 4, 1321–1326.

(254) Yang, Z.; Yao, Z.; Li, G. F.; Fang, G. Y.; Nie, H. G.; Liu, Z.; Zhou, X. M.; Chen, X.; Huang, S. M. Sulfur-Doped Graphene as an Efficient Metal-free Cathode Catalyst for Oxygen Reduction. *ACS Nano* **2012**, 6, 205–211.

(255) Zhang, C. Z.; Mahmood, N.; Yin, H.; Liu, F.; Hou, Y. L. Synthesis of Phosphorus-Doped Graphene and its Multifunctional Applications for Oxygen Reduction Reaction and Lithium Ion Batteries. *Adv. Mater.* **2013**, 25, 4932–4937.

(256) Wang, L.; Ambrosi, A.; Pumera, M. “Metal-Free” Catalytic Oxygen Reduction Reaction on Heteroatom-Doped Graphene is Caused by Trace Metal Impurities. *Angew. Chem., Int. Ed.* **2013**, 52, 13818–13821.

(257) Wang, L.; Ambrosi, A.; Pumera, M. Could Carbonaceous Impurities in Reduced Graphenes be Responsible for Some of Their Extraordinary Electrocatalytic Activities? *Chem. - Asian J.* **2013**, 8, 1200–1204.

(258) Yang, J.; Voiry, D.; Ahn, S. J.; Kang, D.; Kim, A. Y.; Chhowalla, M.; Shin, H. S. Two-Dimensional Hybrid Nanosheets of Tungsten Disulfide and Reduced Graphene Oxide as Catalysts for Enhanced Hydrogen Evolution. *Angew. Chem., Int. Ed.* **2013**, 52, 13751–13754.

(259) Peng, S. J.; Li, L. L.; Han, X. P.; Sun, W. P.; Srinivasan, M.; Mhaisalkar, S. G.; Cheng, F. Y.; Yan, Q. Y.; Chen, J.; Ramakrishna, S. Cobalt Sulfide Nanosheet/Graphene/Carbon Nanotube Nanocompo-

sites as Flexible Electrodes for Hydrogen Evolution. *Angew. Chem., Int. Ed.* **2014**, *53*, 12594–12599.

(260) He, C. Y.; Tao, J. Z. Synthesis of Nanostructured Clean Surface Molybdenum Carbides on Graphene Sheets as Efficient and Stable Hydrogen Evolution Reaction Catalysts. *Chem. Commun.* **2015**, *51*, 8323–8325.

(261) Youn, D. H.; Han, S.; Kim, J. Y.; Kim, J. Y.; Park, H.; Choi, S. H.; Lee, J. S. Highly Active and Stable Hydrogen Evolution Electrocatalysts Based on Molybdenum Compounds on Carbon Nanotube-Graphene Hybrid Support. *ACS Nano* **2014**, *8*, 5164–5173.

(262) Bai, S.; Wang, C. M.; Deng, M. S.; Gong, M.; Bai, Y.; Jiang, J.; Xiong, Y. J. Surface Polarization Matters: Enhancing the Hydrogen-Evolution Reaction by Shrinking Pt Shells in Pt-Pd-Graphene Stack Structures. *Angew. Chem., Int. Ed.* **2014**, *53*, 12120–12124.

(263) Yan, H. J.; Tian, C. G.; Wang, L.; Wu, A. P.; Meng, M. C.; Zhao, L.; Fu, H. G. Phosphorus-Modified Tungsten Nitride/Reduced Graphene Oxide as a High-Performance, Non-Noble-Metal Electrocatalyst for the Hydrogen Evolution Reaction. *Angew. Chem., Int. Ed.* **2015**, *54*, 6325–6329.

(264) Chen, Y.; Zhu, Q. L.; Tsumori, N.; Xu, Q. Immobilizing Highly Catalytically Active Noble Metal Nanoparticles on Reduced Graphene Oxide: A Non-Noble Metal Sacrificial Approach. *J. Am. Chem. Soc.* **2015**, *137*, 106–109.

(265) Yang, J. M.; Wang, S. A.; Sun, C. L.; Ger, M. D. Synthesis of size-selected Pt Nanoparticles Supported on Sulfonated Graphene with Polyvinyl Alcohol for Methanol Oxidation in Alkaline Solutions. *J. Power Sources* **2014**, *254*, 298–305.

(266) Chen, Y.; Yang, J.; Yang, Y.; Peng, Z.; Li, J.; Mei, T.; Wang, J.; Hao, M.; Chen, Y.; Xiong, W.; et al. A Facile Strategy to Synthesize Three-Dimensional Pd@Pt Core-Shell Nanoflowers Supported on Graphene Nanosheets as Enhanced Nanoelectrocatalysts for Methanol Oxidation. *Chem. Commun.* **2015**, *51*, 10490–10493.

(267) Metin, O.; Ho, S. F.; Alp, C.; Can, H.; Mankin, M. N.; Gultekin, M. S.; Chi, M. F.; Sun, S. H. Ni/Pd Core/Shell Nanoparticles Supported on Graphene as a Highly Active and Reusable Catalyst for Suzuki-Miyaura Cross-Coupling Reaction. *Nano Res.* **2013**, *6*, 10–18.

(268) Putta, C.; Sharavath, V.; Sarkar, S.; Ghosh, S. Palladium Nanoparticles on Beta-Cyclodextrin Functionalised Graphene Nanosheets: A Supramolecular Based Heterogeneous Catalyst for C-C Coupling Reactions under Green Reaction Conditions. *RSC Adv.* **2015**, *5*, 6652–6660.

(269) Ren, L.; Yang, F.; Wang, C. X.; Li, Y. F.; Liu, H. L.; Tu, Z. Q.; Zhang, L. Q.; Liu, Z. C.; Gao, J. S.; Xu, C. M. Plasma Synthesis of Oxidized Graphene Foam Supporting Pd Nanoparticles as a New Catalyst for One-Pot Synthesis of Dibenzyls. *RSC Adv.* **2014**, *4*, 63048–63054.

(270) Fang, Y. X.; Wang, E. K. Electrochemical Biosensors on Platforms of Graphene. *Chem. Commun.* **2013**, *49*, 9526–9539.

(271) Wu, W.; Liu, Z. H.; Jauregui, L. A.; Yu, Q. K.; Pillai, R.; Cao, H. L.; Bao, J. M.; Chen, Y. P.; Pei, S. S. Wafer-Scale Synthesis of Graphene by Chemical Vapor Deposition and Its Application in Hydrogen Sensing. *Sens. Actuators, B* **2010**, *150*, 296–300.

(272) Li, M.; Bo, X. J.; Zhang, Y. F.; Han, C.; Guo, L. P. One-Pot Ionic Liquid-Assisted Synthesis of Highly Dispersed PtPd Nanoparticles/Reduced Graphene Oxide Composites for Nonenzymatic Glucose Detection. *Biosens. Bioelectron.* **2014**, *56*, 223–230.

(273) Mukherji, A.; Seger, B.; Lu, G. Q.; Wang, L. Z. Nitrogen Doped Sr₂Ta₂O₇ Coupled with Graphene Sheets as Photocatalysts for Increased Photocatalytic Hydrogen Production. *ACS Nano* **2011**, *5*, 3483–3492.

(274) Li, Q.; Guo, B. D.; Yu, J. G.; Ran, J. R.; Zhang, B. H.; Yan, H. J.; Gong, J. R. Highly Efficient Visible-Light-Driven Photocatalytic Hydrogen Production of CdS-Cluster-Decorated Graphene Nanosheets. *J. Am. Chem. Soc.* **2011**, *133*, 10878–10884.

(275) Meng, F. K.; Li, J. T.; Cushing, S. K.; Zhi, M. J.; Wu, N. Q. Solar Hydrogen Generation by Nanoscale p-n Junction of p-type Molybdenum Disulfide/n-type Nitrogen-Doped Reduced Graphene Oxide. *J. Am. Chem. Soc.* **2013**, *135*, 10286–10289.

(276) Wang, Y.; Yu, J. G.; Xiao, W.; Li, Q. Microwave-Assisted Hydrothermal Synthesis of Graphene Based Au-TiO₂ Photocatalysts for Efficient Visible-Light Hydrogen Production. *J. Mater. Chem. A* **2014**, *2*, 3847–3855.

(277) Martin, S. T.; Lee, A. T.; Hoffmann, M. R. Chemical Mechanism of Inorganic Oxidants in the Process – Increased Rates of Degradation of Chlorinated Hydrocarbons. *Environ. Sci. Technol.* **1995**, *29*, 2567–2573.

(278) Vinayan, B. P.; Nagar, R.; Ramaprabhu, S. Solar Light Assisted Green Synthesis of Palladium Nanoparticle Decorated Nitrogen Doped Graphene for Hydrogen Storage Application. *J. Mater. Chem. A* **2013**, *1*, 11192–11199.

(279) Tuček, J.; Kemp, K. C.; Kim, K. S.; Zbořil, R. Iron-Oxide-Supported Nanocarbon in Lithium-Ion Batteries, Medical, Catalytic, and Environmental Applications. *ACS Nano* **2014**, *8*, 7571–7612.

(280) Kucinskis, G.; Bajars, G.; Kleperis, J. Graphene in Lithium Ion Battery Cathode Materials: A Review. *J. Power Sources* **2013**, *240*, 66–79.

(281) Sun, W. W.; Wang, Y. Graphene-Based Nanocomposite Anodes for Lithium-Ion Batteries. *Nanoscale* **2014**, *6*, 11528–11552.

(282) Yang, Q.; Liang, Q.; Liu, J.; Liang, S. Q.; Tang, S. S.; Lu, P. J.; Lu, Y. K. Ultrafine MoO₃ Nanoparticles Grown on Graphene Sheets as Anode Materials for Lithium-Ion Batteries. *Mater. Lett.* **2014**, *127*, 32–35.

(283) Pan, L.; Zhu, X.-D.; Xie, X.-M.; Liu, Y.-T. Smart Hybridization of TiO₂ Nanorods and Fe₃O₄ Nanoparticles with Pristine Graphene Nanosheets: Hierarchically Nanoengineered Ternary Heterostructures for High-Rate Lithium Storage. *Adv. Funct. Mater.* **2015**, *25*, 3341–3350.

(284) Kasavajjula, U.; Wang, C. S.; Appleby, A. J. Nano- and Bulk-Silicon-Based Insertion Anodes for Lithium-Ion Secondary Cells. *J. Power Sources* **2007**, *163*, 1003–1039.

(285) Zhu, S. M.; Zhu, C. L.; Ma, J.; Meng, Q.; Guo, Z. P.; Yu, Z. Y.; Lu, T.; Li, Y.; Zhang, D.; Lau, W. M. Controlled Fabrication of Si Nanoparticles on Graphene Sheets for Li-Ion Batteries. *RSC Adv.* **2013**, *3*, 6141–6146.

(286) Hassan, F. M.; Elsayed, A. R.; Chabot, V.; Batmaz, R.; Xiao, X. C.; Chen, Z. W. Subeutectic Growth of Single-Crystal Silicon Nanowires Grown on and Wrapped with Graphene Nanosheets: High-Performance Anode Material for Lithium-Ion Battery. *ACS Appl. Mater. Interfaces* **2014**, *6*, 13757–13764.

(287) Zhou, M.; Li, X.; Wang, B.; Zhang, Y.; Ning, J.; Xiao, Z.; Zhang, X.; Chang, Y.; Zhi, L. High-Performance Silicon Battery Anodes Enabled by Engineering Graphene Assemblies. *Nano Lett.* **2015**, *15*, 6222–6228.

(288) Yuan, F. W.; Tuan, H. Y. Scalable Solution-Grown High-Germanium-Nanoparticle-Loading Graphene Nanocomposites as High-Performance Lithium-Ion Battery Electrodes: An Example of a Graphene-Based Platform toward Practical Full-Cell Applications. *Chem. Mater.* **2014**, *26*, 2172–2179.

(289) Zhang, H. W.; Zhou, L.; Noonan, O.; Martin, D. J.; Whittaker, A. K.; Yu, C. Z. Tailoring the Void Size of Iron Oxide@Carbon Yolk-Shell Structure for Optimized Lithium Storage. *Adv. Funct. Mater.* **2014**, *24*, 4337–4342.

(290) Li, Y.; Zhu, C. L.; Lu, T.; Guo, Z. P.; Zhang, D.; Ma, J.; Zhu, S. M. Simple Fabrication of a Fe₂O₃/Carbon Composite for Use in a High-Performance Lithium Ion Battery. *Carbon* **2013**, *52*, 565–573.

(291) Slater, M. D.; Kim, D.; Lee, E.; Johnson, C. S. Sodium-Ion Batteries. *Adv. Funct. Mater.* **2013**, *23*, 947–958.

(292) Yu, D. Y. W.; Prikhodchenko, P. V.; Mason, C. W.; Batabyal, S. K.; Gun, J.; Sladkevich, S.; Medvedev, A. G.; Lev, O. High-Capacity Antimony Sulphide Nanoparticle-Decorated Graphene Composite as Anode for Sodium-Ion Batteries. *Nat. Commun.* **2013**, *4*, 2922.

(293) Xiao, Z. B.; Yang, Z.; Wang, L.; Nie, H. G.; Zhong, M. E.; Lai, Q. Q.; Xu, X. J.; Zhang, L. J.; Huang, S. M. A Lightweight TiO₂/Graphene Interlayer, Applied as a Highly Effective Polysulfide Absorbent for Fast, Long-Life Lithium-Sulfur Batteries. *Adv. Mater.* **2015**, *27*, 2891–2898.

(294) Ryu, W. H.; Yoon, T. H.; Song, S. H.; Jeon, S.; Park, Y. J.; Kim, I. D. Bifunctional Composite Catalysts Using Co₃O₄ Nanofibers

Immobilized on Nonoxidized Graphene Nanoflakes for High-Capacity and Long-Cycle Li-O₂ Batteries. *Nano Lett.* **2013**, *13*, 4190–4197.

(295) Chandra, V.; Park, J.; Chun, Y.; Lee, J. W.; Hwang, I.-C.; Kim, K. S. Water Dispersible Magnetite-Reduced Graphene Oxide Composites for Arsenic Removal. *ACS Nano* **2010**, *4*, 3979–3986.

(296) Hu, Y.; Jensen, J. O.; Zhang, W.; Huang, Y. J.; Cleemann, L. N.; Xing, W.; Bjerrum, N. J.; Li, Q. F. Direct Synthesis of Fe₃C-Functionalized Graphene by High Temperature Autoclave Pyrolysis for Oxygen Reduction. *ChemSusChem* **2014**, *7*, 2099–2103.

(297) Moussa, S. O.; Panchakarla, L. S.; Ho, M. Q.; El-Shall, M. S. Graphene-Supported, Iron-Based Nanoparticles for Catalytic Production of Liquid Hydrocarbons from Synthesis Gas: The Role of the Graphene Support in Comparison with Carbon Nanotubes. *ACS Catal.* **2014**, *4*, 535–545.

(298) Xu, X.; Li, H.; Zhang, Q.; Hu, H.; Zhao, Z.; Li, J.; Li, J.; Qiao, Y.; Gogotsi, Y. Self-Sensing, Ultra light, and Conductive 3D Graphene/Iron Oxide Aerogel Elastomer Deformable in a Magnetic Field. *ACS Nano* **2015**, *9*, 3969–3977.

(299) Chen, Y.; Wang, Y. L.; Zhang, H. B.; Li, X. F.; Gui, C. X.; Yu, Z. Z. Enhanced Electromagnetic Interference Shielding Efficiency of Polystyrene/Graphene Composites with Magnetic Fe₃O₄ Nanoparticles. *Carbon* **2015**, *82*, 67–76.

(300) Yao, K.; Gong, J.; Tian, N. N.; Lin, Y. C.; Wen, X.; Jiang, Z. W.; Na, H.; Tang, T. Flammability Properties and Electromagnetic Interference Shielding of PVC/Graphene Composites Containing Fe₃O₄ nanoparticles. *RSC Adv.* **2015**, *5*, 31910–31919.

(301) Singh, A. P.; Mishra, M.; Hashim, D. P.; Narayanan, T. N.; Hahm, M. G.; Kumar, P.; Dwivedi, J.; Kedawat, G.; Gupta, A.; Singh, B. P.; et al. Probing the Engineered Sandwich Network of Vertically Aligned Carbon Nanotube-Reduced Graphene Oxide Composites for High Performance Electromagnetic Interference Shielding Applications. *Carbon* **2015**, *85*, 79–88.

(302) Kumar, S.; Singh, A. K.; Dasmahapatra, A. K.; Mandal, T. K.; Bandyopadhyay, D. Graphene Based Multifunctional Superbots. *Carbon* **2015**, *89*, 31–40.

(303) Jiang, Z.; Li, J.; Aslan, H.; Li, Q.; Li, Y.; Chen, M.; Huang, Y.; Froning, J. P.; Otyepka, M.; Zboril, R.; et al. A High Efficiency H₂S Gas Sensor Material: Paper Like Fe₂O₃/graphene Nanosheets and Structural Alignment Dependency of Device Efficiency. *J. Mater. Chem. A* **2014**, *2*, 6714–6717.

(304) Wang, K.; Wan, S.; Liu, Q.; Yang, N.; Zhai, J. CdS Quantum Dot-Decorated Titania/Graphene Nanosheets Stacking Structures for Enhanced Photoelectrochemical Solar Cells. *RSC Adv.* **2013**, *3*, 23755–23761.

(305) Bi, E.; Su, Y.; Chen, H.; Yang, X.; Yin, M.; Ye, F.; Li, Z.; Han, L. A Hybrid Catalyst Composed of Reduced Graphene Oxide/Cu₂S Quantum Dots as a Transparent Counter Electrode for Dye Sensitized Solar Cells. *RSC Adv.* **2015**, *5*, 9075–9078.

(306) Fu, M.; Jiao, Q.; Zhao, Y. One-Step Vapor Diffusion Synthesis of Uniform CdS Quantum Dots/Reduced Graphene Oxide Composites as Efficient Visible-Light Photocatalysts. *RSC Adv.* **2014**, *4*, 23242–23250.

(307) Mo, R.; Lei, Z.; Sun, K.; Rooney, D. Facile Synthesis of Anatase TiO₂ Quantum-Dot/Graphene Nanosheet Composites with Enhanced Electrochemical Performance for Lithium-Ion Batteries. *Adv. Mater.* **2014**, *26*, 2084–2088.

(308) Zeng, X.; Tu, W.; Li, J.; Bao, J.; Dai, Z. Photoelectrochemical Biosensor Using Enzyme-Catalyzed in Situ Propagation of CdS Quantum Dots on Graphene Oxide. *ACS Appl. Mater. Interfaces* **2014**, *6*, 16197–16203.

(309) Jiang, S.-D.; Tang, G.; Ma, Y.-F.; Hu, Y.; Song, L. Synthesis of Nitrogen-Doped Graphene-ZnS Quantum Dots Composites with Highly Efficient Visible Light Photodegradation. *Mater. Chem. Phys.* **2015**, *151*, 34–42.

(310) Xia, H.; Hong, C.; Li, B.; Zhao, B.; Lin, Z.; Zheng, M.; Savilov, S. V.; Aldoshin, S. M. Facile Synthesis of Hematite Quantum-Dot/Functionalized Graphene-Sheet Composites as Advanced Anode Materials for Asymmetric Supercapacitors. *Adv. Funct. Mater.* **2015**, *25*, 627–635.

(311) Chao, D.; Zhu, C.; Xia, X.; Liu, J.; Zhang, X.; Wang, J.; Liang, P.; Lin, J.; Zhang, H.; Shen, Z. X.; et al. Graphene Quantum Dots Coated VO₂ Arrays for Highly Durable Electrodes for Li and Na Ion Batteries. *Nano Lett.* **2015**, *15*, 565–573.

(312) Yeh, T. F.; Teng, C. Y.; Chen, S. J.; Teng, H. Nitrogen-Doped Graphene Oxide Quantum Dots as Photocatalysts for Overall Water-Splitting under Visible Light Illumination. *Adv. Mater.* **2014**, *26*, 3297–3303.

(313) Chao, D.; Zhu, C.; Xia, X.; Liu, J.; Zhang, X.; Wang, J.; Liang, P.; Lin, J.; Zhang, H.; Shen, Z. X.; et al. Graphene Quantum Dots Coated VO₂ Arrays for Highly Durable Electrodes for Li and Na Ion Batteries. *Nano Lett.* **2015**, *15*, 565–573.

(314) He, P.; Sun, J.; Tian, S.; Yang, S.; Ding, S.; Ding, G.; Xie, X.; Jiang, M. Processable Aqueous Dispersions of Graphene Stabilized by Graphene Quantum Dots. *Chem. Mater.* **2015**, *27*, 218–226.

(315) Lin, Y.; Chapman, R.; Stevens, M. M. Integrative Self-Assembly of Graphene Quantum Dots and Biopolymers into a Versatile Biosensing Toolkit. *Adv. Funct. Mater.* **2015**, *25*, 3183–3192.

(316) Zhang, Q.; Jie, J.; Diao, S.; Shao, Z.; Zhang, Q.; Wang, L.; Deng, W.; Hu, W.; Xia, H.; Yuan, X.; et al. Solution-Processed Graphene Quantum Dot Deep-UV Photodetectors. *ACS Nano* **2015**, *9*, 1561–1570.

(317) Song, S. H.; Jang, M. H.; Chung, J.; Jin, S. H.; Kim, B. H.; Hur, S. H.; Yoo, S. H.; Cho, Y. H.; Jeon, S. W. Highly Efficient Light-Emitting Diode of Graphene Quantum Dots Fabricated from Graphite Intercalation Compounds. *Adv. Opt. Mater.* **2014**, *2*, 1016–1023.

(318) Kumar, P. N.; Mandal, S.; Deepa, M.; Srivastava, A. K.; Joshi, A. G. Functionalized Graphite Platelets and Lead Sulfide Quantum Dots Enhance Solar Conversion Capability of a Titanium Dioxide/Cadmium Sulfide Assembly. *J. Phys. Chem. C* **2014**, *118*, 18924–18937.

(319) Jung, M. H.; Chu, M. J. Comparative Experiments of Graphene Covalently and Physically Binding CdSe Quantum Dots to Enhance the Electron Transport in Flexible Photovoltaic Devices. *Nanoscale* **2014**, *6*, 9241–9249.

(320) Guo, S.; Bao, D.; Upadhyayula, S.; Wang, W.; Guvenc, A. B.; Kyle, J. R.; Hosseinibay, H.; Bozhilov, K. N.; Vullev, V. I.; Ozkan, C. S.; et al. Photoinduced Electron Transfer Between Pyridine Coated Cadmium Selenide Quantum Dots and Single Sheet Graphene. *Adv. Funct. Mater.* **2013**, *23*, 5199–5211.

(321) Hirose, T.; Kutsuma, Y.; Kurita, A.; Kaneko, T.; Tamai, N. Blinking Suppression of CdTe Quantum Dots on Epitaxial Graphene and the Analysis with Marcus Electron Transfer. *Appl. Phys. Lett.* **2014**, *105*, 083102.

(322) Liu, J.; Kumar, P.; Hu, Y.; Cheng, G. J.; Irudayaraj, J. Enhanced Multiphoton Emission from CdTe/ZnS Quantum Dots Decorated on Single-Layer Graphene. *J. Phys. Chem. C* **2015**, *119*, 6331–6336.

(323) Qin, J.; Wang, X.; Cao, M.; Hu, C. Germanium Quantum Dots Embedded in N-Doping Graphene Matrix with Sponge-Like Architecture for Enhanced Performance in Lithium-Ion Batteries. *Chem. - Eur. J.* **2014**, *20*, 9675–9682.

(324) Sun, X.; Zhou, C.; Xie, M.; Sun, H.; Hu, T.; Lu, F.; Scott, S. M.; George, S. M.; Lian, J. Synthesis of ZnO Quantum Dot/Graphene Nanocomposites by Atomic Layer Deposition with High Lithium Storage Capacity. *J. Mater. Chem. A* **2014**, *2*, 7319–7326.

(325) Zhou, X.; Shi, J.; Liu, Y.; Su, Q.; Zhang, J.; Du, G. Microwave Irradiation Synthesis of Co₃O₄ Quantum Dots/Graphene Composite as Anode Materials for Li-Ion Battery. *Electrochim. Acta* **2014**, *143*, 175–179.

(326) Zhao, S.; Xie, D.; Yu, X.; Su, Q.; Zhang, J.; Du, G. Facile Synthesis of Fe₃O₄@C Quantum Dots/Graphene Nanocomposite with Enhanced Lithium-Storage Performance. *Mater. Lett.* **2015**, *142*, 287–290.

(327) Wei, W.; Yang, S.; Zhou, H.; Lieberwirth, I.; Feng, X.; Müllen, K. 3D Graphene Foams Cross-linked with Pre-encapsulated Fe₃O₄ Nanospheres for Enhanced Lithium Storage. *Adv. Mater.* **2013**, *25*, 2909–2914.

(328) Tayyebi, A.; Tavakoli, M. M.; Outokesh, M.; Shafiekhani, A.; Simchi, A. Supercritical Synthesis and Characterization of Graphene-

PbS Quantum Dots Composite with Enhanced Photovoltaic Properties. *Ind. Eng. Chem. Res.* **2015**, *54*, 7382–7392.

(329) Gao, H.; Shanguan, W.; Hu, G.; Zhu, K. Preparation and Photocatalytic Performance of Transparent Titania Film from Monolayer Titania Quantum Dots. *Appl. Catal., B* **2016**, *180*, 416–423.

(330) Cao, S.; Chen, C.; Zhang, J.; Zhang, C.; Yu, W.; Liang, B.; Tsang, Y. MnO_x Quantum Dots Decorated Reduced Graphene Oxide/TiO₂ Nanohybrids for Enhanced Activity by a UV Pre-Catalytic Microwave Method. *Appl. Catal., B* **2015**, *176–177*, 500–512.

(331) Kaur, P.; Shin, M. S.; Sharma, N.; Kaur, N.; Joshi, A.; Chae, S. R.; Park, J. S.; Kang, M. S.; Sekhon, S. S. Non-Covalent Functionalization of Graphene with Poly(diallyl dimethylammonium) Chloride: Effect of a Non-Ionic Surfactant. *Int. J. Hydrogen Energy* **2015**, *40*, 1541–1547.

(332) Tiwari, J. N.; Tiwari, R. N.; Kim, K. S. Zero-Dimensional, One-Dimensional, Two-Dimensional and Three-Dimensional Nanostructured Materials for Advanced Electrochemical Energy Devices. *Prog. Mater. Sci.* **2012**, *57*, 724–803.

(333) Tiwari, J. N.; Tiwari, R. N.; Singh, G.; Kim, K. S. Recent Progress in the Development of Anode and Cathode Catalysts for Direct Methanol Fuel Cells. *Nano Energy* **2013**, *2*, 553–578.

(334) Tiwari, J. N.; Tiwari, R. N.; Chang, Y.-M.; Lin, K.-L. A Promising Approach to the Synthesis of 3D Nanoporous Graphitic Carbon as a Unique Electrocatalyst Support for Methanol Oxidation. *ChemSusChem* **2010**, *3*, 460–466.

(335) Tiwari, J. N.; Tiwari, R. N.; Singh, G.; Lin, K.-L. Direct Synthesis of Vertically Interconnected 3-D Graphitic Nanosheets on Hemispherical Carbon Particles by Microwave Plasma CVD. *Plasmonics* **2011**, *6*, 67–73.

(336) Dubey, P.; Kumar, A.; Prakash, R. Non-Covalent Functionalization of Graphene Oxide by Polyindole and Subsequent Incorporation of Ag Nanoparticles for Electrochemical Applications. *Appl. Surf. Sci.* **2015**, *355*, 262–267.

(337) Campbell, P. G.; Merrill, M. D.; Wood, B. C.; Montalvo, E.; Worsley, M. A.; Baumann, T. F.; Biener, J. Battery/Supercapacitor Hybrid via Non-Covalent Functionalization of Graphene Macro-Assemblies. *J. Mater. Chem. A* **2014**, *2*, 17764–17770.

(338) Kong, D.; He, H.; Song, Q.; Wang, B.; Lv, W.; Yang, Q.-H.; Zhi, L. Rational Design of MoS₂@Graphene Nanocables: Towards High Performance Electrode Materials for Lithium Ion Batteries. *Energy Environ. Sci.* **2014**, *7*, 3320–3325.

(339) Yang, S.; Cao, C.; Huang, P.; Peng, L.; Sun, Y.; Wei, F.; Song, W. Sandwich-Like Porous TiO₂/Reduced Graphene Oxide (rGO) for High-Performance Lithium-Ion Batteries. *J. Mater. Chem. A* **2015**, *3*, 8701–8705.

(340) Ali, G.; Oh, S. H.; Kim, S. Y.; Kim, J. Y.; Cho, B. W.; Chung, K. Y. An Open-Framework Iron Fluoride and Reduced Graphene Oxide Nanocomposite as a High-Capacity Cathode Material for Na-Ion Batteries. *J. Mater. Chem. A* **2015**, *3*, 10258–10266.

(341) David, L.; Bhandavat, R.; Singh, G. MoS₂/Graphene Composite Paper for Sodium-Ion Battery Electrodes. *ACS Nano* **2014**, *8*, 1759–1770.

(342) Hu, C.; Zheng, G.; Zhao, F.; Shao, H.; Zhang, Z.; Chen, N.; Jiang, L.; Qu, L. A Powerful Approach to Functional Graphene Hybrids for High Performance Energy-Related Applications. *Energy Environ. Sci.* **2014**, *7*, 3699–3708.

(343) Ren, X.; Hu, Z.; Hu, H.; Qiang, R.; Li, L.; Li, Z.; Yang, Y.; Zhang, Z.; Wu, H. Noncovalently-Functionalized Reduced Graphene Oxide Sheets by Water-Soluble Methyl Green for Supercapacitor Application. *Mater. Res. Bull.* **2015**, *70*, 215–221.

(344) Jung, S. M.; Mafra, D. L.; Lin, C.-T.; Jung, H. Y.; Kong, J. Controlled Porous Structures of Graphene Aerogels and Their Effect on Supercapacitor Performance. *Nanoscale* **2015**, *7*, 4386–4393.

(345) Jana, M.; Saha, S.; Khanra, P.; Samanta, P.; Koo, H.; Murmu, N. C.; Kuila, T. Non-Covalent Functionalization of Reduced Graphene Oxide Using Sulfanilic Acid Azocromotrop and Its Application as a Supercapacitor Electrode Material. *J. Mater. Chem. A* **2015**, *3*, 7323–7331.

(346) Hsu, W.-T.; Tsai, Z.-S.; Chen, L.-C.; Chen, G.-Y.; Lin, C.-C.; Chen, M.-H.; Song, J.-M.; Lin, C.-H. Passivation Ability of Graphene

Oxide Demonstrated by Two-Different-Metal Solar Cells. *Nanoscale Res. Lett.* **2014**, *9*, 696.

(347) Kim, K. S.; Zhao, Y.; Jang, H.; Lee, S. Y.; Kim, J. M.; Kim, K. S.; Ahn, J.-H.; Kim, P.; Choi, J.-Y.; Hong, B. H. Large-Scale Pattern Growth of Graphene Films for Stretchable Transparent Electrodes. *Nature* **2009**, *457*, 706–710.

(348) Yin, Z.; Zhu, J.; He, Q.; Cao, X.; Tan, C.; Chen, H.; Yan, Q.; Zhang, H. Graphene-Based Materials for Solar Cell Applications. *Adv. Energy Mater.* **2014**, *4*, 1300574.

(349) Liu, J.; Xue, Y.; Dai, L. Sulfated Graphene Oxide as a Hole-Extraction Layer in High-Performance Polymer Solar Cells. *J. Phys. Chem. Lett.* **2012**, *3*, 1928–1933.

(350) Shi, E.; Li, H.; Yang, L.; Zhang, L.; Li, Z.; Li, P.; Shang, Y.; Wu, S.; Li, X.; Wei, J.; et al. Colloidal Antireflection Coating Improves Graphene-Silicon Solar Cells. *Nano Lett.* **2013**, *13*, 1776–1781.

(351) Wang, J. T.-W.; Ball, J. M.; Barea, E. M.; Abate, A.; Alexander-Webber, J. A.; Huang, J.; Saliba, M.; Mora-Sero, I.; Bisquert, J.; Snaith, H. J.; et al. Low-Temperature Processed Electron Collection Layers of Graphene/TiO₂ Nanocomposites in Thin Film Perovskite Solar Cells. *Nano Lett.* **2014**, *14*, 724–730.

(352) Kim, H.; Mattevi, C.; Kim, H. J.; Mittal, A.; Mkhoyan, K. A.; Riman, R. E.; Chhowalla, M. Optoelectronic Properties of Graphene Thin Films Deposited by a Langmuir-Blodgett Assembly. *Nanoscale* **2013**, *5*, 12365–12374.

(353) Supur, M.; Ohkubo, K.; Fukuzumi, S. Photoinduced Charge Separation in Ordered Self-Assemblies of Perylenediimide-Graphene Oxide Hybrid Layers. *Chem. Commun.* **2014**, *50*, 13359–13361.

(354) Dehsari, H. S.; Shalamzari, E. K.; Gavgani, J. N.; Taromi, F. A.; Ghanbary, S. Efficient Preparation of Ultralarge Graphene Oxide Using a PEDOT:PSS/GO Composite Layer as Hole Transport Layer in Polymer-Based Optoelectronic Devices. *RSC Adv.* **2014**, *4*, 55067–55076.

(355) Kymakis, E.; Savva, K.; Stylianakis, M. M.; Fotakis, C.; Stratakis, E. Flexible Organic Photovoltaic Cells with In Situ Nonthermal Photoreduction of Spin-Coated Graphene Oxide Electrodes. *Adv. Funct. Mater.* **2013**, *23*, 2742–2749.

(356) Oregan, B.; Gratzel, M. A Low-Cost, High-Efficiency Solar Cell Based on Dye-Sensitized Colloidal TiO₂ Films. *Nature* **1991**, *353*, 737–740.

(357) Hagfeldt, A.; Boschloo, G.; Sun, L.; Kloo, L.; Pettersson, H. Dye-Sensitized Solar Cells. *Chem. Rev.* **2010**, *110*, 6595–6663.

(358) Cheng, G.; Akhtar, M. S.; Yang, O. B.; Stadler, F. J. Novel Preparation of Anatase TiO₂@Reduced Graphene Oxide Hybrids for High-Performance Dye-Sensitized Solar Cells. *ACS Appl. Mater. Interfaces* **2013**, *5*, 6635–6642.

(359) Bi, E.; Chen, H.; Yang, X.; Peng, W.; Graetzel, M.; Han, L. A Quasi Core-Shell Nitrogen-Doped Graphene/Cobalt Sulfide Conductive Catalyst for Highly Efficient Dye-Sensitized Solar Cells. *Energy Environ. Sci.* **2014**, *7*, 2637–2641.

(360) Yang, W. S.; Noh, J. H.; Jeon, N. J.; Kim, Y. C.; Ryu, S.; Seo, J.; Seok, S. I. High-Performance Photovoltaic Perovskite Layers Fabricated through Intramolecular Exchange. *Science* **2015**, *348*, 1234–1237.

(361) Jeon, N. J.; Noh, J. H.; Yang, W. S.; Kim, Y. C.; Ryu, S.; Seo, J.; Seok, S. I. Compositional Engineering of Perovskite Materials for High-Performance Solar Cells. *Nature* **2015**, *517*, 476–480.

(362) Kong, D.; Wang, H.; Cha, J. J.; Pasta, M.; Koski, K. J.; Yao, J.; Cui, Y. Synthesis of MoS₂ and MoSe₂ Films with Vertically Aligned Layers. *Nano Lett.* **2013**, *13*, 1341–1347.

(363) Wang, H.; Kong, D.; Johanes, P.; Cha, J. J.; Zheng, G.; Yan, K.; Liu, N.; Cui, Y. MoSe₂ and WSe₂ Nanofilms with Vertically Aligned Molecular Layers on Curved and Rough Surfaces. *Nano Lett.* **2013**, *13*, 3426–3433.

(364) Chen, W. F.; Wang, C. H.; Sasaki, K.; Marinkovic, N.; Xu, W.; Muckerman, J. T.; Zhu, Y.; Adzic, R. R. Highly Active and Durable Nanostructured Molybdenum Carbide Electrocatalysts for Hydrogen Production. *Energy Environ. Sci.* **2013**, *6*, 943–951.

(365) Vrubel, H.; Hu, X. Molybdenum Boride and Carbide Catalyze Hydrogen Evolution in both Acidic and Basic Solutions. *Angew. Chem., Int. Ed.* **2012**, *51*, 12703–12706.

- (366) Karunadasa, H. I.; Montalvo, E.; Sun, Y.; Majda, M.; Long, J. R.; Chang, C. J. A Molecular MoS_2 Edge Site Mimic for Catalytic Hydrogen Generation. *Science* **2012**, *335*, 698–702.
- (367) Chen, W.-F.; Sasaki, K.; Ma, C.; Frenkel, A. I.; Marinkovic, N.; Muckerman, J. T.; Zhu, Y.; Adzic, R. R. Hydrogen-Evolution Catalysts Based on Non-Noble Metal Nickel-Molybdenum Nitride Nanosheets. *Angew. Chem., Int. Ed.* **2012**, *51*, 6131–6135.
- (368) Cao, B.; Veith, G. M.; Neuefeind, J. C.; Adzic, R. R.; Khalifah, P. G. Mixed Close-Packed Cobalt Molybdenum Nitrides as Non-noble Metal Electrocatalysts for the Hydrogen Evolution Reaction. *J. Am. Chem. Soc.* **2013**, *135*, 19186–19192.
- (369) Chen, W.-F.; Iyer, S.; Iyer, S.; Sasaki, K.; Wang, C.-H.; Zhu, Y.; Muckerman, J. T.; Fujita, E. Biomass-Derived Electrocatalytic Composites for Hydrogen Evolution. *Energy Environ. Sci.* **2013**, *6*, 1818–1826.
- (370) Xie, X.; Lin, L.; Liu, R.-Y.; Jiang, Y.-F.; Zhu, Q.; Xu, A.-W. The Synergistic Effect of Metallic Molybdenum Dioxide Nanoparticle Decorated Graphene as an Active Electrocatalyst for an Enhanced Hydrogen Evolution Reaction. *J. Mater. Chem. A* **2015**, *3*, 8055–8061.
- (371) Chang, Y.-H.; Lin, C.-T.; Chen, T.-Y.; Hsu, C.-L.; Lee, Y.-H.; Zhang, W.; Wei, K.-H.; Li, L.-J. Highly Efficient Electrocatalytic Hydrogen Production by MoS_x Grown on Graphene-Protected 3D Ni Foams. *Adv. Mater.* **2013**, *25*, 756–760.
- (372) Levy, R. B.; Boudart, M. Platinum-Like Behavior of Tungsten Carbide in Surface Catalysis. *Science* **1973**, *181*, 547–549.
- (373) Pan, L. F.; Li, Y. H.; Yang, S.; Liu, P. F.; Yu, M. Q.; Yang, H. G. Molybdenum Carbide Stabilized on Graphene with High Electrocatalytic Activity for Hydrogen Evolution Reaction. *Chem. Commun.* **2014**, *50*, 13135–13137.
- (374) Zhang, X.; Meng, F.; Mao, S.; Ding, Q.; Shearer, M. J.; Faber, M. S.; Chen, J.; Hamers, R. J.; Jin, S. Amorphous MoS_xCl_x Electrocatalyst Supported by Vertical Graphene for Efficient Electrochemical and Photoelectrochemical Hydrogen Generation. *Energy Environ. Sci.* **2015**, *8*, 862–868.
- (375) Zhou, W.; Zhou, J.; Zhou, Y.; Lu, J.; Zhou, K.; Yang, L.; Tang, Z.; Li, L.; Chen, S. N-Doped Carbon-Wrapped Cobalt Nanoparticles on N-Doped Graphene Nanosheets for High-Efficiency Hydrogen Production. *Chem. Mater.* **2015**, *27*, 2026–2032.
- (376) Chowdhury, I.; Duch, M. C.; Mansukhani, N. D.; Hersam, M. C.; Bouchard, D. Colloidal Properties and Stability of Graphene Oxide Nanomaterials in the Aquatic Environment. *Environ. Sci. Technol.* **2013**, *47*, 6288–6296.
- (377) Achari, A.; Datta, K. K. R.; De, M.; Dravid, V. P.; Eswaramoorthy, M. Amphiphilic Aminoclay-RGO Hybrids: A Simple Strategy to Disperse a High Concentration of RGO in Water. *Nanoscale* **2013**, *5*, 5316–5320.
- (378) McCoy, T. M.; Brown, P.; Eastoe, J.; Tabor, R. F. Noncovalent Magnetic Control and Reversible Recovery of Graphene Oxide Using Iron Oxide and Magnetic Surfactants. *ACS Appl. Mater. Interfaces* **2015**, *7*, 2124–2133.
- (379) Le, N. H.; Seema, H.; Kemp, K. C.; Ahmed, N.; Tiwari, J. N.; Park, S.; Kim, K. S. Solution-Processable Conductive Micro-Hydrogels of Nanoparticle/Graphene Platelets Produced by Reversible Self-Assembly and Aqueous Exfoliation. *J. Mater. Chem. A* **2013**, *1*, 12900–12908.
- (380) Zubir, N. A.; Yacou, C.; Motuzas, J.; Zhang, X.; da Costa, J. C. D. Structural and Functional Investigation of Graphene Oxide- Fe_3O_4 Nanocomposites for the Heterogeneous Fenton-Like Reaction. *Sci. Rep.* **2014**, *4*, 4594.
- (381) Liu, Y.; Jiang, X.; Li, B.; Zhang, X.; Liu, T.; Yan, X.; Ding, J.; Cai, Q.; Zhang, J. Halloysite Nanotubes@Reduced Graphene Oxide Composite for Removal of Dyes from Water and as Supercapacitors. *J. Mater. Chem. A* **2014**, *2*, 4264–4269.
- (382) Dong, Z.; Wang, D.; Liu, X.; Pei, X.; Chen, L.; Jin, J. Bio-Inspired Surface-Functionalization of Graphene Oxide for the Adsorption of Organic Dyes and Heavy Metal Ions with a Superhigh Capacity. *J. Mater. Chem. A* **2014**, *2*, 5034–5040.
- (383) Mondal, T.; Bhowmick, A. K.; Krishnamoorti, R. Synthesis and Characterization of Bi-Functionalized Graphene and Expanded Graphite Using n-butyl Lithium and Their Use for Efficient Water Soluble Dye Adsorption. *J. Mater. Chem. A* **2013**, *1*, 8144–8153.
- (384) Liang, R.; Shen, L.; Jing, F.; Qin, N.; Wu, L. Preparation of MIL-53(Fe)-Reduced Graphene Oxide Nanocomposites by a Simple Self-Assembly Strategy for Increasing Interfacial Contact: Efficient Visible-Light Photocatalysts. *ACS Appl. Mater. Interfaces* **2015**, *7*, 9507–9515.
- (385) Qi, X.; Tan, C.; Wei, J.; Zhang, H. Synthesis of Graphene-Conjugated Polymer Nanocomposites for Electronic Device Applications. *Nanoscale* **2013**, *5*, 1440–1451.
- (386) Lu, H.; Yao, Y.; Huang, W. M.; Hui, D. Noncovalently Functionalized Carbon Fiber by Grafted Self-Assembled Graphene Oxide and the Synergistic Effect on Polymeric Shape Memory Nanocomposites. *Composites, Part B* **2014**, *67*, 290–295.
- (387) Lu, H.; Liang, F.; Gou, J.; Leng, J.; Du, S. Synergistic Effect of Ag Nanoparticle-Decorated Graphene Oxide and Carbon Fiber on Electrical Actuation of Polymeric Shape Memory Nanocomposites. *Smart Mater. Struct.* **2014**, *23*, 085034.
- (388) Love, J. C.; Estroff, L. A.; Kriebel, J. K.; Nuzzo, R. G.; Whitesides, G. M. Self-Assembled Monolayers of Thiolates on Metals as a Form of Nanotechnology. *Chem. Rev.* **2005**, *105*, 1103–1169.
- (389) Schedin, F.; Geim, A. K.; Morozov, S. V.; Hill, E. W.; Blake, P.; Katsnelson, M. I.; Novoselov, K. S. Detection of Individual Gas Molecules Adsorbed on Graphene. *Nat. Mater.* **2007**, *6*, 652–655.
- (390) Wang, X.; Li, X.; Zhang, L.; Yoon, Y.; Weber, P. K.; Wang, H.; Guo, J.; Dai, H. N-Doping of Graphene Through Electrothermal Reactions with Ammonia. *Science* **2009**, *324*, 768–771.
- (391) Joo, P.; Kim, B. J.; Jeon, E. K.; Cho, J. H.; Kim, B.-S. Optical Switching of the Dirac Point in Graphene Multilayer Field-Effect Transistors Functionalized with Spiropyran. *Chem. Commun.* **2012**, *48*, 10978–10980.
- (392) Li, B.; Klekachev, A. V.; Cantoro, M.; Huyghebaert, C.; Stesmans, A.; Asselberghs, I.; De Gendt, S.; De Feyter, S. Toward Tunable Doping in Graphene FETs by Molecular Self-Assembled Monolayers. *Nanoscale* **2013**, *5*, 9640–9644.
- (393) Long, B.; Manning, M.; Burke, M.; Szafraneck, B. N.; Visimberga, G.; Thompson, D.; Greer, J. C.; Povey, I. M.; MacHale, J.; Lejosne, G.; et al. Non-Covalent Functionalization of Graphene Using Self-Assembly of Alkane-Amines. *Adv. Funct. Mater.* **2012**, *22*, 717–725.
- (394) Wang, H.; Bi, S.-G.; Ye, Y.-S.; Xue, Y.; Xie, X.-L.; Mai, Y.-W. An Effective Non-Covalent Grafting Approach to Functionalize Individually Dispersed Reduced Graphene Oxide Sheets with High Grafting Density, Solubility and Electrical Conductivity. *Nanoscale* **2015**, *7*, 3548–3557.
- (395) Kozhemyakina, N. V.; Englert, J. M.; Yang, G.; Spiecker, E.; Schmidt, C. D.; Hauke, F.; Hirsch, A. Non-Covalent Chemistry of Graphene: Electronic Communication with Dendronized Perylene Bisimides. *Adv. Mater.* **2010**, *22*, 5483–5487.
- (396) Parvez, K.; Li, R.; Puniredd, S. R.; Hernandez, Y.; Hinkel, F.; Wang, S.; Feng, X.; Muellen, K. Electrochemically Exfoliated Graphene as Solution-Processable, Highly Conductive Electrodes for Organic Electronics. *ACS Nano* **2013**, *7*, 3598–3606.
- (397) Woszczyzna, M.; Winter, A.; Grothe, M.; Willunat, A.; Wundrack, S.; Stosch, R.; Weimann, T.; Ahlers, F.; Turchanin, A. All-Carbon Vertical van der Waals Heterostructures: Non-destructive Functionalization of Graphene for Electronic Applications. *Adv. Mater.* **2014**, *26*, 4831–4837.
- (398) Nottbohm, C. T.; Turchanin, A.; Beyer, A.; Stosch, R.; Goelzhaeuser, A. Mechanically Stacked 1-nm-Thick Carbon Nanosheets: Ultrathin Layered Materials with Tunable Optical, Chemical, and Electrical Properties. *Small* **2011**, *7*, 874–883.
- (399) Wang, Z. X.; Eigler, S.; Ishii, Y.; Hu, Y. C.; Papp, C.; Lytken, O.; Steinruck, H. P.; Halik, M. A Facile Approach to Synthesize an Oxofunctionalized Graphene/Polymer Composite for Low-Voltage Operating Memory Devices. *J. Mater. Chem. C* **2015**, *3*, 8595–8604.
- (400) Roth, A.; Ragoussi, M.-E.; Wibmer, L.; Katsukis, G.; de la Torre, G.; Torres, T.; Guldi, D. M. Electron-Accepting Phthalocyanine Pyrene Conjugates: Towards Liquid Phase Exfoliation of Graphite and Photoactive Nanohybrid Formation with Graphene. *Chem. Sci.* **2014**, *5*, 3432–3438.

- (401) Wang, Z.; Hu, G.; Liu, J.; Liu, W.; Zhang, H.; Wang, B. Coordinated Assembly of a New 3D Mesoporous $\text{Fe}_3\text{O}_4/\text{Cu}_2\text{O}$ -Graphene Oxide Framework as a Highly Efficient and Reusable Catalyst for the Synthesis of Quinoxalines. *Chem. Commun.* **2015**, 51, 5069–5072.
- (402) Ren, R.; Li, S.; Li, J.; Ma, J.; Liu, H.; Ma, J. Enhanced Catalytic Activity of Au Nanoparticles Self-Assembled on Thiophenol Functionalized Graphene. *Catal. Sci. Technol.* **2015**, 5, 2149–2156.
- (403) Pathak, P.; Gupta, S.; Grosulak, K.; Imahori, H.; Subramanian, V. Nature-Inspired Tree-Like TiO_2 Architecture: A 3D Platform for the Assembly of CdS and Reduced Graphene Oxide for Photoelectrochemical Processes. *J. Phys. Chem. C* **2015**, 119, 7543–7553.
- (404) Padhi, D. K.; Parida, K.; Singh, S. K. Facile Fabrication Of RGO/N-GZ Mixed Oxide Nanocomposite For Efficient Hydrogen Production Under Visible Light. *J. Phys. Chem. C* **2015**, 119, 6634–6646.
- (405) Ullah, K.; Ye, S.; Lei, Z.; Cho, K.-Y.; Oh, W.-C. Synergistic Effect of PtSe_2 and Graphene Sheets Supported by TiO_2 as Cocatalysts Synthesized via Microwave Techniques for Improved Photocatalytic Activity. *Catal. Sci. Technol.* **2015**, 5, 184–198.
- (406) Jiang, D.; Du, X.; Liu, Q.; Hao, N.; Qian, J.; Dai, L.; Mao, H.; Wang, K. Anchoring AgBr Nanoparticles on Nitrogen-Doped Graphene for Enhancement of Electrochemiluminescence and Radical Stability. *Chem. Commun.* **2015**, 51, 4451–4454.
- (407) Joseph, K. L. V.; Lim, J.; Anthonysamy, A.; Kim, H.-I.; Choi, W.; Kim, J. K. Squaraine-Sensitized Composite of a Reduced Graphene Oxide/ TiO_2 Photocatalyst: π - π Stacking as a New Method of Dye Anchoring. *J. Mater. Chem. A* **2015**, 3, 232–239.
- (408) Ma, H.; Tian, J.; Cui, L.; Liu, Y.; Bai, S.; Chen, H.; Shan, Z. Porous Activated Graphene Nanoplatelets Incorporated in TiO_2 Photoanodes for High-Efficiency Dye-Sensitized Solar Cells. *J. Mater. Chem. A* **2015**, 3, 8890–8895.
- (409) Xu, L.; Huang, W.-Q.; Wang, L.-L.; Tian, Z.-A.; Hu, W.; Ma, Y.; Wang, X.; Pan, A.; Huang, G.-F. Insights into Enhanced Visible-Light Photocatalytic Hydrogen Evolution of $\text{g-C}_3\text{N}_4$ and Highly Reduced Graphene Oxide Composite: The Role of Oxygen. *Chem. Mater.* **2015**, 27, 1612–1621.
- (410) Meng, F.; Cushing, S. K.; Li, J.; Hao, S.; Wu, N. Enhancement of Solar Hydrogen Generation by Synergistic Interaction of $\text{La}_2\text{Ti}_2\text{O}_7$ Photocatalyst with Plasmonic Gold Nanoparticles and Reduced Graphene Oxide Nanosheets. *ACS Catal.* **2015**, 5, 1949–1955.
- (411) Feifel, S. C.; Stieger, K. R.; Lokstein, H.; Lux, H.; Lisdat, F. High Photocurrent Generation by Photosystem I on Artificial Interfaces Composed of π -System-Modified Graphene. *J. Mater. Chem. A* **2015**, 3, 12188–12196.
- (412) Moon, G.-H.; Kim, W.; Bokare, A. D.; Sung, N.-E.; Choi, W. Solar Production of H_2O_2 on Reduced Graphene Oxide- TiO_2 Hybrid Photocatalysts Consisting of Earth-Abundant Elements Only. *Energy Environ. Sci.* **2014**, 7, 4023–4028.
- (413) Lee, D. H.; Song, D.; Kang, Y. S.; Park, W. I. Three-Dimensional Monolayer Graphene and TiO_2 Hybrid Architectures for High-Efficiency Electrochemical Photovoltaic Cells. *J. Phys. Chem. C* **2015**, 119, 6880–6885.
- (414) Shah, S.; Yin, P. T.; Uehara, T. M.; Chueng, S. D.; Yang, L.; Lee, K. B. Guiding Stem Cell Differentiation into Oligodendrocytes Using Graphene-Nanofiber Hybrid Scaffolds. *Adv. Mater.* **2014**, 26, 3673–3680.
- (415) Kim, T. H.; Shah, S.; Yang, L.; Yin, P. T.; Hossain, M. K.; Conley, B.; Choi, J. W.; Lee, K. B. Controlling Differentiation of Adipose-Derived Stem Cells Using Combinatorial Graphene Hybrid-Pattern Arrays. *ACS Nano* **2015**, 9, 3780–3790.
- (416) Park, J.; Kim, B.; Han, J.; Oh, J.; Park, S.; Ryu, S.; Jung, S.; Shin, J.; Lee, B. S.; Hong, B. H.; et al. Graphene Oxide Flakes as a Cellular Adhesive: Prevention of Reactive Oxygen Species Mediated Death of Implanted Cells for Cardiac Repair. *ACS Nano* **2015**, 9, 4987–4999.
- (417) Kang, S.; Park, J. B.; Lee, T. J.; Ryu, S.; Bhang, S. H.; La, W. G.; Noh, M. K.; Hong, B. H.; Kim, B. S. Covalent Conjugation of Mechanically Stiff Graphene Oxide Flakes to Three-Dimensional Collagen Scaffolds for Osteogenic Differentiation of Human Mesenchymal Stem Cells. *Carbon* **2015**, 83, 162–172.
- (418) Tiwari, J. N.; Vij, V.; Kemp, K. C.; Kim, K. S. Engineered Carbon-Nanomaterial-Based Electrochemical Sensors for Biomolecules. *ACS Nano* **2016**, 10, 46–80.
- (419) Gu, W.; Deng, X.; Gu, X.; Jia, X.; Lou, B.; Zhang, X.; Li, J.; Wang, E. Stabilized, Superparamagnetic Functionalized Graphene/ $\text{Fe}_3\text{O}_4/\text{Au}$ Nanocomposites for a Magnetically-Controlled Solid-State Electrochemiluminescence Biosensing Application. *Anal. Chem.* **2015**, 87, 1876–1881.
- (420) Bagheri, H.; Arab, S. M.; Khoshshafar, H.; Afkhami, A. A Novel Sensor for Sensitive Determination of Atropine Based on a Co_3O_4 -Reduced Graphene Oxide Modified Carbon Paste Electrode. *New J. Chem.* **2015**, 39, 3875–3881.
- (421) Yoon, H. J.; Kim, T. H.; Zhang, Z.; Azizi, E.; Pham, T. M.; Paoletti, C.; Lin, J.; Ramnath, N.; Wicha, M. S.; Hayes, D. F.; et al. Sensitive Capture of Circulating Tumour Cells by Functionalized Graphene Oxide Nanosheets. *Nat. Nanotechnol.* **2013**, 8, 735–741.
- (422) Lerner, M. B.; Matsunaga, F.; Han, G. H.; Hong, S. J.; Xi, J.; Crook, A.; Perez-Aguilar, J. M.; Park, Y. W.; Saven, J. G.; Liu, R.; et al. Scalable Production of Highly Sensitive Nanosensors Based on Graphene Functionalized with a Designed G Protein-Coupled Receptor. *Nano Lett.* **2014**, 14, 2709–2714.
- (423) Singh, M.; Holzinger, M.; Tabrizian, M.; Winters, S.; Berner, N. C.; Cosnier, S.; Duesberg, G. S. Noncovalently Functionalized Monolayer Graphene for Sensitivity Enhancement of Surface Plasmon Resonance Immunosensors. *J. Am. Chem. Soc.* **2015**, 137, 2800–2803.
- (424) Hu, W.; He, G.; Zhang, H.; Wu, X.; Li, J.; Zhao, Z.; Qiao, Y.; Lu, Z.; Liu, Y.; Li, C. M. Polydopamine-Functionalization of Graphene Oxide to Enable Dual Signal Amplification for Sensitive Surface Plasmon Resonance Imaging Detection of Biomarker. *Anal. Chem.* **2014**, 86, 4488–4493.
- (425) Yi, M.; Yang, S.; Peng, Z.; Liu, C.; Li, J.; Zhong, W.; Yang, R.; Tan, W. Two-Photon Graphene Oxide/Aptamer Nanosensing Conjugate for In Vitro or In Vivo Molecular Probing. *Anal. Chem.* **2014**, 86, 3548–3554.
- (426) Castrignano, S.; Gilardi, G.; Sadeghi, S. J. Human Flavine-Containing Monooxygenase 3 on Graphene Oxide for Drug Metabolism Screening. *Anal. Chem.* **2015**, 87, 2974–2980.
- (427) Xu, S.; Man, B.; Jiang, S.; Wang, J.; Wei, J.; Xu, S.; Liu, H.; Gao, S.; Liu, H.; Li, Z.; et al. Graphene/Cu Nanoparticle Hybrids Fabricated by Chemical Vapor Deposition As Surface-Enhanced Raman Scattering Substrate for Label-Free Detection of Adenosine. *ACS Appl. Mater. Interfaces* **2015**, 7, 10977–10987.
- (428) Datta, K. K. R.; Kozak, O.; Ranc, V.; Havrdova, M.; Bourlinos, A. B.; Safarova, K.; Hola, K.; Tomankova, K.; Zoppellaro, G.; Otyepka, M.; et al. Quaternized Carbon Dot-Modified Graphene Oxide for Selective Cell Labelling – Controlled Nucleus and Cytoplasm Imaging. *Chem. Commun.* **2014**, 50, 10782–10785.
- (429) Yin, P. T.; Shah, S.; Chhowalla, M.; Lee, K.-B. Design, Synthesis, and Characterization of Graphene-Nanoparticle Hybrid Materials for Bioapplications. *Chem. Rev.* **2015**, 115, 2483–2531.
- (430) Dikin, D. A.; Stankovich, S.; Zimney, E. J.; Piner, R. D.; Dommett, G. H. B.; Evmenenko, G.; Nguyen, S. T.; Ruoff, R. S. Preparation and Characterization of Graphene Oxide Paper. *Nature* **2007**, 448, 457–460.
- (431) Markovic, Z. M.; Harhaji-Trajkovic, L. M.; Todorovic-Markovic, B. M.; Kepic, D. P.; Arsin, K. M.; Jovanovic, S. P.; Pantovic, A. C.; Dramicanin, M. D.; Trajkovic, V. S. In Vitro Comparison of the Photothermal Anticancer Activity of Graphene Nanoparticles and Carbon Nanotubes. *Biomaterials* **2011**, 32, 1121–1129.
- (432) Bitounis, D.; Ali-Boucetta, H.; Hong, B. H.; Min, D.-H.; Kostarelos, K. Prospects and Challenges of Graphene in Biomedical Applications. *Adv. Mater.* **2013**, 25, 2258–2268.
- (433) Feng, L.; Wu, L.; Qu, X. New Horizons for Diagnostics and Therapeutic Applications of Graphene and Graphene Oxide. *Adv. Mater.* **2013**, 25, 168–186.
- (434) Robinson, J. T.; Tabakman, S. M.; Liang, Y.; Wang, H.; Casalongue, H. S.; Daniel, V.; Dai, H. Ultrasmall Reduced Graphene Oxide with High Near-Infrared Absorbance for Photothermal Therapy. *J. Am. Chem. Soc.* **2011**, 133, 6825–6831.

- (435) Jung, H. S.; Kong, W. H.; Sung, D. K.; Lee, M.-Y.; Beack, S. E.; Keum, D. H.; Kim, K. S.; Yun, S. H.; Hahn, S. K. Nanographene Oxide-Hyaluronic Acid Conjugate for Photothermal Ablation Therapy of Skin Cancer. *ACS Nano* **2014**, *8*, 260–268.
- (436) Liu, J.; Jiang, X.; Xu, L.; Wang, X.; Hennink, W. E.; Zhuo, R. Novel Reduction-Responsive Cross-Linked Polyethylenimine Derivatives by Click Chemistry for Nonviral Gene Delivery. *Bioconjugate Chem.* **2010**, *21*, 1827–1835.
- (437) Ma, N.; Li, Y.; Xu, H.; Wang, Z.; Zhang, X. Dual Redox Responsive Assemblies Formed from Diselenide Block Copolymers. *J. Am. Chem. Soc.* **2010**, *132*, 442–443.
- (438) Yang, X.; Zhao, N.; Xu, F.-J. Biocleavable Graphene Oxide Based-Nanohybrids Synthesized via ATRP for Gene/Drug Delivery. *Nanoscale* **2014**, *6*, 6141–6150.
- (439) Sherlock, S. P.; Tabakman, S. M.; Xie, L.; Dai, H. Photothermally Enhanced Drug Delivery by Ultrasmall Multifunctional FeCo/Graphitic Shell Nanocrystals. *ACS Nano* **2011**, *5*, 1505–1512.
- (440) Dembereldorj, U.; Kim, M.; Kim, S.; Ganbold, E.-O.; Lee, S. Y.; Joe, S.-W. A Spatiotemporal Anticancer Drug Release Platform of PEGylated Graphene Oxide Triggered by Glutathione In Vitro and In Vivo. *J. Mater. Chem.* **2012**, *22*, 23845–23851.
- (441) Kiyomiya, K.; Matsuo, S.; Kurebe, M. Mechanism of Specific Nuclear Transport of Adriamycin: The Mode of Nuclear Translocation of Adriamycin-Proteasome Complex. *Cancer Res.* **2001**, *61*, 2467–2471.
- (442) Ochs, M.; Carregal-Romero, S.; Rejman, J.; Braeckmans, K.; De Smedt, S. C.; Parak, W. J. Light-Addressable Capsules as Caged Compound Matrix for Controlled Triggering of Cytosolic Reactions. *Angew. Chem., Int. Ed.* **2013**, *52*, 695–699.
- (443) Kim, H.; Lee, D.; Kim, J.; Kim, T.-I.; Kim, W. J. Photothermally Triggered Cytosolic Drug Delivery via Endosome Disruption Using a Functionalized Reduced Graphene Oxide. *ACS Nano* **2013**, *7*, 6735–6746.
- (444) Yan, L.; Chang, Y.-N.; Yin, W.; Tian, G.; Zhou, G. L.; Liu, X.; Xing, G.; Zhao, L.; Gu, Z.; Zhao, Y. On-Demand Generation of Singlet Oxygen from a Smart Graphene Complex for the Photodynamic Treatment of Cancer Cells. *Biomater. Sci.* **2014**, *2*, 1412–1418.
- (445) Dong, H.; Dai, W.; Ju, H.; Lu, H.; Wang, S.; Xu, L.; Zhou, S.-F.; Zhang, Y.; Zhang, X. Multifunctional Poly(L-lactide)-Polyethylene Glycol-Grafted Graphene Quantum Dots for Intracellular MicroRNA Imaging and Combined Specific-Gene-Targeting Agents Delivery for Improved Therapeutics. *ACS Appl. Mater. Interfaces* **2015**, *7*, 11015–11023.
- (446) Bianco, A. Graphene: Safe or Toxic? The Two Faces of the Medal. *Angew. Chem., Int. Ed.* **2013**, *52*, 4986–4997.